Titre: Title:	Automatic Mesh-Based Segmentation of Multiple Organs in MR Images
Auteur: Author:	Majid Reza Moheb Pour
Date:	2018
Type:	Mémoire ou thèse / Dissertation or Thesis
Référence: Citation:	Moheb Pour, M. R. (2018). Automatic Mesh-Based Segmentation of Multiple Organs in MR Images [Thèse de doctorat, École Polytechnique de Montréal]. PolyPublie. https://publications.polymtl.ca/3258/

URL de PolyPublie: PolyPublie URL:	https://publications.polymtl.ca/3258/
Directeurs de recherche: Advisors:	François Guibault, & Farida Cheriet
Programme: Program:	Génie informatique

UNIVERSITÉ DE MONTRÉAL

AUTOMATIC MESH-BASED SEGMENTATION OF MULTIPLE ORGANS IN MR IMAGES

MAJID REZA MOHEB POUR

DÉPARTEMENT DE GÉNIE INFORMATIQUE ET GÉNIE LOGICIEL

ÉCOLE POLYTECHNIQUE DE MONTRÉAL

THÈSE PRÉSENTÉE EN VUE DE L'OBTENTION

DU DIPLÔME DE PHILOSOPHIAE DOCTOR

(GÉNIE INFORMATIQUE)

AOÛT 2018

UNIVERSITÉ DE MONTRÉAL

ÉCOLE POLYTECHNIQUE DE MONTRÉAL

Cette thèse intitulée :

AUTOMATIC MESH-BASED SEGMENTATION OF MULTIPLE ORGANS IN MR IMAGES

présentée par : MOHEB POUR Majid Reza

en vue de l'obtention du diplôme de : Philosophiae Doctor

a été dûment acceptée par le jury d'examen constitué de :

M. BILODEAU Guillaume-Alexandre, Ph. D., président

M. GUIBAULT Francois, Ph. D., membre et directeur de recherche

Mme CHERIET Farida, Ph. D., membre et codirectrice de recherche

M. CAMARERO Ricardo, Ph. D., membre

M. KHACHAN Mohammed, Ph. D., membre externe

DEDICATION

In memory of my mother

To my family & dear wife

With love and eternal appreciation

ACKNOWLEDGEMENTS

This thesis has been made possible through the help and support from many encounters. Notably, I am deeply thankful to all members of my Ph.D. committee who took patience to read and evaluate this manuscript. I am, of course, extremely grateful to my director, Francois Guibault, for his excellent guidance, support, caring, and patience during my Ph.D. study. I have learnt a lot from the sympathetic and supportive ambience of your personality. Also, I would like to express my great appreciation to my co-director, Farida Cheriet, for her supervision, help, valuable advice and corrections.

I would specially like to thank Dr. Julien Dompierre for his help and many insightful discussions and suggestions. This work could not have been succeeded without your help.

I take this opportunity to extend my sincerest thanks to all of my friends and colleagues at Polytechnique de Montréal for their valuable technical and emotional supports during all these years.

On a personal note, I must thank my close and deep friends, who gave me the courage to pursue the Ph.D. when times were darker, Amir Banani, Daneshmand's family for their amazing kindness.

The most important of all in the world I thank my family; my late mother, Simin, who all my efforts in life are because of her love and happiness, my father, Ali, my sisters, Mitra & Samira and my brothers, Saeed & Vahid. Whatever I have in my life is because of your love and support. Your prayer for me was what sustained me thus far.

The best thing that happened to me during my journey at Polytechnique was to get to know my beloved wife, Azadeh, who enlighten my life with her presence. I thank you for being so understanding and for putting up with me through the toughest moments of my life. Your presence, love and support during these years of my study gave me lots of motivation to continue.

RÉSUMÉ

La segmentation de structures anatomiques multiples dans des images de résonance magnétique (RM) est souvent requise dans des applications de génie biomédical telles que la simulation numérique, la chirurgie guidée par l'image, la planification de traitements, etc. De plus, il y a un besoin croissant pour une segmentation automatique d'organes multiples et de structures complexes à partir de cette modalité d'imagerie. Il existe plusieurs techniques de segmentation multi-objets qui ont été appliquées avec succès sur des images de tomographie axiale à rayons-X (CT). Cependant, dans le cas des images RM cette tâche est plus difficile en raison de l'inhomogénéité des intensités dans ces images et de la variabilité dans l'apparence des structures anatomiques. Par conséquent, l'état de l'art sur la segmentation multi-objets sur des images RM est beaucoup plus faible que celui sur les images CT.

Parmi les travaux qui portent sur la segmentation d'images RM, les approches basées sur la segmentation de régions sont sensibles au bruit et la non uniformité de l'intensité dans les images. Les approches basées sur les contours ont de la difficulté à regrouper les informations sur les contours de sorte à produire un contour fermé cohérent. Les techniques basées sur les atlas peuvent avoir des problèmes en présence de structures complexes avec une grande variabilité anatomique. Les modèles déformables représentent une des méthodes les plus populaire pour la détection automatique de différents organes dans les images RM. Cependant, ces modèles souffrent encore d'une limitation importante qui est leur sensibilité à la position initiale et la forme du modèle. Une initialisation inappropriée peut conduire à un échec dans l'extraction des frontières des objets. D'un autre côté, le but ultime d'une segmentation automatique multi-objets dans les images RM est de produire un modèle qui peut aider à extraire les caractéristiques structurelles d'organes distincts dans les images. Les méthodes d'initialisation automatique actuelles qui utilisent différents descripteurs ne réussissent pas complètement l'extraction d'objets multiples dans les images RM. Nous avons besoin d'exploiter une information plus riche qui se trouve dans les contours des organes. Dans ce contexte les maillages adaptatifs anisotropiques semblent être une solution potentielle au problème soulevé. Les maillages adaptatifs anisotropiques construits à partir des images RM contiennent de l'information à un plus haut niveau d'abstraction représentant les éléments, d'une orientation et d'une forme donnée, qui constituent les différents organes dans l'image. Les méthodes existantes pour la

construction de maillages adaptatifs sont basées sur les intensités dans l'image et possèdent une limitation pratique qui est l'alignement inadéquat des éléments du maillage en présence de contours inclinés dans l'image. Par conséquent, nous avons aussi besoin d'améliorer le processus d'adaptation de maillage pour produire une meilleure représentation de l'image basée sur un maillage.

Dans le cadre de ce projet de doctorat, pour pallier au problèmes soulevés nous allons présenter une nouvelle méthode pour la segmentation automatique d'organes multiples dans les images RM en incorporant une technique d'adaptation de maillages. Dans une première étape, nous améliorons le processus d'adaptation anisotropique pour des maillages construits à partir d'images RM. Ainsi, les éléments du maillage sont alignés adéquatement avec le contenu de l'image et améliore l'anisotropie du maillage le long des contours dans toutes les directions. Ensuite, le maillage résultant est utilisé pour l'initialisation de modèles actifs multiples qui permettent d'extraire simultanément les frontières initiales des objets qui sont proches des frontières réelles d'organes multiples. Finalement, une méthode de convolution par champ de vecteurs est utilisée pour guider l'évolution de la courbe vers les frontières des organes afin d'obtenir les résultats de la segmentation finale avec une meilleure performance en termes de vitesse et de précision.

Plusieurs expériences et comparaisons ont été effectuées afin d'évaluer les différentes étapes de la méthodologie proposée. Notre méthode a été appliquée sur des séries d'images RM et les résultats obtenus démontrent sa capacité pour l'extraction simultanée de frontières approximatives initiales qui sont proches des frontières réelles d'organes multiples. Une comparaison a été effectuée entre la méthode proposée et trois autres méthodes distinctes pour l'initialisation automatique afin d'évaluer l'efficacité de la nouvelle approche d'initialisation et son impact sur la performance de la segmentation. La comparaison porte sur le nombre de modèles, le nombre d'itérations et le temps de convergence. Les résultats démontrent une amélioration de la convergence et de la vitesse des modèles actifs dans la segmentation d'organes multiples par rapport aux trois méthodes considérées. Afin d'évaluer la précision des résultats de segmentation, nous avons aussi effectué une comparaison entre les contours segmentés automatiquement à l'aide de la méthode proposée et ceux segmentés par un expert sur des images RM de colonnes vertébrales.

Cependant, la méthode proposée possède certaines limitations comme par exemple son échec dans l'extraction de descripteurs anisotropiques dans des régions à faible contraste et le fait qu'elle soit validée uniquement sur des images 2D, ce qui laisse de la place à des améliorations. Une des recommandations serait de construire une métrique à partir de techniques plus avancées pour l'extraction de descripteurs anisotropiques à partir des images et d'étendre l'algorithme en 3D pour prendre en charge des volumes d'images RM. Une autre recommandation serait de poursuivre cette recherche afin d'annoter les régions segmentées dans le but d'utiliser le modèle géométrique obtenu dans des applications cliniques comme la simulation numérique de traitements.

ABSTRACT

Segmentation of multiple anatomical structures in MR images is often required for biomedical engineering applications such as clinical simulation, image-guided surgery, treatment planning, etc. Moreover, there is a growing need for automatic segmentation of multiple organs and complex structures from this medical imaging modality. Many successful multi-object segmentation attempts were introduced for CT images. However in the case of MR images it is a more challenging task due to intensity inhomogeneity and variability of anatomy appearance. Therefore, state-of-the-art in multi-object MR segmentation is very inferior to that of CT images.

In literature dealing with MR image segmentation, the region-based approaches are sensitive to noise and non-uniformity in the input image. The edge-based approaches are challenging to group the edge information into a coherent closed contour. The atlas-based techniques can be problematic for complicated structures with anatomical variability. Deformable models are among the most popular methods for automatic detection of different organs in MR images. However they still have an important limitation which is that they are sensitive to initial position and shape of the model. An unsuitable initialization may provide failure to capture the true boundaries of the objects. On the other hand, a useful aim for an automatic multi-object MR segmentation is to provide a model which promotes understanding of the structural features of the distinct objects within the MR images. The current automatic initialization methods which have used different descriptors are not completely successful in extracting multiple objects from MR images and we need to find richer information that is available from edges. In this regard, anisotropic adaptive meshes seem to be a potential solution to the aforesaid limitation. Anisotropic adaptive meshes constructed from MR images contain higher level, abstract information about the anatomical structures of the organs within the image retained as the elements shape and orientation. Existing methods for constructing adaptive meshes based on image features have a practical limitation where manifest itself in inadequate mesh elements alignment to inclined edges in the image. Therefore, we also have to enhance mesh adaptation process to provide a better mesh-based representation.

In this Ph.D. project, considering the highlighted limitations we are going to present a novel method for automatic segmentation of multiple organs in MR images by incorporating mesh adaptation techniques. In our progress, first, we improve an anisotropic adaptation process for the

meshes that are constructed from MR images where the mesh elements align adequately to the image content and improve mesh anisotropy along edges in all directions. Then the resulting adaptive meshes are used for initialization of multiple active models which leads to extract initial object boundaries close to the true boundaries of multiple objects simultaneously. Finally, the Vector Field Convolution method is utilized to guide curve evolution towards the object boundaries to obtain the final segmentation results and present a better performance in terms of speed and accuracy.

Experiments and comparison have been carried out to evaluate different parts of the methodology. This method has been applied on series of MR images, and results show the ability of the proposed method in simultaneously extracting initial approximate boundaries that are close to the exact boundaries of multiple organs. A comparison has been made between the proposed method and three distinct methods for automatic initialization to show the effectiveness of the new initialization approach on segmentation performance. The comparison is done in terms of number of models, number of iterations, and convergence time and results indicate an improvement in the convergence and speed of active model segmentation of multiple organs with respect to those obtained using existing methods. In order to assess the accuracy of the segmentation results of our approach we also perform a comparison with ground truth data provided by experts for a series of MR images.

There are, however, some general remaining limitations, for instance, failure to reveal anisotropic features in the areas with low contrast or also being limited to the 2D images, which still leaves room for improvement. It is recommended to try to construct a metric from more advanced techniques for extracting anisotropic features from images and also try to extend the algorithm to deal with volumetric MR images. It is also recommended to pursue research for labeling the segmented regions, which may potentially impact further applications.

TABLE OF CONTENTS

DEDICATION III

ACKNOWLEDGEMENTS IV

RÉSUMÉ V

ABSTRACT VIII

TABLE OF CONTENTS X

LIST OF TABLES XIII

LIST OF FIGURES XIV

LIST OF SYMBOLS AND ABBREVIATIONS XVIII

CHAPTER 1 INTRODUCTION 1

1.1 Context 1

1.2 Motivation 3

1.3 Organization 5

CHAPTER 2 BACKGROUND & LITERATURE REVIEW 7

2.1 Mesh Generation and Adaptation 7

2.1.1 Anisotropic Mesh Adaptation 10

2.1.1.1 Metric Notion 10

2.1.1.2 Geometric Representation of Metrics 11

2.1.1.3 Mesh Adaptation Scheme 12

2.2 Mesh-based Image Models 13

2.3 MRI Segmentation Techniques 16

2.3.1 Classification-Based Techniques 16

2.3.2 Region-Based Techniques 18

2.3.3 Contour-Based Techniques 19

2.3.3.1 Deformable Models 20
2.3.3.2 Deformable Model Initialization 28
2.4 Multi-Object Segmentation 32
CHAPTER 3 RESEARCH OBJECTIVES 35
3.1 Problem Statement 35
3.2 General and specific Objectives 36
3.3 General Methodology 36
CHAPTER 4 METHODOLOGY 38
4.1 Adaptive Mesh Generation 38
4.1.1 Metric Construction 39
4.1.1.1 Hessian Matrix Computation 39
4.1.1.2 Directional Hessian Computation 40
4.2 Multi-Object Extraction 48
4.2.1 Partition of Elements 48
4.2.2 Extracting Holes 49
4.3 Segmentation Process 54
4.3.1 Active Models Initialization 55
4.3.2 Evolution Process 57
4.4 Evaluation 59
CHAPTER 5 RESULTS AND DISCUSSIONS 60
5.1 Anisotropic Mesh Adaptation 60
5.2 Active Contour Initialization 71
5.3 MR Image Segmentation 78
5.4 General Discussion 87

5.4.1 Limitation 89

CHAPTER 6 CONCLUSION 91

6.1 Contributions 92

6.2 Recommendations and Perspectives 93

BIBLIOGRAPHY 94

LIST OF TABLES

Table 5-1 : Number of elements in adaptive meshes constructed by the three approaches 64

Table 5-2 : Segmentation performance summary for four methods (CoD, FFS, PIG, and Proposed method) on a MR image series.....84

LIST OF FIGURES

Figure 1.1 : MRI scanner cutaway (left) and an MR image of human trunk (right) 1

Figure 1.2 : Understanding local structure based on eigenvalues where *E* is the change of intensity for a small shift 4

Figure 2.1: Different types of meshes structured (left) and unstructured (right) 8

Figure 2.2: Size specification map and the corresponding isotropic mesh adapted based on the specified sizes [10] 9

Figure 2.3: Anisotropic map of a domain and the corresponding anisotropic mesh adapted based on the specified size, stretching and orientation [10] 9

Figure 2.4: Geometric representation of a metric tensor 11

Figure 2.5 : The adaptation process of OORT [22] 12

Figure 2.6 : Three examples of simple images with edges in different directions (left), corresponding adaptive meshes by spatial convolution filtering approach (middle), and corresponding adaptive meshes by geometric approximation approach (right) 15

Figure 2.7 : Geometric representation of deformable models 21

Figure 2.8 : Some iterative steps for parametric curve evolution to fit an edge 23

Figure 2.9 : Level set function of a curve 25

Figure 2.10 : Example of topology changes of the contour for ϕ function 26

Figure 2.11 : Manual initialization on a MR image (left) and final segmentation result (right) 28

Figure 2.12 : Simple model initialization on a MR image (left) and final segmentation result (right) 29

Figure 2.13 : Part of GVF fields and centers of divergence marked by circles [97] 29

Figure 2.14 : (a) An example of a binary feature map, (b) the derived EPGVF vector field, and (c) the segmented force field enclosed by the two dark thick contours 30

Figure 2.15 : Original image (left), computed VFC field (middle) and the estimated external energy of the VFC field (right) 31

Figure 2.16 : Three different automatic initialization methods on a MR image; center of divergence (CoD) method (left), force field segmentation (FFS) method (middle), and Poisson inverse gradient (PIG) method (right) 31

Figure 3.1 : Summary of general methodology presented in this thesis 37

Figure 4.1: Initial triangular mesh corresponding to original image pixels 38

Figure 4.2 : Image I as a function of intensity values in a global coordinate system (x, y) 40

Figure 4.3 : Changing coordinate system and using proper neighborhood for Hessian computation 42

Figure 4.4 : Illustration of non-maximum suppression when the edge is blurry. The edge strengths are indicated both as colors and numbers.....44

Figure 4.5 : Picking a proper neighborhood for the pixel in the center according to its edge direction.....44

Figure 4.6 : Original images (top) and the corresponding adaptive meshes generated based on proposed metric construction (bottom) 47

Figure 4.7 : (A) Original MR image; (B) Adaptive mesh of the same image; (C) Zoom on the highlighted part in (B) 47

Figure 4.8 : Bimodal histogram of the element size for the mesh at the top and the result of selecting two different threshold values and removing the region elements from the mesh .49

Figure 4.9 : (a) Original MR image (b) The corresponding adaptive mesh of the image (c) Extracting boundary elements (d) Identifying holes by locating boundary edges 50

Figure 4.10 : Various status of produced holes after identifying boundary edges of the mesh 51

Figure 4.11 : An example of creating a vector list for a given mesh edge set 53

Figure 4.12 : The schematic description of the algorithm for extracting the holes with an example 54

Figure 4.13 : Example of a B-spline curve with control points and corresponding basis functions 55

Figure 4.14 : Original MR image and its extracted sets of points (top) and overlay constructed curves onto the original image (bottom) 56

Figure 4.15 : Example of vector field kernel with radius R and its related terms..... 58

Figure 4.16 : Several closed active contours initialized on a MR image (left) final segmentation result for detecting the true boundary of the organs in the image (right)..... 59

Figure 5.1 : Original images containing single objects for testing Hessian reconstruction algorithms and their corresponding anisotropic adaptive meshes..... 61

Figure 5.2 : Zoom-in on resulting adapted meshes constructed based on three methods; the approach by Farid & Simoncelli (left), the QF approach (middle), and our proposed approach (right) 62

Figure 5.3 : Element skewness on the adapted mesh obtained by the QF approach for axis-aligned and non-axis-aligned edge directions 63

Figure 5.4 : Element skewness on the adapted mesh obtained by our proposed approach for axis-aligned and non-axis-aligned edge directions 63

Figure 5.5 : Extracting the anisotropic elements (aspect ratio ≥ 2) from resulting meshes for the three approaches for the Circle example and their corresponding histograms 65

Figure 5.6 : Anisotropic adaptive meshes constructed based on the three mentioned approaches for the given MR image of the human trunk 66

Figure 5.7 : Extracting anisotropic elements (aspect ratio ≥ 2) from resulting meshes for the three approaches for a MR image and their corresponding histograms 67

Figure 5.8 : Original MR image at the top and three mesh-based representations (isotropic, QF, proposed method) and their corresponding reconstructed images 69

Figure 5.9 : Image reconstruction error over different types of adaptive meshes with different sizes 70

Figure 5.10 : Comparison between QF method and proposed method on a series of MR images 71

Figure 5.11 : Original MR images of a human arm (left) Multiple active contour initializations (right)..... 72

Figure 5.12 : Original MR image of human trunk sections (left) Multiple active contour initializations (right) 73

Figure 5.13 : Comparison of automatic initialization on a MR image (example 1) 75

Figure 5.14 : Comparison of automatic initialization on a MR image (example 2) 75

Figure 5.15 : Comparison of automatic initialization on a MR image (example 3) 76

Figure 5.16 : Comparison of automatic initialization on a MR image (example 4) 76

Figure 5.17 : Comparison of automatic initialization on a MR image (example 5) 77

Figure 5.18 : Comparison of automatic initialization on a MR image (example 6) 77

Figure 5.19 : Evolving the initial contours to obtain final segmentation. Initial contours in red (left) Segmentation results in green (right) 79

Figure 5.20 : Comparison of segmentation result corresponding to initialization in figure 5.13 ..81

Figure 5.21 : Comparison of segmentation result corresponding to initialization in figure 5.14 ..81

Figure 5.22 : Comparison of segmentation result corresponding to initialization in figure 5.15 ..82

Figure 5.23 : Comparison of segmentation result corresponding to initialization in figure 5.16 ..82

Figure 5.24 : Comparison of segmentation result corresponding to initialization in figure 5.17 ..83

Figure 5.25 : Comparison of segmentation result corresponding to initialization in figure 5.18 ..83

Figure 5.26 : Original image of human lumbar spine, its model initialization, and segmentation (top), selected initialization and segmentation of intervertebral disks (bottom) 85

Figure 5.27 : Initial contour for an intervertebral disk (left), comparison between our segmentation in green and manual segmentation in white (right) 86

Figure 5.28 : Graph of Dice similarity results for all dataset 87

Figure 5.29 : Original image (left) and its proposed initialization with white contours superimposed on it to indicate the missing parts (right) 89

Figure 5.30 : The other three methods also failed to capture the bone structures in the example image in figure 5.27 90

LIST OF SYMBOLS AND ABBREVIATIONS

MRI	Magnetic resonance imaging
MRF	Markov random field
EM	Expectation maximization
FCM	Fuzzy c-means
CT	Computed tomography
OORT	Object-Oriented Remeshing Toolkit
QF	Quadratic Fitting
GVF	Gradient Vector Flow
CoD	Center of Divergence
FFS	Force Field Segmentation
PIG	Poisson Inverse Gradient
VFS	Vector Field Convolution
DSC	Dice Similarity Coefficient

CHAPTER 1 INTRODUCTION

1.1 Context

Magnetic resonance imaging (MRI) has become a useful diagnostic tool in numerous fields of biomedical by providing high-resolution anatomic information on human soft tissue [1]. This imaging modality is non-invasive and does not require ionizing radiation. The scanner (figure 1.1) uses the property of nuclear magnetic resonance to create images. When the human body (which is mostly water) is placed in a strong magnetic field, the protons in the hydrogen atoms tend to align themselves with the field and result in a net magnetization of the body. This net magnetization can be pushed away from equilibrium by selectively exciting regions within the body with radio waves at an appropriate frequency. When eventually it returns to equilibrium (relaxation) it generates a radio-frequency electromagnetic signature, which can be measured and analyzed. MR imaging is able to provide high contrast sensitivity for visualizing differences among the tissues in the body because there are several sources of contrast. The contrast in an MR image is controlled both by the characteristics of the externally applied excitation and also the intrinsic properties of the tissues, which affect the relaxation times. Therefore these flexible characteristics of MR images allow varying the contrast between different tissues and highlighting various components in order to reveal fine details of the anatomy [2].

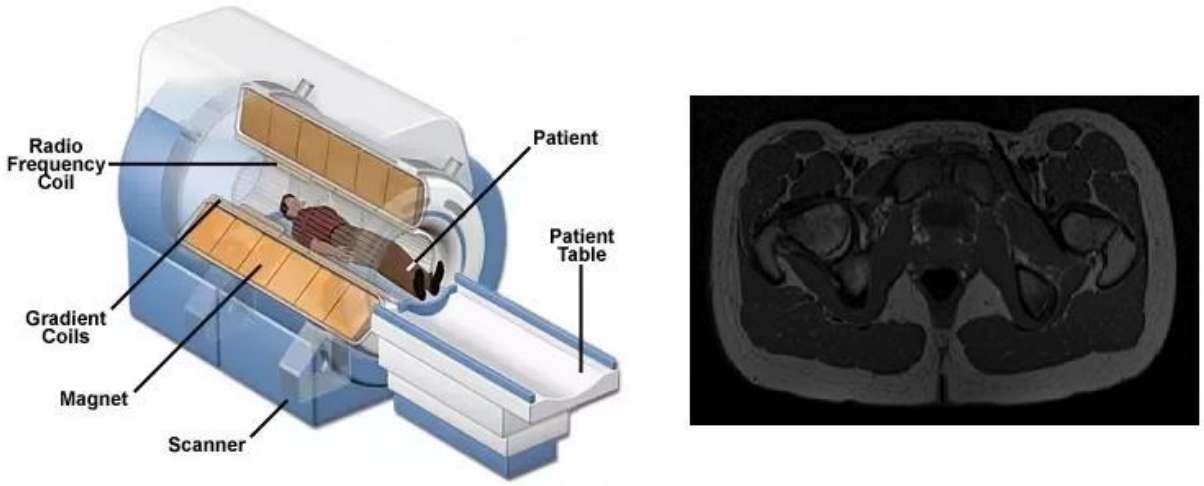

Figure 1.1 : MRI scanner cutaway (left) and an MR image of human trunk (right)

The problematic properties of MRI are intensity inhomogeneity and noise, which arise from the limitations of imaging devices. Due to the presence of this non-uniformity in the image, the intensity varies in different parts of the same tissue within the image. Although this is an imperceptible issue for a human observer, some image analysis methods which are sensitive to intensity variations, such as segmentation, encounter difficulties in identifying tissues based only on pixel intensity. It is very hard to rectify intensity inhomogeneity and noise from MR images because the non-uniformity patterns vary from patient to patient and from slice to slice. There are many methods that have been proposed for correcting the intensity inhomogeneity in MRI [3], but it is still not a completely solved problem, and we have to tackle this obstacle in the segmentation process. It is worth pointing out that intensity inhomogeneity correction and segmentation are two connected procedures and improvements in segmentation can boost non-uniformity correction. According to [3], there are some approaches for inhomogeneity correction which are segmentation-based methods. They try to merge two procedures so that they benefit from each other, simultaneously, in order to yield better segmentation and inhomogeneity correction.

Due to the distinctive characteristics of MRI, it plays a supplementary role in disease management from diagnosis to treatment planning and progress monitoring. Moreover, the creation of 3D patient-specific models out of these images for simulation purposes is becoming a beneficial application. Clinical interpretation of these medical images including segmentation, identification, and analysis of anatomical structures is an essential task which, for images with complicated shape and topology, is very challenging. Unlike traditional medical image analysis which has focused on a single organ or tissue applications, recent technological advances have brought increasing interest in simultaneous analysis and multi-object segmentation of medical images. Despite extensive research and methodological advances, there are still several issues that remain to be solved, and there is a high demand for a widely applicable automatic segmentation and classification technique which is able to handle all anatomical structures. New algorithms and technologies need to be investigated to meet these demands while preserving overall performance.

1.2 Motivation

MR image segmentation which is the process of extracting anatomically significant regions from the image is a challenging and important task in MR image analysis. Moreover, there is a growing need for automatic segmentation of multiple organs and complex structures from this medical imaging modality. Segmentation of multiple objects should provide a decomposition of the image into several components without overlap between the segmented regions.

In literature dealing with MR image segmentation, the region-based approaches which are looking for intensity similarities and try to group pixels into coherent regions, are sensitive to noise and non-uniformity in the input image. The edge-based approaches where use only the intensity discontinuities to determine region boundaries are challenging to group the edge information into a coherent closed contour. The atlas-based techniques which provide prior information for MRI segmentation can be problematic for complicated structures with anatomical variability. A class of variational methods known as deformable models has a great potential to confront MR multi-object segmentation challenges. These model-based techniques are designed to determine region boundaries using closed parametric curves that deform under defined force terms such that the curves are attracted to the image features (e.g. edges) while maintaining internal shape constraints. The main reasons why they are favored in MR image segmentation related to their robustness to noise and spurious edges, mathematical consistency, and sub-pixel accuracy. However they still have an important limitation which is that they are sensitive to initial position and shape of the model. An unsuitable initialization may provide failure to capture the true boundaries of the regions.

On the other hand, a useful aim for an automatic multi-object MR segmentation is to provide a model which promotes understanding of the structural features of the distinct objects within the MR images. However, the lack of connectivity of edge point features is a major limitation to aggregate edge points into a coherent closed curve for every distinct object and obtain initial models automatically only from edge points. Therefore we have to find richer information that is available from edges. The current automatic initialization methods which have used different descriptors such as gradient vector flow or Poisson inverse gradient are not completely successful in extracting multiple objects from MR images. But, the improvement trend of the results by

using higher level descriptions indicates that, providing more abstract level of information enhance the performance of the automatic initialization of the model.

In this regard, anisotropic adaptive meshes seem to be a potential solution to the aforesaid limitation. Mesh-based image representations facilitate the use of non-uniform sampling and have proven beneficial in many image analysis applications. To generate a mesh model of an image, the image domain is partitioned into a set of elements and then over each element an approximating function is constructed. Anisotropic mesh adaptation uses edge and gradient information of an image to provide a sort of structure tensor which is defined as a symmetric and positive semi definite matrix to modify the elements size and orientation in a specific manner. This structure tensor has two orthogonal eigenvectors and the corresponding eigenvalues which can be used to reveal more robust and accurate information about edge structure and orientation. Eigenvectors point in the direction orthogonal across the local edge, with the eigenvalues indicating the strength of the directional intensity change. Furthermore, the eigenvalues can be used as descriptors of local structure as it is shown in figure 1.2.

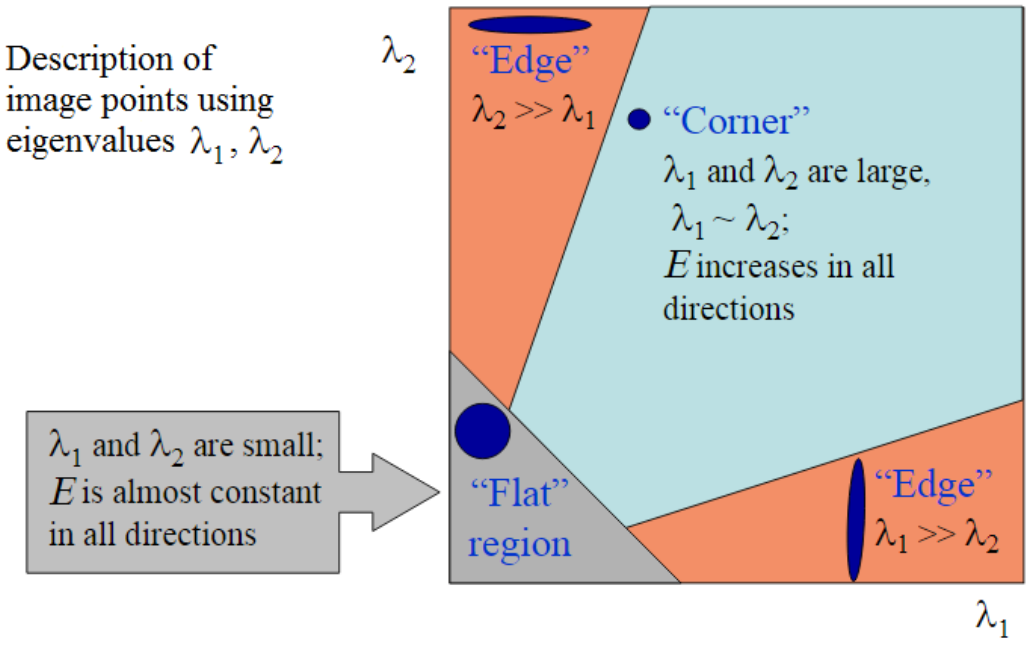

Figure 1.2 : Understanding local structure based on eigenvalues where *E* is the change of intensity for a small shift

Accordingly, anisotropic adaptive meshes constructed from MR images contain higher level, abstract information about the anatomical structures of the organs within the image retained as the elements shape and orientation. Adaptive mesh strategies try to specify metric tensors based on edge points information to control mesh elements characteristics so that they can align with the boundaries of the objects within the image. Existing methods for constructing metrics out of image features have a practical limitation where manifest itself in inadequate mesh elements alignment to inclined edges in the image. Therefore, we also have to enhance metric computation technique in mesh adaptation process to provide a better mesh-based representation. As we can provide a better mesh element alignment to the boundaries of the objects in the image, we may enhance the multi-object extraction process afterward.

Based on these insights, this thesis is going to introduce a new segmentation approach by integrating adaptive mesh generation techniques and deformable models to delineate the geometric structure of different structural objects in MR images.

In this research project, we have mainly focused on 2-dimensional MR images of the human trunk and try to segment all structural organs and tissues in these images. Since this is a very challenging and sophisticated case to handle, we expect our approach to be readily generalizable, and the proposed algorithms to be applicable to other kinds of MR images, thereby having an impact in the field of biomedical engineering.

1.3 Organization

Following the above introductory chapter, this thesis is organized as follows.

Chapter 2 provides relevant literature on three main topics. The first topic is about mesh concepts, mesh generation and adaptation techniques, and mesh-based image representation methods. The second topic is related to MR image properties and existing segmentation techniques for MR images with more details on deformable models as state-of-the-art methods. And the third one reviews current methods for multi-object medical image segmentation. The existing methods in each field are discussed with their advantages and limitations which are going to be addressed in the proposed methodology.

Chapter 3 summarizes the limitation of the existing approaches and presents general and specific objectives of the research project to address those limitations and also provide an overview of the proposed methodology.

Chapter 4 provides the details about the proposed methodology for developing a new mesh-based method for multi-object MR image segmentation.

In chapter 5, experiments and results are discussed. Finally, in chapter 6, conclusions and future research directions are presented.

CHAPTER 2 BACKGROUND & LITERATURE REVIEW

In the three sections that follow, we review the relevant literature to provide a clear understanding about challenges and opportunities in multi-object MR image segmentation towards our general methodology. First we provide a brief introduction to the mesh generation and mesh adaptation process along with literature review addressing the mesh-based image representations and their applications in medical image analysis including segmentation. Since the anisotropic adaptive mesh will be used to provide a roughly representation of multiple objects in the image, then we need to employ a segmentation technique to obtain the exact boundaries of the objects. In this regard we survey various segmentation techniques by emphasizing on active contour model as great candidates for segmenting multiple objects from MR images. The advantages of active contours and their limitations are discussed and the methods which address these limitations are investigated.

2.1 Mesh Generation and Adaptation

A mesh is a discretization of a continuous domain into simple elements such as triangles or quadrilaterals in two dimensions. The elements and their connectivity express the geometry and topology of the spatial domain. The shape and orientation of the elements affect both efficiency and accuracy of the mesh-based methods in scientific applications [4].

Generating meshes can be done in two different manners. Structured methods generate meshes with regular connectivity where all the vertices have the same number of neighbors, and all interior vertices are topologically alike (grid of quadrilaterals in 2D shown in figure 2.1). Structured meshes provide simplicity and easy data access, but they have lower geometrical flexibility. On the other hand, unstructured methods generate meshes with irregular connectivity where the number of neighbors may vary for different vertices (set of triangles in 2D shown in figure 2.1). Unstructured meshes are more costly to access, but they offer geometrical flexibility and more convenient mesh adaptivity for complicated domains.

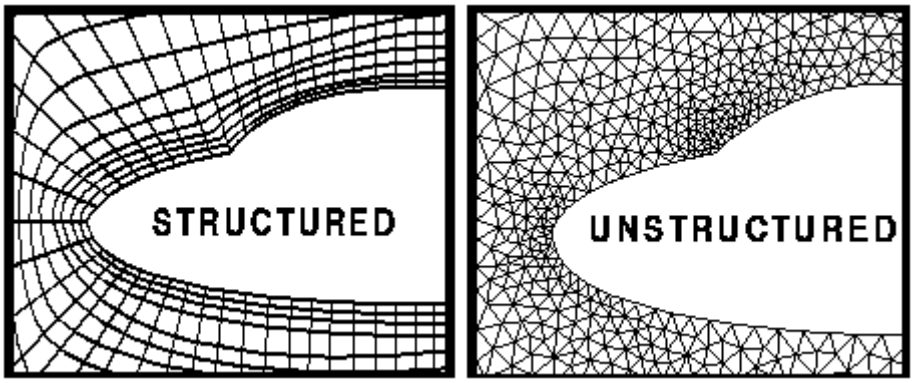

Figure 2.1: Different types of meshes structured (left) and unstructured (right)

Since the domains that are studied in this research are medical images and they usually contain complicated structures, unstructured meshing methods are chosen over structured methods.

Mesh adaptation refers to the modification of an existing mesh as to conform to physical features of the domain. The goal of these modifications is to achieve higher resolution of the domain features and lower overall computational time for respective applications [5-9].

Mesh adaptation methods try to modify the meshes by controlling the size, shape, and orientation of mesh elements throughout the domain and in this regard, they can be categorized into two types; isotropic vs. anisotropic.

Traditionally researchers have focused on isotropic mesh adaptation where only the size is specified for mesh element modification, and there is no stretching and orientation. Therefore, the triangles (mesh elements) in the result mesh are close to equilateral (figure 2.2). This can only be optimal if the gradients of the domain features are almost equal in all spatial directions. The alternative approach is an anisotropic mesh adaptation in which the mesh modifications are controlled to simultaneously adjust the size, shape, and orientation of mesh elements [9-13]. Thus, if the features of the domain are highly directional and the variation in one direction is more significant than the others, the triangles in the resulting mesh are stretched and aligned with directional properties (figure 2.3).

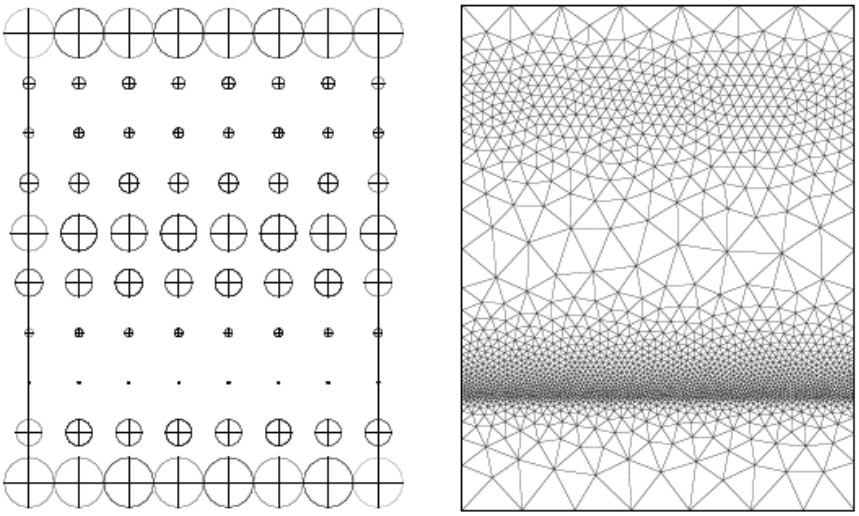

Figure 2.2: Size specification map and the corresponding isotropic mesh adapted based on the specified sizes [10]

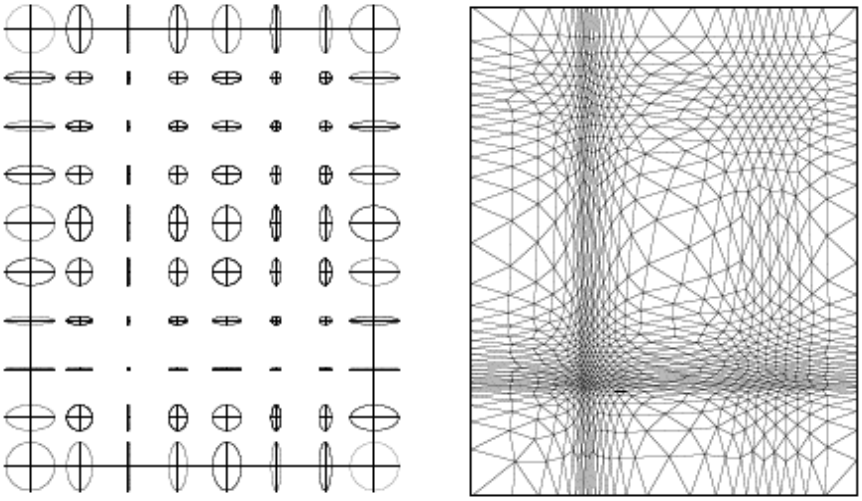

Figure 2.3: Anisotropic map of a domain and the corresponding anisotropic mesh adapted based on the specified size, stretching and orientation [10]

Since the domain features studied in this project are the edges from the outline of the objects in the image and they are strongly directional, an anisotropic adaptation approach is chosen over an isotropic one. In the following, more details on anisotropic mesh adaptation are provided.

2.1.1 Anisotropic Mesh Adaptation

As mentioned before, the idea of mesh adaptation is to modify the mesh according to the domain features by controlling size and orientation. As a result, in areas of high variation in the domain, elements are fine and highly stretched, and in areas of low variation, elements are coarse and more regular. In this regard, the concept of metric is used to specify the mesh size in different directions and orientation. This is also called metric-based anisotropic adaptation.

2.1.1.1 Metric Notion

A Metric is a function defined over a domain that maps any point in the domain to a 2×2 matrix (in 2-dimensions) and expresses how long and skinny the triangles should be and in which direction they should be oriented. In another word, at each point, a metric determines how distances and angles are measured.

Geometrically, distance can be measured by the dot product between two vectors which is symmetric, positive, and definite. In 2×2 Euclidean space, for two vectors u and v the dot product is indicated in Eq. 2-1 and the length of a segment ab is given by Eq. 2-2.

$$\langle \vec{u}, \vec{v} \rangle = {}^t\vec{u}\,\vec{v} \tag{2-1}$$

$$\ell(a,b) = \sqrt{{}^t\overrightarrow{ab}\ \overrightarrow{ab}} \tag{2-2}$$

In Euclidean metric space, the dot product is generalized by introducing a 2×2 symmetric positive definite matrix as $\mathcal{M} = \begin{bmatrix} a & b \\ b & c \end{bmatrix}$.

In this space, the distance definition is shown in Eq. 2-3 and length of the segment ab is given by Eq. 2-4.

$$\langle \vec{u}, \vec{v} \rangle_{\mathcal{M}} = {}^t\vec{u}\,\mathcal{M}\vec{v} \tag{2-3}$$

$$\ell_{\mathcal{M}}(a,b) = \sqrt{{}^t\overrightarrow{ab}\,\mathcal{M}\,\overrightarrow{ab}} \tag{2-4}$$

In the context of mesh adaptation, a Riemannian metric space defined by $M = (\mathcal{M}(x))_{x\in\Omega}$ represents $\mathcal{M}$ as a Riemannian metric over the space of parametrization Ω. To consider the variation of the metric along the segment ab the length is computed using the straight line parametrization in domain Ω with an integral formula as in Eq. 2-5.

$$\ell_{\mathcal{M}}(a,b) = \int_0^1 \sqrt{{}^t\overrightarrow{ab}\,\mathcal{M}(a+tab)\overrightarrow{ab}}\ \mathrm{dt} \tag{2-5}$$

Where $t \in [0,1]$.

2.1.1.2 **Geometric Representation of Metrics**

In the above equations, the metric $\mathcal{M}$ which is also called a metric tensor, has geometric representation in the form of an ellipse [14]. Since this metric tensor is symmetric, it is diagonalizable and can be decomposed as indicated in Eq. 2-6.

$$\mathcal{M} = \mathcal{R}\,\Lambda\,{}^t\mathcal{R} \tag{2-6}$$

$$\Lambda = \begin{bmatrix}\lambda_1 & 0\\ 0 & \lambda_2\end{bmatrix}$$

$$\mathcal{R} = (\overrightarrow{e_1}, \overrightarrow{e_2})$$

where $\mathcal{R}$ is an orthonormal matrix containing the eigenvectors of $\mathcal{M}$ that represent the two axes of the ellipse and Λ is a diagonal matrix containing the eigenvalues of $\mathcal{M}$ specifying two lengths of the ellipse axes as $h_i = \lambda_i^{-1/2}$ as shown in figure 2.4.

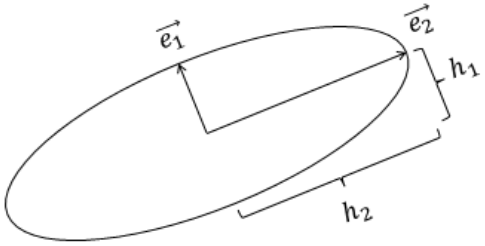

Figure 2.4: Geometric representation of a metric tensor

Geometric representation of metric tensors by ellipses provides a convenient way to visualize the size, stretching, and orientation over the domain for mesh generation and adaptation process.

2.1.1.3 Mesh Adaptation Scheme

There are many software systems for performing anisotropic mesh adaptation and the more recent ones are, Gamanic3d [15], Tango [16], Mesh Adap [17], OORT [18], Feflo.a [19], and MAdLib [20].

The OORT (Object-Oriented Remeshing Toolkit) which was developed by Julien Dompierre and Paul Labbe is the one that has been chosen for this project. The capacity of this tool for metric-based anisotropic mesh adaptation has been shown in [21]. The adaptation process in OORT is performed iteratively as it is shown in figure 2.5.

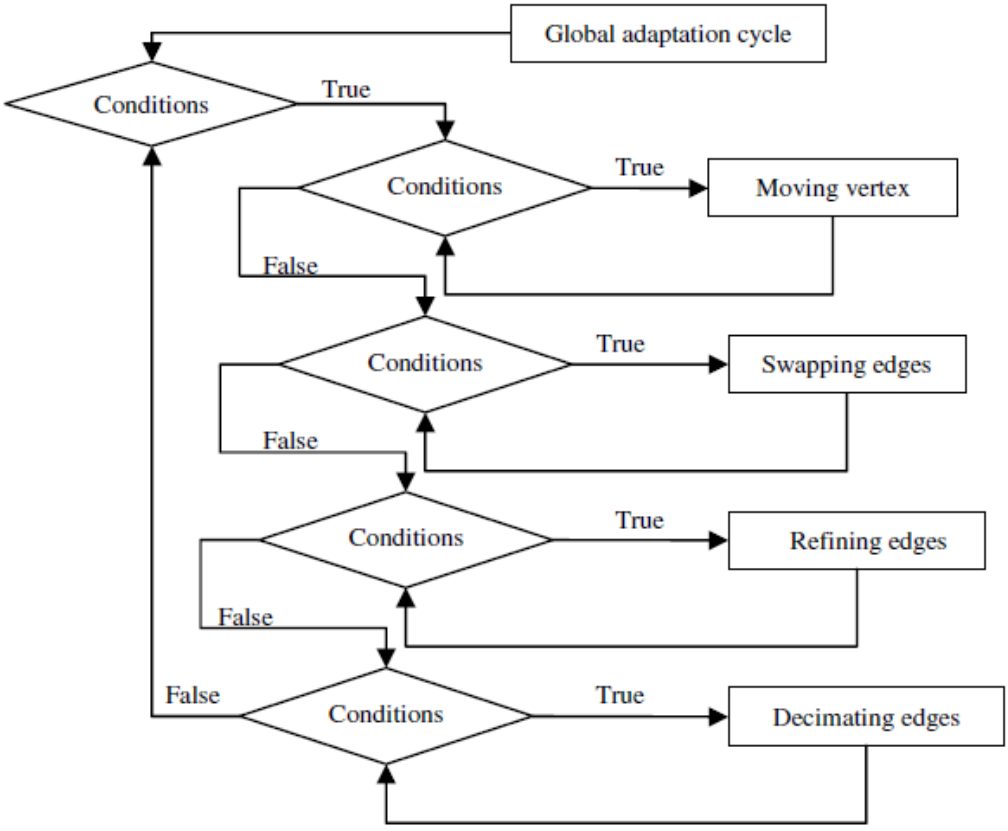

Figure 2.5 : The adaptation process of OORT [22]

In each iteration, any local mesh modification (including moving vertices, swapping, refining, and decimating edges of the elements) is done to satisfy the metric. The final result is a unit mesh in predefined Riemannian metric space in which all elements are quasi-unit while they are adapted and anisotropic in the Euclidean space.

2.2 Mesh-based Image Models

In recent years, researchers have presented numerical simulations in the biomedical field in order to investigate the impact of medical treatments in different areas including cardiology, neurology, orthopedic surgery, etc. Many of these simulators are constructed based on medical images by generating structured or unstructured meshes from the images. Then through an adaptation process, the initial mesh is deformed to follow desirable features within the image. In the scope of this research, desirable features of an image are considered as all the edges in the image that represent boundaries of different regions (in particular, distinct anatomical tissues) within the image. Therefore the process of mesh deformation to conform to the edges involves changing mesh elements size and orientation to align element edges with the boundaries of the regions. As mentioned before, although structured meshes can produce high-quality models, the advantages of using unstructured meshes include generating meshes with fewer elements and the ability to conform better with image features [23, 24]. In this regard, we are going to focus on generating unstructured meshes and anisotropic adaptation processes applied on these meshes. Many of these methods are considered as sampling methods which try to find desired sample points first and then connect the points to construct a mesh [25-35] and a few methods start from an initial mesh and then try to adapt the mesh according to the image content [22, 36-38]. Ramponi and Carrato [33] have introduced non-uniform grids using an irregular sampling scheme based on measuring the change in gray-level values. Yang et al. [31] have represented an adaptive mesh generation technique by placing the mesh vertices using the classical Floyd-Steinberg error diffusion algorithm and then using Delaunay triangulation to connect the vertices. The resulting mesh contains small elements where the gray-level variation is high and large elements in low variation regions. Demaret et al. [27, 28] have proposed an image approximation scheme for the

purpose of image compression which starts with all image points and then removes less significant pixels in a greedy way to reach the smallest reconstruction error. Adams et al. [25] have presented an effective framework based on the greedy point removal scheme of Demaret et al. and the idea of the error diffusion scheme of Yang et al. in order to replace the initial mesh of all image points with a good subset of those sample points. This would provide a flexible tradeoff between mesh quality and computational and memory complexity. Sarkis and Diepold [36] have combined a Binary Space Partition and clustering scheme to present a new method for approximating an image with a mesh. They cluster the image area into a few triangles and try to model the intensity variation inside each triangle and reconstruct the gray level values of pixels lying within. If a triangle's equation does not have the ability to reconstruct those pixel values, it is subdivided recursively based on a predefined threshold. Bougleux et al. [37] have shown that anisotropic sampling and triangulation are crucial to improve image approximation. They have proposed a progressive geodesic meshing that defines geodesic distance using a Riemannian Fast Marching to force the triangulation to follow the anisotropy of the image. However, in their method, the metrics are constructed using first order derivatives which make the eigenvalues physically meaningless. On the other hand, Riemannian metric tensors have been used to control the anisotropic adaptation of meshes. These metric tensors in the case of images are constructed based on second order derivatives of the intensity of the image at every pixel. Several approaches have been presented for the computation of second order derivatives of images. Vallet et al. [39] have compared different methods such as: Double linear fitting (DLF) [40], Simple linear fitting (SLF) [41], Double L^2-projection (DL2P) [42], and Quadratic fitting (QF) [43]. The common feature of all these methods is that they try to find an approximation of the image function at each pixel and then the partial derivatives of these functions will be derived to construct the Hessian matrix for all pixel intensities. Among these second derivatives recovery methods, they suggest that, the QF method which fits a least-square quadratic polynomial on a two neighborhood levels patch is more robust and more accurate. O. Courchesne et al. [22] have applied the QF method on MRI images to compute a Hessian matrix and construct metric tensors for mesh adaptation processes. The result in figure 2.6 shows that this approach only works perfectly for edges in vertical and horizontal directions and for other directions it can align element edges with the oriented boundaries but not as perfectly as in the main two directions.

Several methods have been proposed for computing image derivatives using special convolution filters such as Steerable filters [44] and least-squares polynomial smoothing [45]. Farid and Simoncelli [46, 47] have provided a discrete representation of their continuous differentiation scheme as some optimized differentiating filters which are commonly used in practice. Their method has demonstrated more accuracy in estimating local orientation in images. However, the result of constructing a metric based on the image derivatives is shown in figure 2.6 which only gives proper alignment in horizontal and vertical directions and fails to be aligned in other directions.

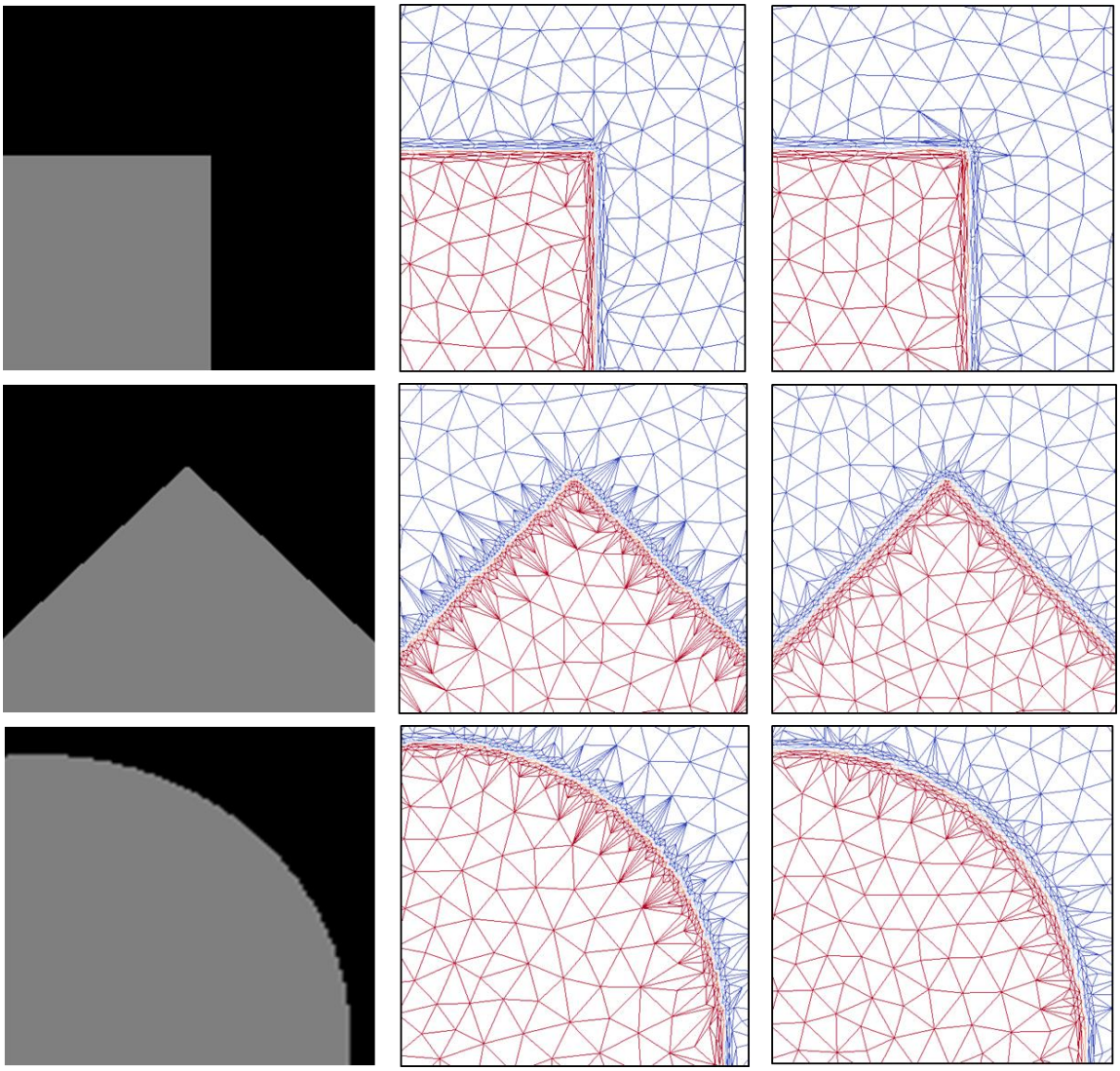

Figure 2.6 : Three examples of simple images with edges in different directions (left), corresponding adaptive meshes by spatial convolution filtering approach (middle), and corresponding adaptive meshes by geometric approximation approach (right)

In summary, the above literature review indicates that the main limitation of the existing approaches for anisotropic mesh adaptation is their inadequate alignment for non-axis aligned edge directions. Therefore we need to construct an adaptive mesh for a given image in which elements of the mesh become aligned with the boundaries of the objects in any directions.

As mentioned before, we want to incorporate anisotropic mesh adaptation and segmentation methods to present an automatic multi-object segmentation technique. In this regard we survey various segmentation techniques for MR images in the following section.

2.3 MRI Segmentation Techniques

In this section, we review some of the current methods in MRI segmentation and the state-of-the-art related to the proposed segmentation framework. A large and growing body of literature has been published which can be divided into three main categories: classification-based, region-based and contour-based techniques. In the following sections, we discuss the characteristics, advantages, and disadvantages of these methods.

2.3.1 Classification-Based Techniques

In classification-based methods, segmentation is the process of classifying pixels into certain tissue classes based on some specific criteria. One class of techniques in this category is statistical pattern recognition models, which have been applied extensively in MRI segmentation [48]. A mixture model is used to model the probability density function of tissue classes. A set of features based on pixel information is provided in order to measure the probability of pixels belonging to each class. Generally, to characterize the variation of each pixel feature, a class conditional probability distribution is needed which is generally unknown [49]. In supervised approaches, these distributions will be provided based on the tissue regions identified by the user. In statistical clustering [50], they can be approximated automatically based on the image data in an iterative way. On the other hand, some of the statistical methods, which are considered as parametric methods, assume that the conditional distribution of classes is known and often model

them as a mixture of Gaussians [51]. Many statistical methods assume that the number of tissue classes and a priori probability of their occurrence are provided prior to the segmentation process. Then, in order to estimate a posteriori probability, the Bayes rule is employed, and pixels are assigned to the class with highest a posteriori probabilities [52]. Markov random fields (MRF) are introduced to incorporate local contextual information which allows neighbourhood pixels to affect segmentation. MRF also provides reliable information to model the possible neighbourhood for each tissue class [53]. A recent study shows that MRF regularization allows modelling the spatial interaction in neighbourhood space [54]. Another implementation of statistical clustering for tissue identification is based on a 3-step expectation maximization (EM) algorithm [55, 56]. This iterative procedure also assumes tissue classes as a mixture of Gaussians and creates a model with MRF regularization in order to reduce segmentation errors arising from intensity inhomogeneity and noise. Although statistical techniques result in a significant improvement in MRI segmentation, they are still not powerful enough to yield automatic and accurate segmentation, in the general case [57].

A popular class of pixel clustering methods is based on a fuzzy clustering technique, derived from the fuzzy c-means (FCM) algorithm [52]. The FCM and its derivatives have been found very successful in medical image segmentation particularly in those cases where distinctive decisions have to be made. Clustering algorithms allow image pixels to be grouped together based on similarity of the description features. Unlike hard c-means algorithms which assign an absolute membership to one of the classes, the FCM algorithm assigns a degree of membership to each of the classes. Some adaptive methods based on FCM have been applied to MRI segmentation [58, 59]. These methods implement a modified objective function for FCM to model the variation in intensity value and help to amend the intensity inhomogeneity problem. However, they do not pay attention to spatial context between pixels because the procedure is done in the feature space and this limitation makes them sensitive to noise and image artefacts. Some alternative approaches have been proposed to consider spatial constraints and reduce errors caused by noise [58, 60], but they induce a higher computational complexity and are time-consuming.

Some recent studies [61, 62] have presented visual features for capturing spatial context for detection and localization of anatomical structure in CT images, and they plan to extend their technique to MR images. They have incorporated those features within a random decision forest

classifier. A random forest [63] is a collection of randomly trained decision trees. Decision trees were once very popular, but researchers have stopped using them because they suffer from the over-fitting problem and consequently they don't tend to generalize and provide well prediction. After coming along the idea of bias-variance trade-off, it was found that even though trees have very high variance in their predictions, if you make many trees and average them, you can get rid of the variance and build one of the most powerful classifier called random forest. A Random forest is a kind of ensemble model, and the algorithm simply takes the trees, sums them and divides by the number of trees. The algorithm has two sources of randomness, one is the randomness of the input data, and the other one is the randomness in the features. Injecting such randomness improves generalization. So, by randomly choosing input data and features for different trees, each tree only sees a small part of the data and features. Each tree is correct but missing a lot of information, but when we average them, we get a classifier which is very near the truth. Just like the forest can be used for classification, it also can be used for regression. A split point is introduced which divides the data into two nodes, and then in each node, a linear model is fitted. The aforesaid techniques built upon randomized decision forests for detecting anatomical structures have been enriched with learned visual features which capture long-range spatial context. Although they have presented satisfactory result in the case of CT images and might be extendable to MR images, they have focused only on some specific human organs. In order to consider all organs and tissues and moreover to introduce general-purpose classifier, further generic features need to be defined.

2.3.2 Region-Based Techniques

Another way of describing the objects in the image is by determining the region they occupy. Usually, the pixels within an object have similar intensity or texture characteristics. Accordingly, region-based methods make efforts to identify homogenous regions in the image in order to segment various objects. Region-based techniques, unlike clustering approaches, try to embody spatial properties between pixels and neighborhood information. Thresholding [64] approaches are the simplest techniques which try to find a threshold value to differentiate between tissue regions in the image. Although these methods are computationally fast, in the presence of noise and intensity inhomogeneity, it becomes very difficult to determine thresholds accurately.

Another simple idea is to determine some seeds indicating different regions and let them grow until the entire image is covered [65, 66]. In this regard, for controlling the growing process, some rules or tools must be provided to check the similarity at each growth step. One class of region-based approaches which has been used for MRI segmentation is region growing. These methods start by locating the seeds in the image and check the neighborhood pixels with predefined homogeneity criteria to identify biological segments [67]. Most of these techniques are semi-automatic and rely on user interactions. Also, some automatic statistical forms of these methods have been proposed. They estimate local mean and variance for each pixel and try to find the best parameter via a minimization function, but in the general case, they encounter some difficulties in determining a proper homogeneity criterion in advance [68]. In this regard, an adaptive technique was proposed which attempts to learn the criteria automatically, based on the characteristics of the regions during the segmentation process [69].

Split and merge techniques are another set of region-based methods that operate on an image in a recursive way. They start with entire images and check intensity homogeneity, and if pixels are not all of a similar intensity, the volume is split into smaller sub-regions, and the same process is applied to sub-sections. In the merge step, the inverse direction is followed, and the small regions are joined together if they have enough similarity [70]. In the case of medical images, the major problem is when the image contains many small sub-regions with variable sizes which cause over-segmentation difficulties.

2.3.3 Contour-Based Techniques

Several attempts have been made to segment biological and anatomical objects in MR images by detecting their boundaries. This group of approaches is categorized as contour-based segmentation techniques.

A notable idea in the class of edge detection methods suggests combining Marr-Hildreth and morphological operators for edge detection and edge refinement in MRI segmentations [71]. Some other studies based on edge tracing, which is commonly used in image processing, try to extract edge information and trace the adjacent connectivity to represent the object boundaries [72]. Typically they are not applicable for segmentation problems on their own, because their

information is based on local intensity variations and may not always result in a closed form and connected boundaries. Some studies have been done to produce suboptimal results and also reduce computation time, but they are restricted to segmentation of large and well-defined structures [73]. Generally, these boundary-based methods tend to be sensitive to noise and image artefacts and may suffer seriously from over and under-segmentation due to the inaccurate threshold selection [74]. Some MRI segmentation approaches are based on the watershed algorithm. They choose to model MR images as topographic reliefs where intensity values of voxels determine the physical elevation. The watershed method subdivides the image into basic elements, called catchment basins and considers each one has a local minimum. By imagining a hole at each local minimum of the topographic relief, as the catchment basins are filled with water, the surface will be immersed starting from the basin which is associated to the global minimum. As soon as water flows from one catchment basin to another, a dam is built. In the end, the borders defined by the watersheds represent the segmentation result [75]. This semi-automatic segmentation method also suffers from an over-segmentation problem in the presence of noise and other artefacts [57]. The images have to be smoothed prior to the watershed operation in order to reduce this adverse effect.

In recent years there has been a considerable amount of literature on a group of contour-based methods known as deformable models. These methods have an increasing influence on medical image segmentation including MRI segmentation. Their distinctive properties, which are discussed in the following, make them state-of-the-art methods for MRI segmentation.

2.3.3.1 **Deformable Models**

Deformable models are used in a very large range of applications such as image processing, surgery simulation, computer animation, etc. Different models can be classified based on their contour representation as it is shown in figure 2.7. The difference between continuous and discrete representation is that in discrete form the geometry of contours is only known at finite sets of points. Continuous forms must be discretized for computational needs, but it is possible to compute normal and curvature along the whole curve.

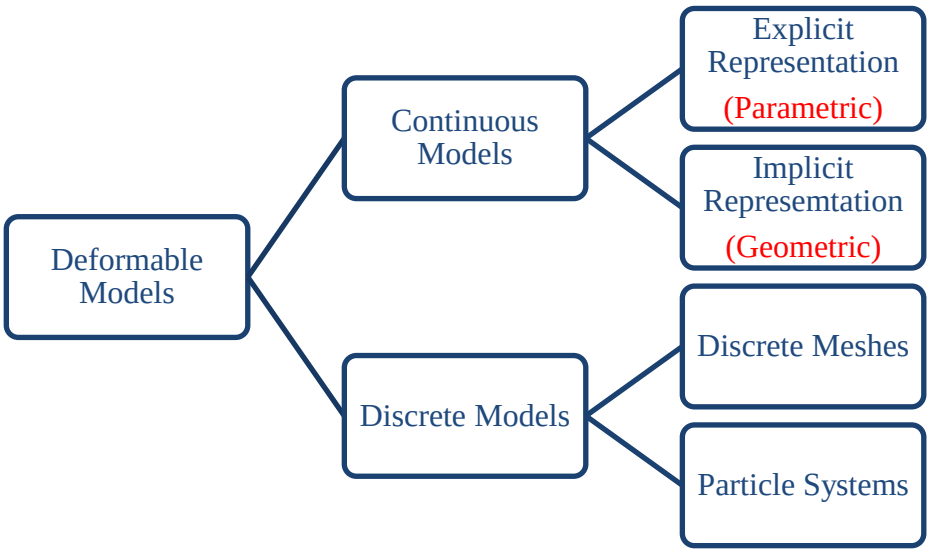

Figure 2.7 : Geometric representation of deformable models

Continuous models have been used extensively for image segmentation while discrete models such as meshes are mostly used for object modelling. There are some advantages in using deformable models in medical images over other segmentation techniques. They are able to generate closed parametric templates from images in a smooth manner, making them robust to noise and spurious edges, and able to manage complex geometries and topology changes (curve splitting and merging). Moreover, they provide consistent mathematical descriptions, which can be used for subsequent applications. Continuous deformable models including active contours (2D) and active surfaces (3D) provide some closed curves or surfaces with the ability of expansion and contraction to fit the objects' boundaries. There are two types of these deformable models: parametric and geometric.

2.3.3.1.1 Parametric Models

Parametric models represent deformable contour that are explicit in their parametric form during deformation. Mathematically, a deformable contour is a parametrized curve $C(s) = [X(s), Y(s)]$; $s \in [0,1]$ where deformation is based on energy minimizing functions. Most of them are derived from snake models [76]. Snake energy formulation is based on internal and external forces as shown in Eq. 2-1:

$$E = E(int) + E(ext) \tag{2-1}$$

Internal energy manifests itself in the smoothness of the shape and is given by Eq. 2-2:

$$E(int) = \int_0^1 \alpha|C'(s)|^2 + \beta|C''(s)|^2 ds \tag{2-2}$$

Where α and β control the tension and rigidity of contours respectively and $C'(s)$ and $C''(s)$ are curve derivatives.

External energy consists of potential forces which usually involve forces derived from the image. The role of the external energy is to make the curve converge towards the edges and is given by Eq. 2-3:

$$E(ext) = \int_0^1 E_{im}(C(s))\, ds \tag{2-3}$$

E_{im} is the edge attraction function and represents the gradient of the image intensity function. Local minima of E_{im} represent the situation where the snake and the edge conform to each other (figure 2.8). It is defined as Eq. 2-4:

$$E_{im} = \frac{1}{\lambda\,|\nabla G_\sigma * I(x,y)|} \tag{2-4}$$

Where λ is a chosen constant, G_σ is a Gaussian function with standard deviation σ, ∇ is the gradient operator, * is the image convolution operator, and $I(x,y)$ is a given gray-level image. So, the curve moves through the spatial domain of an image to minimize the following energy function (Eq. 2-5):

$$E = \int_0^1 [\tfrac{1}{2}(\alpha|C'(s)|^2 + \beta|C''(s)|^2) + E_{im}\big(C(s)\big)]\, ds \tag{2-5}$$

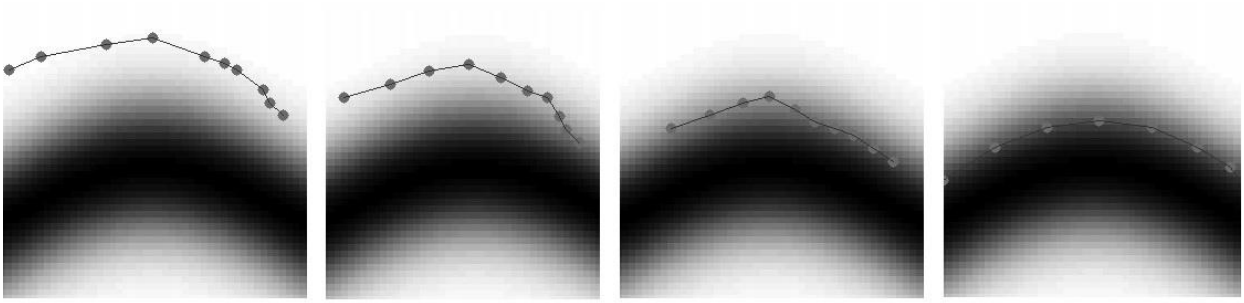

Figure 2.8 : Some iterative steps for parametric curve evolution to fit an edge

Many extensions have been proposed for medical image analysis including segmentation. The first use of parametric models in segmentation was proposed in [77]. The major limitations of their approach are that they can only provide accurate results if the initial curve is given close to the edge and they also detect some spurious edges as real edges of the structures. Although many modifications have been done to traditional snakes to overcome the initial condition and spurious edge problems, they all suffer from noise and other image artefacts due to the fact that they only use the gradients of the image. In order to solve this problem, one study [78] suggests using gradient vector flow (GVF) as a kind of region-based feature to form the external force. They alleviate the problems related to noise and are also able to handle concave objects. However, their method has some drawbacks. The generation of GVF needs intensive computations. Also, weak and strong edges create similar flow because only the gradient information affects the flow. Another problem of traditional snakes is convergence to local minima which makes them improper for noisy images. Another early study [79] suggests a different external force model. They first apply a Gaussian kernel for smoothing and then compute the edge map based on a gradient operator or Gabor filter. They improve the capture range, but this method requires prior information of the object in order to select the initial parameter and produce accurate results. Another research [80] indicates a different formulation of the energy function based on a mean shift technique in order to improve segmentation accuracy and computational efficiency, but it still has initial condition and parameter optimization problems. In addition, several issues still remain unsolved for parametric models such as topological changes, handling multiple objects, and convergence stability. Another class of methods known as geometric models is proposed to handle some of these limitations.

2.3.3.1.2 Geometric Models

Geometric models deform curves or surfaces implicitly as a particular level of a function and using an elegant formulation based on the object geometry. These models comprise two approaches; one is based on curve evolution theory [81] which uses geometric information such as curvatures and unit normal for curve deformation, and another one is based on level set methods which represent curves or surfaces as a level set of a higher dimension scalar function. After complete deformation, the parameterized model is computed.

In the first approach, the curves are parameterized and the energy function can be defined by adding an integral functional on the boundary and another integral functional inside the boundary. Then the contour that minimizes the energy function can be identified by an Euler-Lagrange equation. Let us consider the curve $\boldsymbol{X}(s,t) = [X(s,t), Y(s,t)]$ where s is any parametrization and t is the time. The contour evolution towards the minimum is implemented by the gradient descent equation (Eq. 2-6):

$$\frac{\partial \boldsymbol{X}}{\partial t} = V_{(k)}.\overrightarrow{N}, \tag{2-6}$$

which moves the contour along the normal $\vec{N}$ with the speed function $V_{(k)}$.

In the level set approach [79, 82], a function represents the contour in implicit form and uses a contour of higher order; a 3D surface is used for 2D curves and a 4D hyper-surface for representing 3D surfaces. If Ω is the range of the contour model and function $\phi: \Omega \times \Re^{+} \longrightarrow \Re$ is defined, the task is to analyze and compute deformation under a velocity field. This velocity can depend on position, time, geometry (normal and mean curvature) of the curve and the external physics. The curve is expressed with a function ϕ (figure 2.9) as Eq. 2-7:

$$\boldsymbol{X} = \{x | \phi(s,t) = 0\} \tag{2-7}$$

And the function ϕ has the following properties (Eq. 2-8):

$$\phi(x,t) < 0 \qquad for\ x\ inside\ \Omega \tag{2-8}$$

$$\phi(x,t) > 0 \qquad for\ x\ outside\ \Omega$$

$$\phi(x,t) = 0 \qquad for\ x\ on\ the\ curve$$

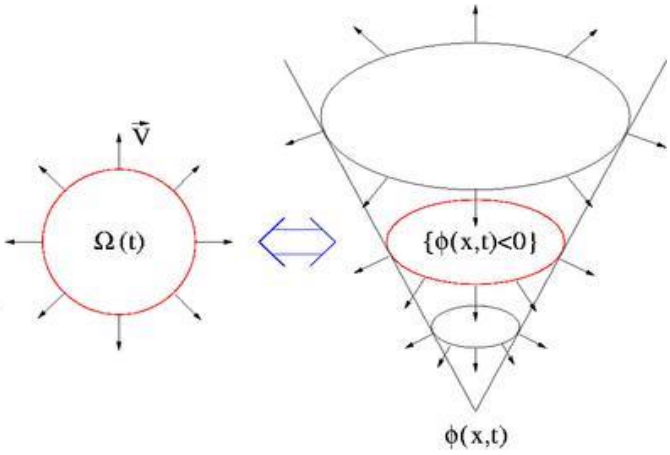

Figure 2.9 : Level set function of a curve

If the curve moves with speed F along the normal $\vec{N}$ as in Eq. 2-9:

$$\frac{\partial \boldsymbol{X}}{\partial t} = F.\vec{N} \tag{2-9}$$

we express the change in the level set ϕ to move according to this speed by Eq. 2-10:

$$\phi_t = \frac{\partial \phi}{\partial t} = |\nabla \phi|.F \tag{2-10}$$

which is much easier to implement than the previous approach. Since the movement or evolution of the curve and the level set function are identical, a curve can be represented as the border between the positive and negative areas of the level set function. An important issue in this approach is that topological merging and breaking are handled naturally (figure 2.10). The

popularity of this approach in MRI segmentation is explained by the fact that it can handle complex geometry and topological changes.

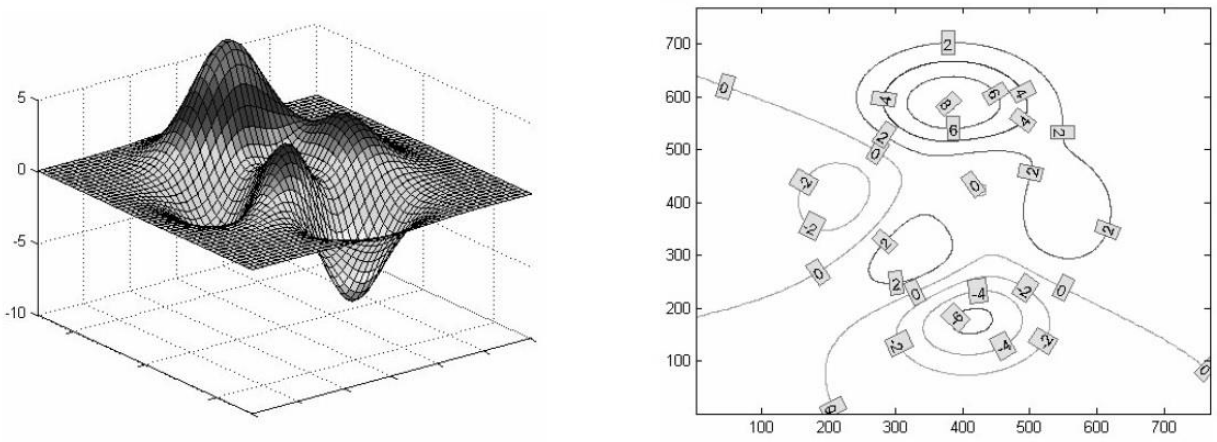

Figure 2.10 : Example of topology changes of the contour for ϕ function

Early methods [83, 84] that have been proposed for MRI segmentation consider the segments as intensity constant regions and ignore the intensity inhomogeneity and noise problems. Some extensions to these methods have been suggested in [85, 86] and although the results have improved, they still have problems with intensity non-uniformity. Mainly because they don't consider the fact that non-uniformity patterns are not similar in different tissue regions. Another study [87] advises to construct the level set model based on Bayesian inference for volumetric image segmentation. They introduce neighborhood statistical analysis in order to overcome disturbances caused by noise and intensity inhomogeneity. A very recent method [88] has presented a new level set approach using a new formulation of the speed function. Although they produce results which are more accurate and less sensitive to noise, they still vary from ground truth. In summary, the level set approach offers good performance in MRI segmentation, but current methods need to be improved in order to overcome the initialization problem and produce more accurate results despite of noise and non-uniformity. Resolving these issues would help to contribute to a fully-automatic and general-purpose segmentation approach.

As mentioned before, discrete deformable models such as meshes (sets of points with some connectivity relations) are mostly used for modeling and have many applications in image processing including medical image analysis. The main issue is how to construct a mesh for

image representation that is well adapted to the content of the image. In the sense of mesh-based segmentation approaches, several efforts have been made to use meshes for image segmentation. The most relevant ones are presented in [89-93] and all of them are based on the same concept but involve different approaches. In [91] they have introduced topological active volume (TAV) which is a structure composed of interrelated nodes. This model is based on polyhedral meshes and represents segmentation by means of a distribution of nodes. The segmentation process is performed by moving the nodes which deform the mesh to detect the objects in the scene. The state of the structure is governed by an energy function. The internal energy is based on first and second order derivatives and controls the shape and structure of the net and the external energy is obtained from intensity value and neighborhood information of the node and guides the adjustment process. They have shown the ability of accommodating topological changes and conforming to concavities and holes. They have also provided some extension to their method [89, 90] in order to improve the adjustment to complex regions and represent better segmentation results. Another method and its recent extension to medical images [92, 93] called whole mesh deformation (WMD) has been proposed with similar assumptions as in the case of TAVs, but with different mesh deformation strategy and different energy formulation in order to improve the efficiency of the model. The internal energy is represented as a combination of mesh continuity and curvature forces and the external energy is defined based on three forces from image intensity, gradient vector flow, and results of a Canny edge detector. The methods show that mesh models are simpler to manipulate than parametric models and allow fast convergence of the models, represent more details about the segmented scenes and offer more efficiency and stability in segmentation procedures. Another semi-automatic approach proposes using anisotropic mesh adaptation in MR image segmentation which has been demonstrated accurate results [94]. The anisotropic mesh is provided by the Object-Oriented Remeshing Toolkit [18] and the segmentation is performed using a thresholding technique on the mesh.

Despite many interesting efforts in using continuous and discrete deformable models for MRI segmentation, there are still a number of drawbacks for these models. The region-based approaches are sensitive to noise and non-uniformity in the input image and the edge-based approaches are sensitive to initial position and shape of the model. An improper initialization of the model might cause entrapment in a local minimum and result in segmentation error. Topology changes and detecting large regions when the image contains more than one object and

when the objects have discontinuities would be problematic in a parametric formulation and would need user interaction over the process. In the following section we review some of the existing literature on initialization of deformable models.

2.3.3.2 **Deformable Model Initialization**

The concluding point from the previous section states that initialization of deformable models is a crucial part which will affect the ultimate result of the segmentation. A suitable initialization can prevent failure caused by entrapment in local minima and help capture the boundary of objects. It will also reduce the number of iterations that the method needs to converge. Although considerable research has been carried out on active model improvement, only a small portion of this research has paid attention to model initialization.

Some of the current methods use manual initialization by selecting some initial points on the image [95, 96]. Although manual initialization is more effective, it is very tedious and time-consuming. Also, it may not always capture the true boundary, due to the limited number of points used (figure 2.11).

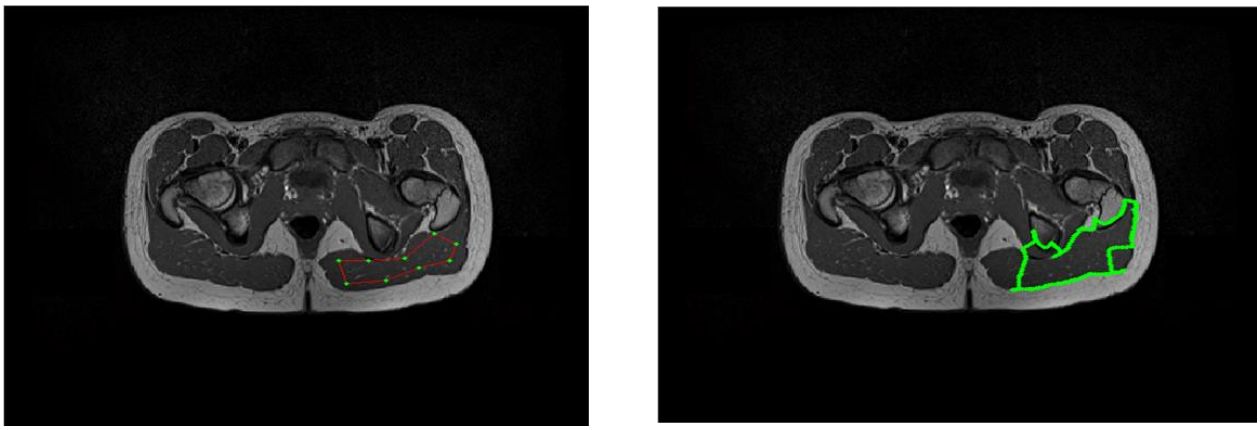

Figure 2.11 : Manual initialization on a MR image (left) and final segmentation result (right)

Some other models employ simple geometric models such as circles (2D) which may need many iterations to converge and also may not converge to the desired features due to noise and artifacts in the image (figure 2.12).

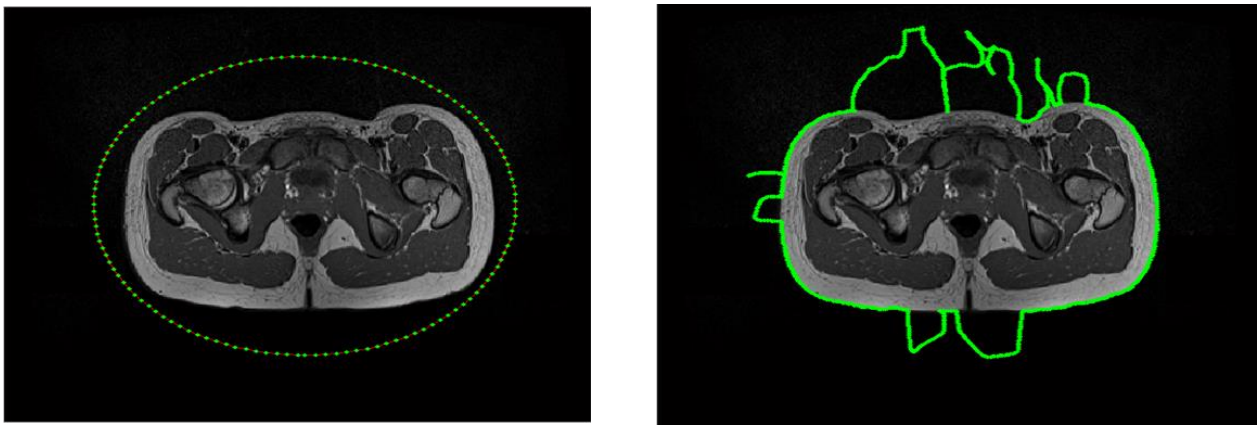

Figure 2.12 : Simple model initialization on a MR image (left) and final segmentation result (right)

There have been several investigations on automatic initialization. Ge et al. [97] proposed a method to start multiple active contours based on some points called Center of Divergence (CoD) computed by Gradient Vector Flow (GVF) field. In the CoD method presented by Ge and Tian [97], some points are computed from a gradient vector flow field, which are called centers of divergence. Then multiple active contours are initialized by locating circles which are centered on these points like the examples in figure 2.13.

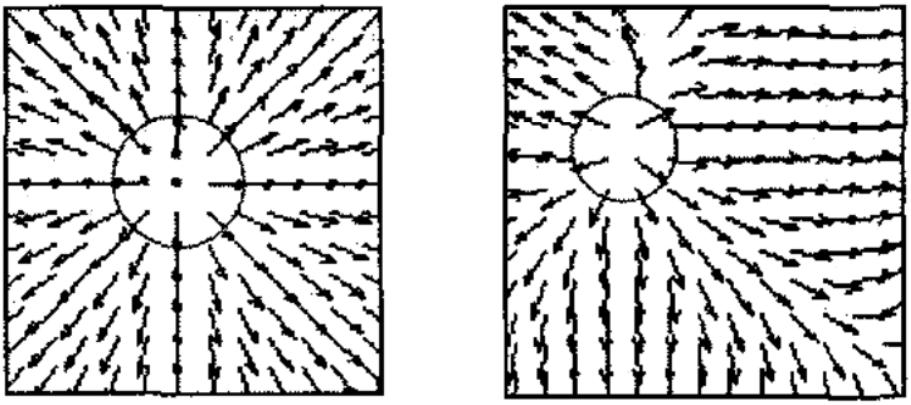

Figure 2.13 : Part of GVF fields and centers of divergence marked by circles [97]

Their approach is suitable for simple images, but for complex images, it is difficult to determine an appropriate set of CoD. Tauber et al. [98] generalized the notion of CoD by representing a skeleton of divergence, but it needs the starting point to be determined by the user. They also presented a method [99] based on a GVF field combined with anisotropic diffusion in order to improve the results, but this method is also considered as quasi-automatic and needs user interaction. Another method named Force Field Segmentation (FFS) was introduced by Li et al. [100]. They have proposed a new external force field named edge preserving gradient vector flow (EPGVF). With the help of graph representation and a graph theory approach, the EPGVF field is segmented first as shown in figure 2.14, and then multiple active contours are individually initialized within each segment.

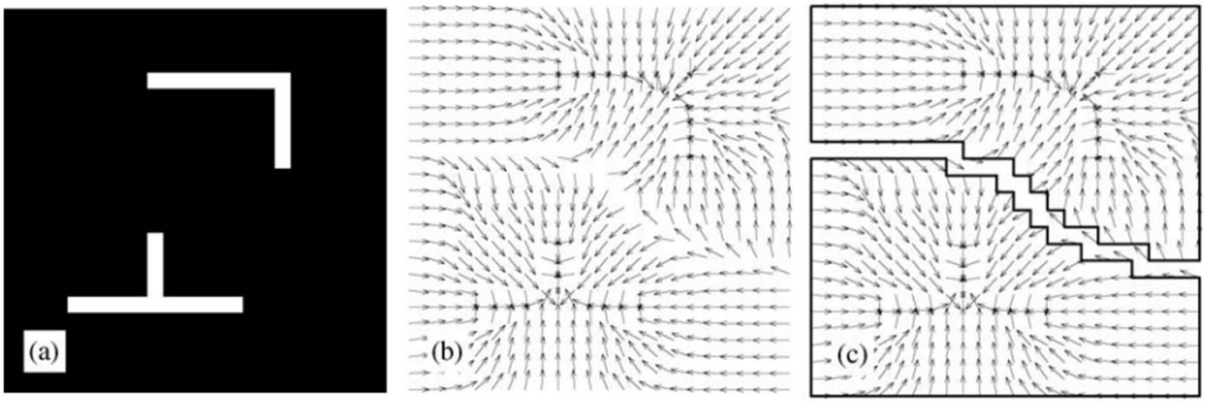

Figure 2.14 : (a) An example of a binary feature map, (b) the derived EPGVF vector field, and (c) the segmented force field enclosed by the two dark thick contours

Figure 2.16 indicates a deficiency of the CoD and FFS methods for contour initialization on a MR image, where they produce many active contour models due to the noise within the image.

Bing et al. [101] proposed a method based on an external energy force field and Dirichlet boundary conditions to automatically initialize parametric active models by solving Poisson's equation. They point out the relation between force field and energy field which implies that a force field is considered as the negative gradient of an energy field. Since the related fields such as GVF and VFC are not conservative, the scalar energy function does not exist and the external

energy field is approximated by solving Poisson's equation (see an example in figure 2.15). Then the initialization of the active model is identified as the contour line of the reconstructed external energy with lowest energy.

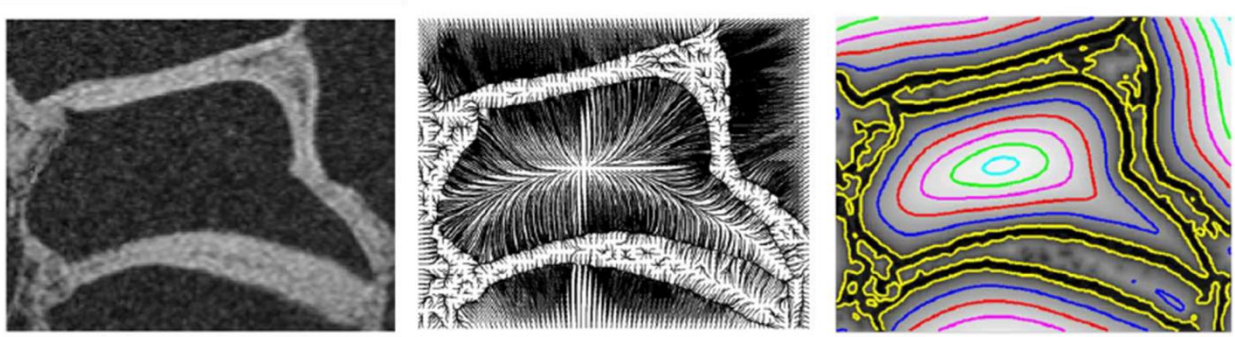

Figure 2.15 : Original image (left), computed VFC field (middle) and the estimated external energy of the VFC field (right)

Their method is limited to parametric active models, and doesn't preserve the boundaries of the objects within the image very well (figure 2.16).

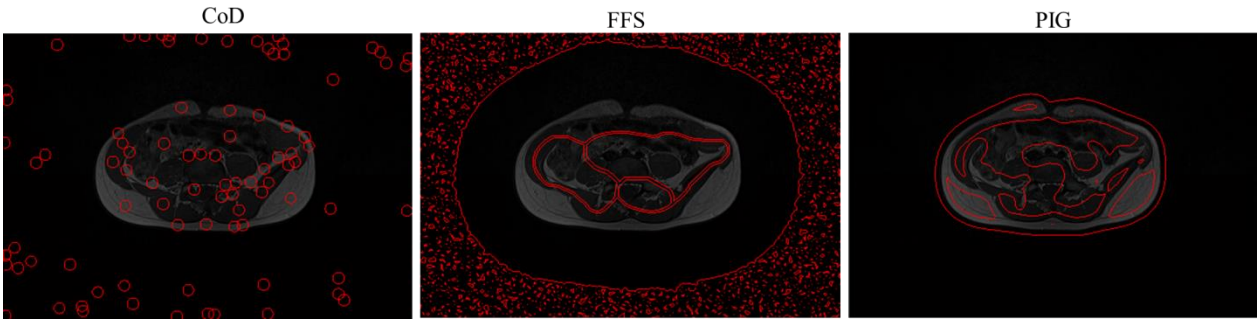

Figure 2.16 : Three different automatic initialization methods on a MR image; center of divergence (CoD) method (left), force field segmentation (FFS) method (middle), and Poisson inverse gradient (PIG) method (right)

So far we have reviewed segmentation methods which have been mainly proposed for MR images. Since our perspective is to segment multiple objects within the image, in the next section

we are going to review the literature that addresses the challenges of multi-object detection (aka MR image parsing).

2.4 Multi-Object Segmentation

Recently, there has been increasing interest in simultaneous multi-object segmentation. One of the popular applications for this approach is creating patient-specific models for simulation purposes. Many segmentation methods are capable of extracting one object at a time. Therefore, the process should be performed sequentially for multi-object segmentation. However such an approach may cause inefficiency and overlapping problems. Several attempts have been made to segment multiple adjacent objects at the same time and also solve the overlapping problem for medical images. A number of studies have led to the development of methods which incorporate higher-level knowledge into the segmentation. This knowledge, such as expert-defined rules, prior information, and shape models, can greatly improve the result of segmentation if they are applied properly. As an example, some researchers propose atlas-based approaches for multi-object segmentation. The atlases are generated based on information needed for segmentation. For example, some types of probabilistic atlases are generated from average intensity, tissue type and structural information [102]. The atlases are applied as a reference frame in the segmentation process, and the main idea is to determine a transformation to register one region of interest from the atlas to the region in the image that we are going to segment [103]. The result is mostly used as prior information for statistical pattern recognition and clustering approaches. For instance, atlases have been used with the fuzzy c-means method [104], the fuzzy connectedness segmentation [105], and the boundary identification approach [106]. Park et al. [107] present a probabilistic atlas and incorporate a Bayesian framework to segment low-contrast organs within CT images. Zhou and Bai [108] combine an abdominal atlas and a fuzzy-connectedness approach for segmenting abdominal organs. Okada et al. [109] construct hierarchical multi-organ statistical atlases from CT images for automatic segmentation. Wolz et al. [110] combine multi-atlas registration and patch-based registration to generate hierarchical atlases for segmenting abdominal organs from CT images. The major difficulty of atlas-based techniques is to find an accurate registration, especially in the case of complex structures, and this issue makes them more suitable in situations with stable structures over the population of study. In the general case,

atlas-based methods are problematic for segmentation of complicated structures with anatomical variability. Another groups suggest learning-based approach such as learning-based marginal space learning (MSL) models presented by Kohllberger et al. [111] for multi-organ detection in CT images. Also Lu et al. [112] combine the same approach with information theory to extract organs from CT scans.

Some other studies propose energy minimization approaches and using deformable models. Tsai et al. [113] present multiple objects which are implicitly separated by some signed distance functions and then a parametric model is derived by applying principal component analysis to these functions. The method represents a wide range of shape variability and can handle a large amount of noise. Yang et al. [114] present the incorporation of statistical neighbor prior information into level set formulation to segment multiple objects in MR data. Yan et al. [115] propose an energy function to provide competition between multiple deformable models using prior shape information. Li et al. [116] propose an optimal graph searching technique for segmenting multiple objects for MR images of ankle cartilage and tries to solve the overlapping problem. They also have extended their method for segmenting long vascular trees [117]. Costa et al. [118] introduce a fully automatic method for the segmentation of lower abdomen structures in CT images by enforcing statistical shape prior information into coupled deformable models. Shimizu et al. [119] introduce an energy minimization method for simultaneous extraction for 12 organs from CT images. They perform segmentation using multiple level sets and energy functional considering gray level uniformity, hierarchy and exclusiveness between organs. Yin et al. [120] have applied multi-object graph cuts for knee-joint bones segmentation and produce an accurate bone and cartilage segmentation result. Their graph segmentation requires preliminary localization prior to the optimal segmentation. A recent interesting method has been introduced by Gao et al. for multi-object segmentation of MR images in [121]. Although they have proposed a general-purpose image segmentation framework, it is not suitable in the context of an automatic scheme, because it is based on prior anatomical knowledge provided by the user. As can be seen many successful multi-object segmentation attempts were introduced for CT images. However in the case of MR images it is a more challenging task due to intensity inhomogeneity and low contrast across structures and also variability of anatomy appearance. Therefore, state-of-the-art in multi-object MR segmentation is very inferior to that of CT images.

Overall, the literature review presented here, has indicated some of the limitations of the current approaches in multi-object MR image segmentation. We have seen a number of edge-based and region-based segmentation methods (thresholding, clustering, region growing, watershed, etc.) which have been applied on MR images. Edge-based methods use intensity discontinuities as a criterion of region boundaries, but it is very challenging to aggregate the edge-based information to some coherent closed curves. On the other hand, region-based methods exploit intensity similarity and try to group pixels into coherent regions. The main challenge in these approaches is to find out the similarity criterion. Most of the above methods lack a mathematical optimization criterion to determine the convergence of the methods. This is where variational methods were introduced to devise a segmentation approaches that groups the regions based on optimizing some criterion such as minimizing some energy functional. Deformable models as a class of variational methods used for computing the segmentation, try to minimize the energy functional where its argument is a curve in the image. The curve is a boundary that we are looking for. The variational approaches have been started with ‘Snakes' and then improved greatly with time by introducing better representations, data terms, regularizers, etc. the main strategy for energy minimization approaches is to initialize the curve somehow and then propagate the curve to minimize the energy. The initialization is a crucial part which directly affects the segmentation performance.

Inspired by the ideas of discrete deformable models (meshes) and the capability of anisotropic adaptive mesh in mesh-based image representation, we are going to propose a new idea for automatic multi-object MR segmentation. We have a plan to employ anisotropic adaptive meshes for the initialization of active contour models. However, for incorporating mesh adaptation technique for our proposed framework, we need to construct a mesh for a given image in which elements of the mesh become aligned adequately with the boundaries of the objects in any directions. In this regard, we need to specify the metric tensors for image pixels in a proper manner to obtain the desired result. The current methods usually construct metrics using Hessian matrix of image pixels. Their computations lack an adequate alignment along inclined boundaries.

CHAPTER 3 RESEARCH OBJECTIVES

3.1 Problem Statement

Multi-object segmentation of MR images is a process of decomposing the images into several distinct sub-regions which represent different anatomical structures. This process can be conducted by classification of pixels in the image or by recognition of a boundary for each tissue class. Manual segmentation by radiologists is possible but it is tedious and time-consuming and reproducing the result is very difficult and uncertain. Therefore, automatic segmentation would be more desirable; however, there are still some problems to overcome for achieving a fully automatic approach which make it an active research area.

Deformable models are model-based techniques for determining boundaries of the objects using closed parametric curves which move based on internal and external forces. The major drawback of these models is that they are highly sensitive to model initialization and improper initialization may cause divergence and entrapment into local minima, and it may result in failure to detect true boundaries. The existing methods are limited in different ways which have been presented in the previous chapter. In this regard, we are going to propose incorporating anisotropic adaptive meshes to develop a new initialization method for deformable models to yield better segmentation results. In this thesis we implement and test our idea for parametric deformable models (active contours) but the idea can be used for initializing other types of deformable models as well.

On the other hand, anisotropic adaptive mesh strategies try to control mesh element characteristics so that they conform to image features and become usable for different applications in image processing. The edges are considered one of the most important features of the image identifying different objects in the image and mesh-based representation methods try to align mesh elements along these edges. The edge length of the mesh elements is controlled through the specification of a metric. As we discussed before, the existing anisotropic adaptive meshes which are used for mesh-based image representation are not completely suitable for our purpose. The main limitation of constructing metric tensors using these methods manifests itself in inadequate mesh element alignment to inclined edges of the image. Therefore, we need to

improve metric computation techniques for anisotropic mesh adaptation to provide a better representation according to our needs.

Consequently, by considering the above limitations, we set out our objectives in the following.

3.2 General and specific Objectives

As mentioned in the introduction, the general objective of this research study is to introduce an automatic method for multi-objects MR image segmentation by exploiting active contour models initialized using anisotropic adaptive meshes. In this way and also by considering the highlighted limitations of current methods, the specific objectives are as follows:

- To improve mesh anisotropy along inclined boundaries in mesh-based image representation
- To devise automatic deformable model initialization for multiple organ detection.
- To apply evolution process and integrate it in an organ segmentation process.
- To evaluate the initialization and final segmentation results.

3.3 General Methodology

In order to accomplish our objectives, several steps are specified as summarized in figure 3.1.

Adaptive Mesh Generation: At first we provide a triangular mesh for a given image and construct a metric tensor for each pixel, based on the directional second derivatives information. Then we generate an anisotropic mesh through mesh adaptation controlled by the prescribed metric. The output of this part is a mesh which is adequately adapted with region boundaries in the image.

Multi-objects Extraction: At this point, the elements of the adaptive mesh are partitioned in two sets: those that belong to the region interior, and those that belong to region boundary. Removing the interior elements creates several holes in the mesh, each one depicting the presence of an

object in that area. The holes are then extracted by identifying the elements around the holes. The outputs of this phase are several ordered sets of points for several objects in the image.

Segmentation Process: In this step, for each set of points we fit a B-Spline curve which provides an initialization for deformable model techniques. After automatic initialization of the model, the deformation process is applied to reach the final segmentation result.

Evaluation: In order to evaluate the effectiveness of the proposed approach, experimental validations using clinical MR data and comparison with current methods are conducted for different phases. Also the final segmentation result is compared to the ground truth result provided by experts.

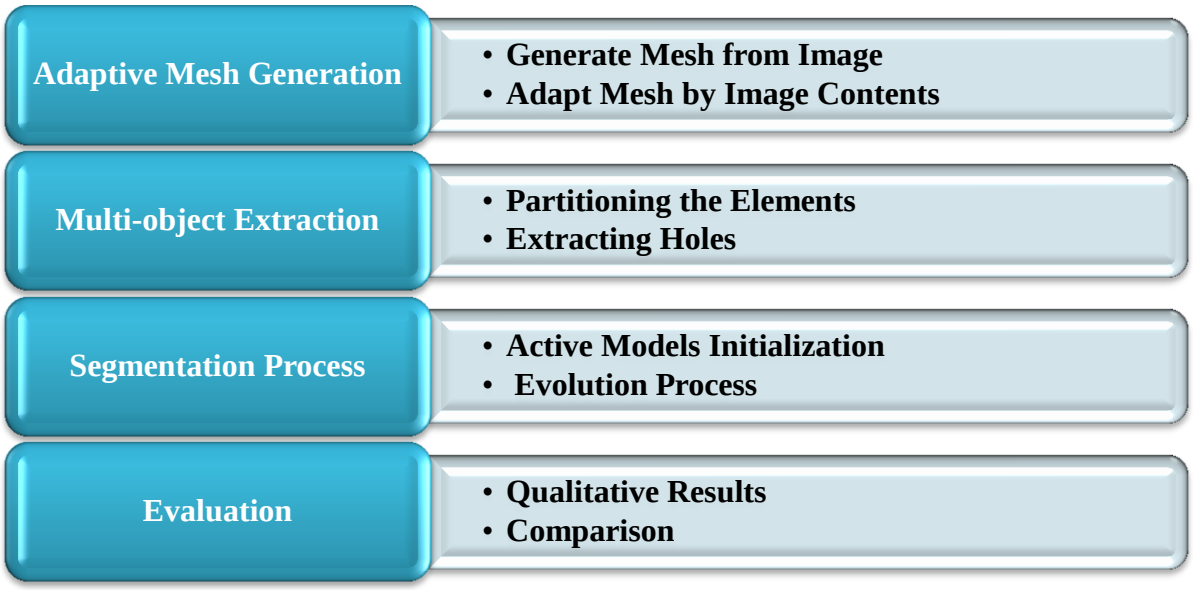

Figure 3.1 : Summary of general methodology presented in this thesis

CHAPTER 4 METHODOLOGY

In this chapter, we propose a novel framework for multi-object MR image segmentation by incorporating an adaptive mesh generation technique. The overview of the general methodology to achieve our goal was presented in the previous chapter and here we explain different steps of this methodology in details.

4.1 Adaptive Mesh Generation

The goal of this step is to provide an adaptive mesh for a given image that conforms well to the desired features within the image. In the scope of this project, desirable features of an image are considered as all the edges in the image that represent boundaries of different regions within the image. The OORT (Object-Oriented Remeshing Toolkit) software is used for adaptive mesh generation which needs two types of data as input; an initial mesh and a metric tensor field. OORT modifies the initial mesh based on the supplied metric tensor field to fit the mesh to the desired features.

The Initial Mesh is constructed based on MR image by considering each pixel in the image as a vertex in a triangular mesh as it is shown in the figure 4.1. Therefore, the vertices of the initial mesh support the gray-level intensity of image pixels as the solution field.

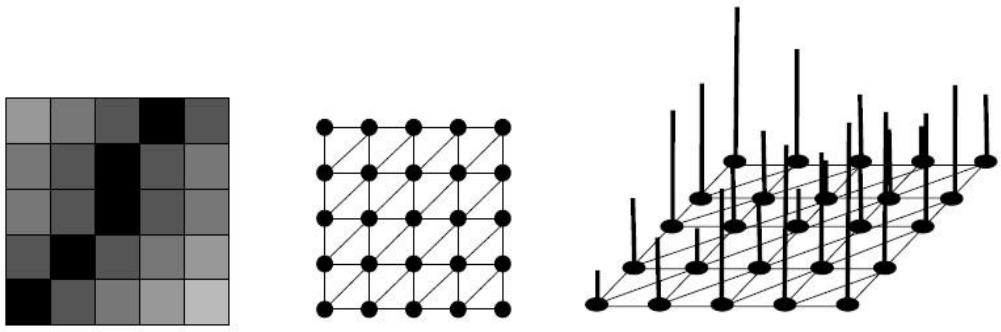

Figure 4.1: Initial triangular mesh corresponding to original image pixels

The Metric Tensor Field is constructed on the initial mesh using a Hessian matrix computed at pixels. The computation of the Hessian matrix in OORT is based on a geometric approximation

and it has been shown to be robust in numerical simulations for a range of application areas such as computation fluid dynamics. However, in the case of images, the Hessian computation does not work well for the pixels that belong to the edges in directions other than vertical and horizontal. In this sense, we propose a two-step process to overcome this limitation.

4.1.1 Metric Construction

The Hessian matrix is used to build a metric field and in the case of images, the Hessian matrix is constructed based on the gray-level intensity of the image pixels. In this regard, we apply a quadratic fitting approach for computing the Hessian matrix for all pixels except for the pixels that belong to the edge map, for which we compute a directional Hessian.

4.1.1.1 **Hessian Matrix Computation**

The Quadratic Fitting (QF) method fits a least-square quadratic polynomial at each pixel by considering a two-level neighborhood that surrounds the pixel. If we consider the quadratic function given in Eq. 4-1 and the basis functions for QF as in Eq.4-2,

$$F_h(x,y) = \sum_{i=1}^{6} a_i \varsigma_i(x,y) \tag{4-1}$$

$$\varsigma_i \in \{1, x, y, x^2, xy, y^2\} \tag{4-2}$$

the values of the second order derivatives are estimated at each pixel as in Eq. 4-3 to construct the Hessian matrix H in Eq.4-4.

$$\frac{\partial^2}{\partial x^2}\sum_{i=1}^{6} a_i \varsigma_i(x,y) = 2a_4 \tag{4-3}$$

$$\frac{\partial^2}{\partial x \partial y}\sum_{i=1}^{6} a_i \varsigma_i(x,y) = a_5$$

$$\frac{\partial^2}{\partial y^2}\sum_{i=1}^{6} a_i \varsigma_i(x,y) \;=\; 2a_6$$

$$H \;=\; \begin{bmatrix} \dfrac{\partial^2 F_h}{\partial x^2} & \dfrac{\partial^2 F_h}{\partial x \partial y} \\ \dfrac{\partial^2 F_h}{\partial x \partial y} & \dfrac{\partial^2 F_h}{\partial y^2} \end{bmatrix} = \begin{bmatrix} 2a_4 & a_5 \\ a_5 & 2a_6 \end{bmatrix} \tag{4-4}$$

4.1.1.2 **Directional Hessian Computation**

Consider a discrete intensity function $I = f(x,y)$ corresponding to a gray scale image as shown in figure 4.2. The reference coordinate system is shown by (x,y).

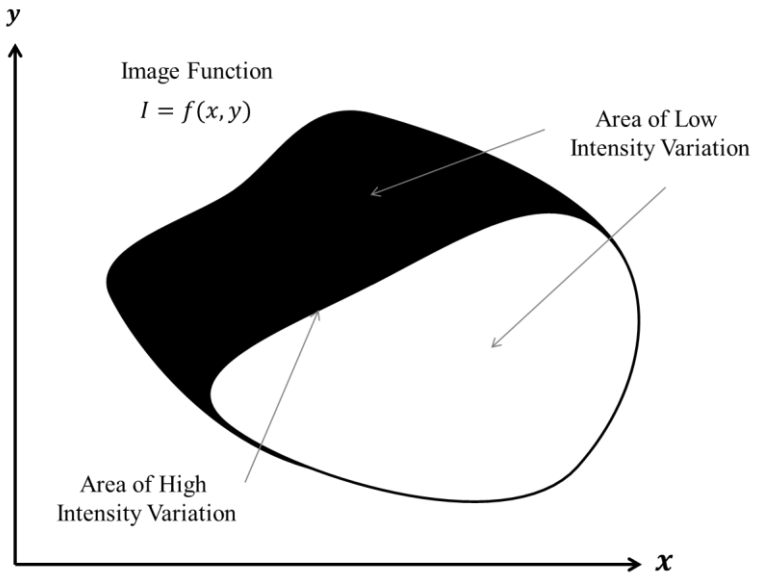

Figure 4.2 : Image I as a function of intensity values in a global coordinate system (x,y)

According to Geusebroek et al. [122], in two dimension images, image points that are on straight lines in different directions can be detected (i.e. line detection) by considering second order directional derivatives in the gradient direction. In practice, a measure of line contrast can be

obtained by the appropriate Gaussian weighted differentiation in the gradient direction as in Eq. 4-5.

$$f_{ww}^{\sigma} = G_{ww}(\sigma) * f(x, y) \quad (4\text{-}5)$$

Where f_{ww}^{σ} and $G_{ww}(\sigma)$ are second derivatives in the gradient direction of the image function and a Gaussian kernel respectively. The Gaussian standard deviation (σ) denotes the scale for detecting the line structure. They also concluded that, because of larger spatial extent along the line direction, compared to the direction perpendicular to the line, we need to use anisotropic Gaussian filtering with scales σ_v and σ_w along the longest and shortest axis. Therefore, differentiation along the line in direction θ when the filter is correctly aligned to the line direction is given by Eq. 4-6.

$$f_{ww}^{\sigma_v,\sigma_w,\theta} = G_{ww}(\sigma_v, \sigma_w, \theta) * f(x, y) \quad (4\text{-}6)$$

Where θ is a line direction, σ_v is a smoothing scale in line direction, and σ_w is a differentiation scale perpendicular to the line. Accordingly, in order to capture anisotropic features along inclined edges in a mesh-based image representation, we need to get elements aligned with the edge direction and compute a metric function by considering neighbors along the edges. In this regard, we need to use directional filtering in the edges directions.

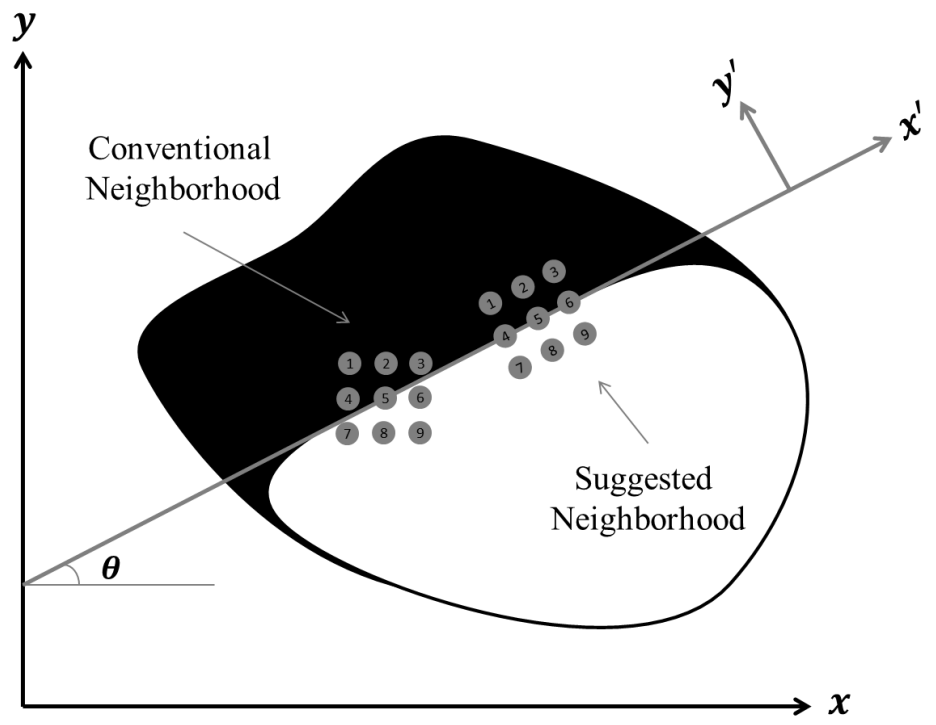

Figure 4.3 : Changing coordinate system and using proper neighborhood for Hessian computation

In terms of edge pixels, we compute the Hessian matrix on a rotated image. Rotating the image at edge pixels consists in changing the coordinate system along the edge direction and considering the neighbors along that direction for the Hessian matrix computation. Let's consider the local coordinate system denoted by (x', y') as shown in Figure 4.3, which corresponds to the edge direction θ. To determine the direction of the edges in the image, standard edge detection methods such as Canny which is the most widely used edge detector in image analysis can be used, followed by a gradient direction computation as follow:

$$\theta = \tan^{-1}\left(\frac{\partial f}{\partial y}\Big/\frac{\partial f}{\partial x}\right) \tag{4-7}$$

Then the local Hessian matrix, by considering differentiation on the discrete image with neighboring pixels labeled 1-9 along the edge direction in this coordinate system, is given by:

$$H(x', y') = \begin{bmatrix} \frac{\partial^2 f}{\partial x'^2} & \frac{\partial^2 f}{\partial x' \partial y'} \\ \frac{\partial^2 f}{\partial y' \partial x'} & \frac{\partial^2 f}{\partial y'^2} \end{bmatrix} \tag{4-8}$$

Then we have to use rotation transformation equations (Eq. 4-9) to transform the results from the local coordinate system back to the global coordinate system. Accordingly, the Hessian matrix in the global image system is obtained with Eq. 4-10 which will be used to construct the Hessian matrix for the image pixels that belong to the region boundaries.

$$R_\theta = \begin{bmatrix} \cos\theta & -\sin\theta \\ \sin\theta & \cos\theta \end{bmatrix} \tag{4-9}$$

$$H(x, y) = R'_\theta \, H(x', y') \, R_\theta \tag{4-10}$$

With respect to the direction of derivation (x', y'), approximations to the true image partial derivatives using conventional neighborhood are as follow:

$$\begin{aligned} f_{xx}^{\theta} = \; & \cos^2\theta \, (f[x+1, y] - 2f[x, y] + f[x-1, y]) \\ & + 2\sin\theta\cos\theta \, (f[x+1, y+1] + f[x-1, y-1] \\ & - f[x-1, y+1] - f[x+1, y-1]) \\ & + \sin^2\theta \, (f[x, y+1] - 2f[x, y] + f[x, y-1]) \end{aligned} \tag{4-11}$$

$$\begin{aligned} f_{xy}^{\theta} = \; & \sin\theta\cos\theta \, \{(f[x, y+1] - 2f[x, y] + f[x, y-1]) \\ & - (f[x+1, y] - 2f[x, y] + f[x-1, y])\} \\ & + (\cos^2\theta - \sin^2\theta)(f[x+1, y+1] + f[x-1, y-1] \\ & - f[x-1, y+1] - f[x+1, y-1]) \end{aligned} \tag{4-12}$$

$$f_{yy}^{\theta} = \sin^2\theta\,(f[x+1,y] - 2f[x,y] + f[x-1,y]) \qquad (4\text{-}13)$$
$$- 2\sin\theta\cos\theta\,(f[x+1,y+1] + f[x-1,y-1]$$
$$- f[x-1,y+1] - f[x+1,y-1])$$
$$+ \cos^2\theta\,(f[x,y+1] - 2f[x,y] + f[x,y-1])$$

The above equations are modified by picking neighbors along the edges. Using a 3x3 neighborhood size, we have a few possible pixel-wise situations in terms of edge angles $(0°, 18°, 26°, 45°, 63°, 72°, 90°)$ where some of them are presented in figure 4.5. All other direction angles are rounded to the nearest case. If edge is blurry which means image gradient changes gradually along the edge normal direction, we use a non-maximum suppression step of Canny's algorithm to find the local peaks of the neighborhood as it is shown in figure 4.4.

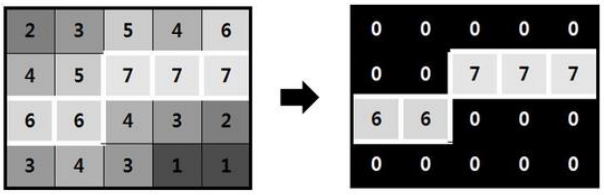

Figure 4.4 : Illustration of non-maximum suppression when the edge is blurry. The edge strengths are indicated both as colors and numbers.

Herein the computation of second derivatives for each pixel is performed in the edge direction and by considering neighbors along the edge numbered 1 to 9 as indicated in figure 4.5.

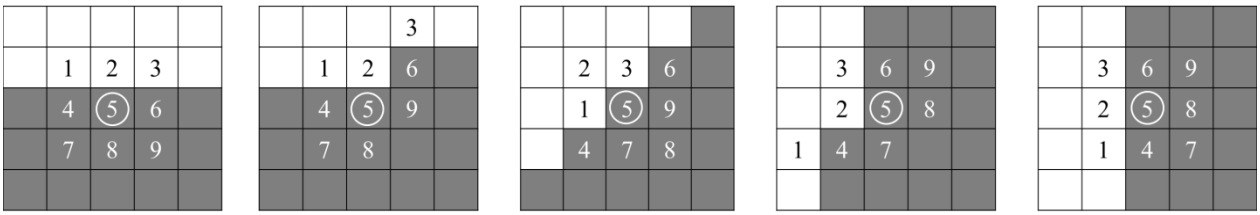

Figure 4.5 : Picking a proper neighborhood for the pixel in the center according to its edge direction

For example the partial second derivatives for an 18 degree edge are computed using Eq. 4-11 to 4-13 by substituting the image pixels according the new neighborhood set represented in figure 4.5. Therefore the modified equations are presented as follow:

$$f_{xx}^{18} = \cos^2 18\,(f[x+1,y-1] - 2f[x,y] + f[x-1,y]) + 2\sin 18 \cos 18\,(f[x+1,y] + f[x-1,y-1] - f[x-1,y+1] - f[x+1,y-2]) + \sin^2 18\,(f[x,y+1] - 2f[x,y] + f[x,y-1]) \quad (4\text{-}14)$$

$$f_{xy}^{18} = \sin 18 \cos 18\,\{(f[x,y+1] - 2f[x,y] + f[x,y-1]) - (f[x+1,y-1] - 2f[x,y] + f[x-1,y])\} + (\cos^2 18 - \sin^2 18)(f[x+1,y] + f[x-1,y-1] - f[x-1,y+1] - f[x+1,y-2]) \quad (4\text{-}15)$$

$$f_{yy}^{18} = \sin^2 18\,(f[x+1,y-1] - 2f[x,y] + f[x-1,y]) - 2\sin 18 \cos 18\,(f[x+1,y] + f[x-1,y-1] - f[x-1,y+1] - f[x+1,y-2]) + \cos^2 18\,(f[x,y+1] - 2f[x,y] + f[x,y-1]) \quad (4\text{-}16)$$

Likewise for the other six cases we provide corresponding equations to approximate the second derivatives which form the elements of the Hessian matrix. This would provide a better response of the second order directional derivatives in the gradient direction and the reason is because it involves proper neighbors along the edge direction.

So far we have computed the Hessian matrix for all pixels in the image. The next step is to construct a Riemannian metric field based on these Hessian matrices. As we mentioned in the previous chapter, the metric tensors need to be symmetric positive definite by construction. Since

the Hessian matrix is symmetric, it is diagonalizable and can be decomposed to eigenvectors and eigenvalues as in Eq. 4-17.

$$H = \mathcal{R}\Lambda^{t}\mathcal{R} = (\overrightarrow{e_1} \quad \overrightarrow{e_2}) \begin{pmatrix} \lambda_1 & 0 \\ 0 & \lambda_2 \end{pmatrix} \begin{pmatrix} \overrightarrow{e_1} \\ \overrightarrow{e_2} \end{pmatrix} \tag{4-17}$$

Where $\overrightarrow{e_1}$ and $\overrightarrow{e_2}$ are eigenvectors and λ_1 and λ_2 are eigenvalues such that:

$$\lambda_{1,2} = \frac{f_{xx} + f_{yy} \pm \sqrt{(f_{xx} - f_{yy})^2 + 4f_{xy}^2}}{2} \tag{4-18}$$

Where f_{xx} , f_{yy} and f_{xy} denote second order derivatives from the Hessian matrix. Then the eigenvalues are processed to be nonzero, positive definite such that when the metric tensor will be used to compute the distance, it will satisfy usual properties of a distance. Finally the processed eigenvalues λ_1' and λ_2' are multiplied by the eigenvectors to recompose the metric tensor $\mathcal{M}$ as in Eq. 4-19.

$$\mathcal{M} = (\overrightarrow{e_1} \quad \overrightarrow{e_2}) \begin{pmatrix} \lambda_1' & 0 \\ 0 & \lambda_2' \end{pmatrix} \begin{pmatrix} \overrightarrow{e_1} \\ \overrightarrow{e_2} \end{pmatrix} \tag{4-19}$$

The mesh adaptation process enforces the target size, stretching and orientation prescribed by this metric $\mathcal{M}$. Therefore, the edge length between two points a and b of the mesh domain in the Riemannian metric space is calculated by the following formula:

$$\ell_{\mathcal{M}}(a,b) = \int_0^1 \sqrt{{}^t\overrightarrow{ab}\,\mathcal{M}(a+tab)\overrightarrow{ab}}\ \mathrm{dt} \tag{4-20}$$

Where ab is parametrized by $t \in [0,1]$.

Figure 4.6 presents the adaptive meshes for three simple images with edges in different directions based on the proposed metric construction. It is shown that the proposed method is capable of handling all edge directions in the same manner and provides a smooth alignment even all around a circle with continuous change in orientation. This leads to an adaptation process that can: align adequately element edges with the edges present in an image, regardless of the edge direction,

improve the quality of the anisotropic meshing and reduce the number of mesh elements. A result of this anisotropic mesh adaptation technique on a MR image is presented in figure 4.7.

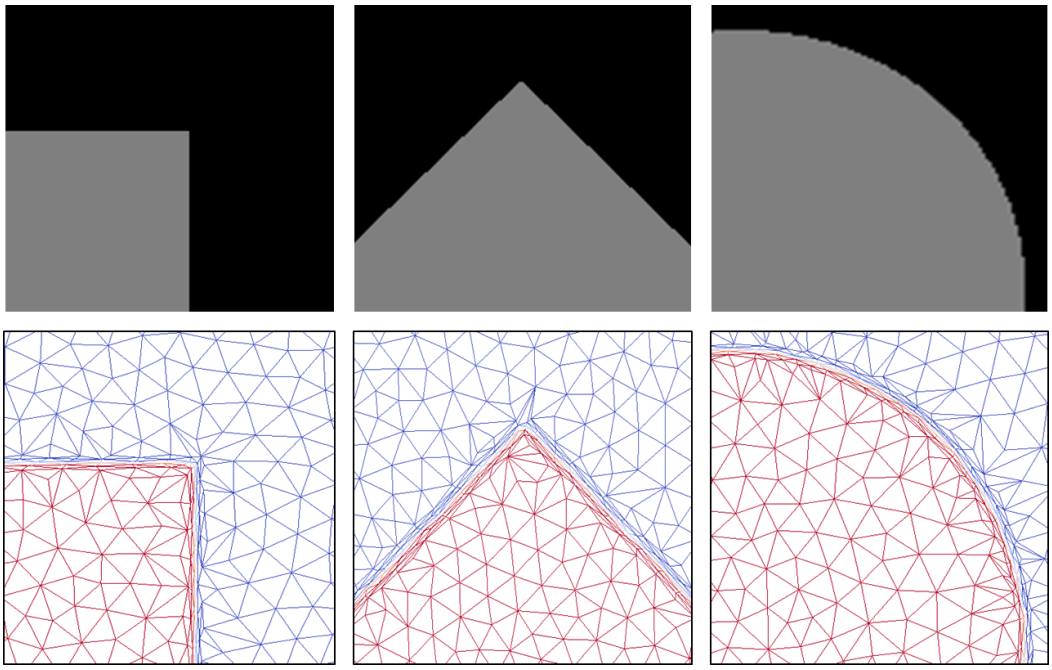

Figure 4.6 : Original images (top) and the corresponding adaptive meshes generated based on proposed metric construction (bottom)

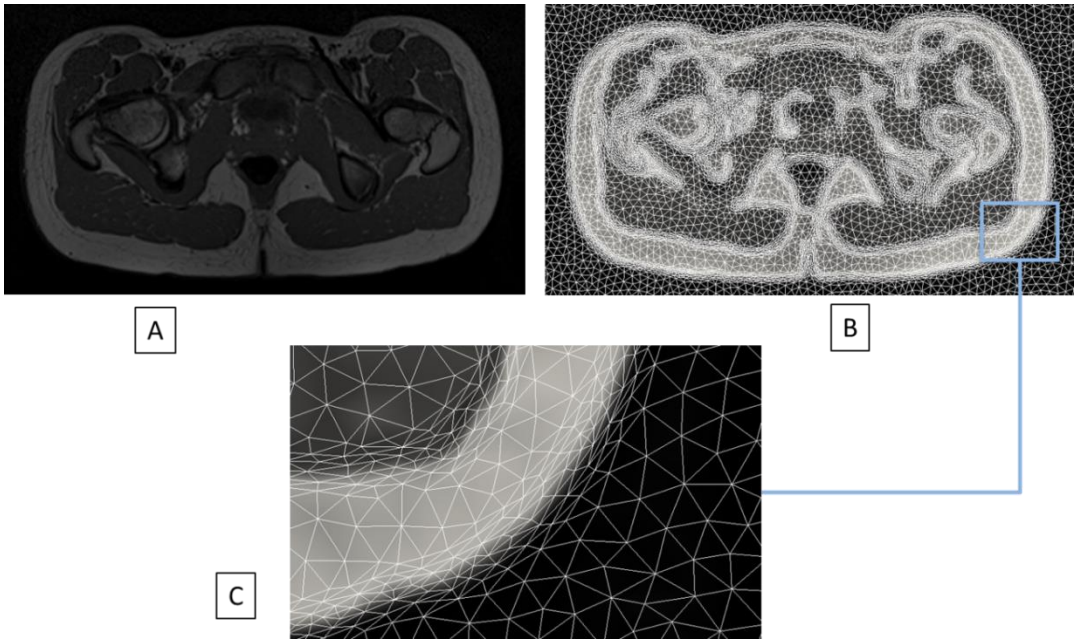

Figure 4.7 : (A) Original MR image; (B) Adaptive mesh of the same image; (C) Zoom on the highlighted part in (B)

4.2 Multi-Object Extraction

In this step, the goal is to utilize the adaptive mesh to identify different objects representing different organs in the image. The rationale behind our approach is to capture the image contents using a unit mesh generated in Riemannian space and discriminate the structures by analysing mesh characteristics in Euclidean Space. In this regard, first we partition the mesh elements and then extract the border lines to roughly identify different organs in the domain.

4.2.1 Partition of Elements

As a result of anisotropic mesh adaptation we have obtained a unit mesh in Riemannian space that contains fine and stretched elements near object boundaries and coarse and regular elements in the region inside the objects. Although all the elements sizes are equal in Riemannian length, they can be discriminated using Euclidean length. For this distinction we need to set a threshold on element size to categorize the mesh elements into boundary elements and region elements.

To find a suitable threshold we have analyzed the histogram of the mesh element size and found that, in general, the size histogram of all meshes are double-peaked or bimodal distributed like the one in figure 4.8. The bimodality is caused by two groups of elements which can be recognized pretty easily. Therefore, the threshold for separating boundary and region elements can be chosen in the distinctive valley between the two peaks. As it is shown in the figure, by removing the region elements from the mesh, several holes appear inside the mesh with each one depicting the presence of an organ in that area. This action also removes the background area of the image from the mesh. The results of two different thresholds selected in the range of the valley between the two peaks are also presented in the figure, where both of them are valid for roughly identifying organ structures.

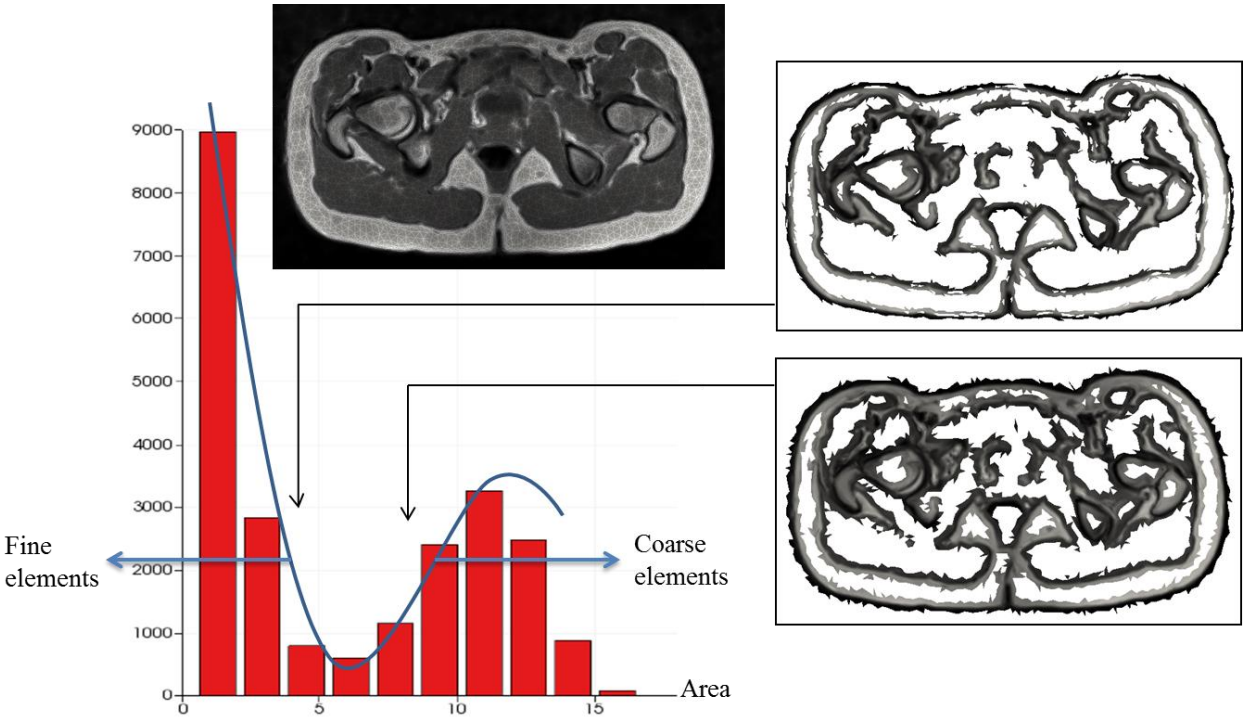

Figure 4.8 : Bimodal histogram of the element size for the mesh at the top and the result of selecting two different threshold values and removing the region elements from the mesh

4.2.2 Extracting Holes

Extracting the holes and identifying the elements around the holes yields a rough representation of the interfaces between the objects, which are very close to their true boundaries. We want to represent each hole as a set of vertices surrounding the hole and an important aspect we would like to consider is to have a set of ordered points to represent each hole. Therefore, after discriminating between the elements and removing the region elements, the next step is to extract the vertices around the holes which are shown in red color in figure 4.9-c. The Feature Edge filter from the Visualization Toolkit (VTK) has been used to extract these mesh edges on the borders and the example output is shown in figure 4.9-d.

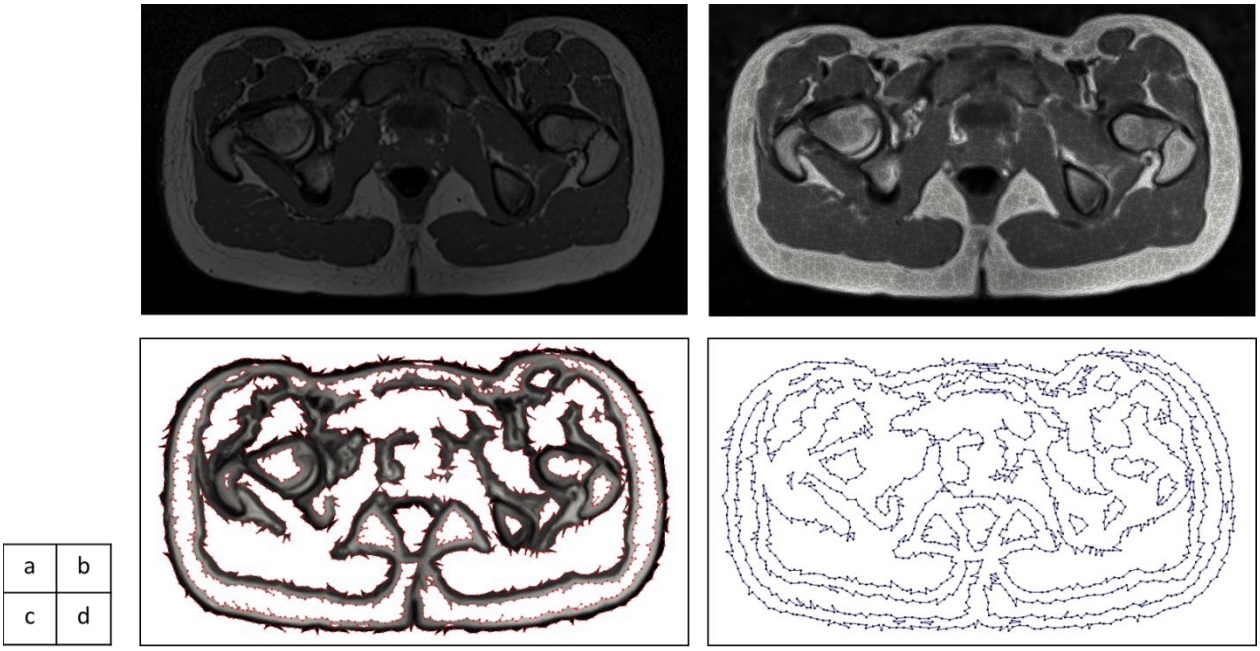

Figure 4.9 : (a) Original MR image (b) The corresponding adaptive mesh of the image (c) Extracting boundary elements (d) Identifying holes by locating boundary edges

Then we have to go through all these vertices to collect the different sets of vertices that belong to each hole. There is another filter in the VTK library named the Connectivity filter that can detect connected regions by selecting mesh edges that share common vertices and meet other connectivity criterion. Then by tracking these vertices sequentially, we can obtain the ordered set of vertices that belong to each hole. The Connectivity filter would be a solution to our need if the holes were completely separate, which is not a common situation in our cases. On the contrary, it is very probable to confront connected holes that share one or more vertices with each other as shown in figure 4.10. Therefore, we need to provide a more robust algorithm to handle all possible situations.

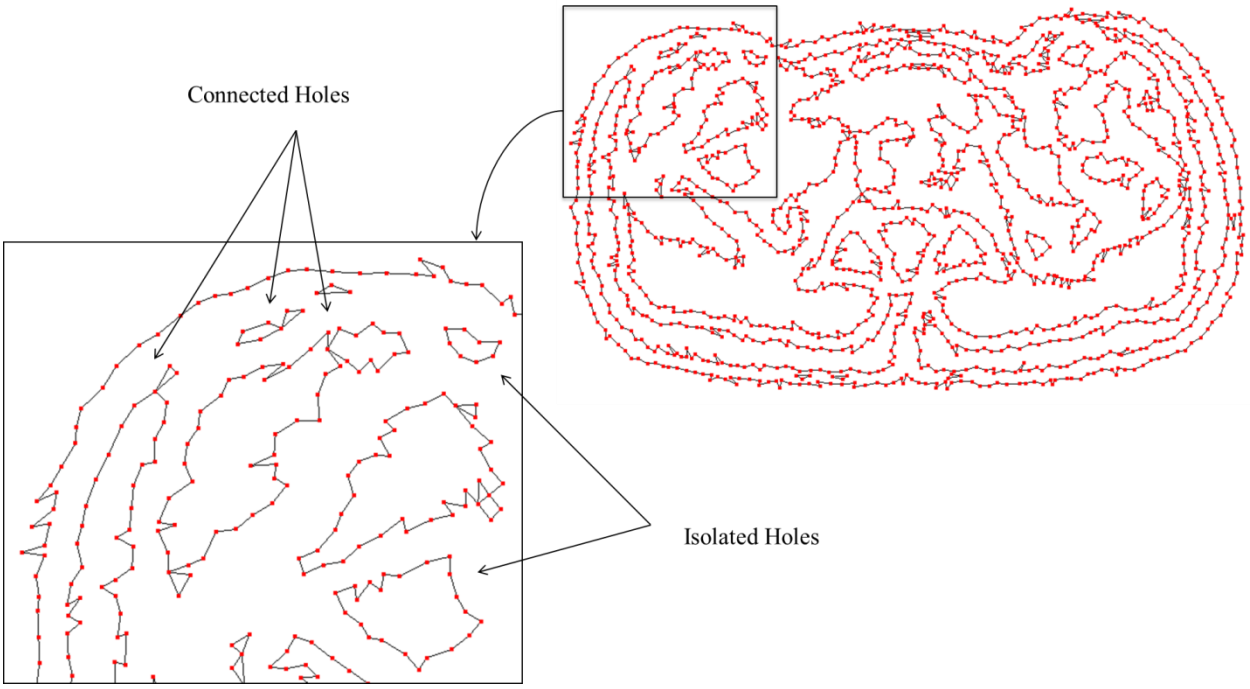

Figure 4.10 : Various status of produced holes after identifying boundary edges of the mesh

The following algorithm has been developed for extracting holes by tracking boundary edges, linking them together into loops which can handle all these situations and output several sets of points defining several holes. The algorithm explained in detail in the following.

Algorithm for Detecting the Holes

Input: List of feature edges extracted from the mesh
Output: Several Sequences of points defining several objects

Begin

- Create a *Vertex List*
- Mark all vertices as unvisited
- **While** (unvisited vertex exists)

{

- Create an empty output *Sequence*
- Pick an unvisited, single-degree from *head* vertices as a starting point *S*

- Mark as visited and add to the output *Sequence*
- **While** (the starting point *S* is not reached)
{
    - Follow the *tail* vertices
    - **If** (at this point exists more than one *tail* to follow)
    {
        - Compute angles considering each *tail* by $\mathbf{cos^{-1}}\left(\frac{\boldsymbol{current\ edge}\ .\ \boldsymbol{next\ edge}}{\|\boldsymbol{current\ edge}\|\|\boldsymbol{next\ edge}\|}\right)$
        - Pick tail vertex from the edge with biggest angle
    }
    - Mark the vertex as visited and add to the output *Sequence*
}
- Print out the output *Sequence*

}

End

The input of the algorithm is a set of mesh edges (line segment joining two vertices) where each edge consists of *head* vertex and *tail* vertex. The algorithm first creates a *vertex list* and for any *head* vertex, list out all the *tail* vertices for that, as it is shown in figure 4.11. The goal in this example is to separate these three connected holes and print out three sequences that contain ordered sets of vertices surrounding the holes.

Vertex list	
v0	v1
v1	v6
v2	v3
v3	v10
v4	v5 v8
v5	v0
v6	v7
v7	v17
v8	v9
v9	v4
v10	v11 v15
v11	v14
v12	v2
v13	v12
v14	v4
v15	v18
v16	v10
v17	v16
v18	v13

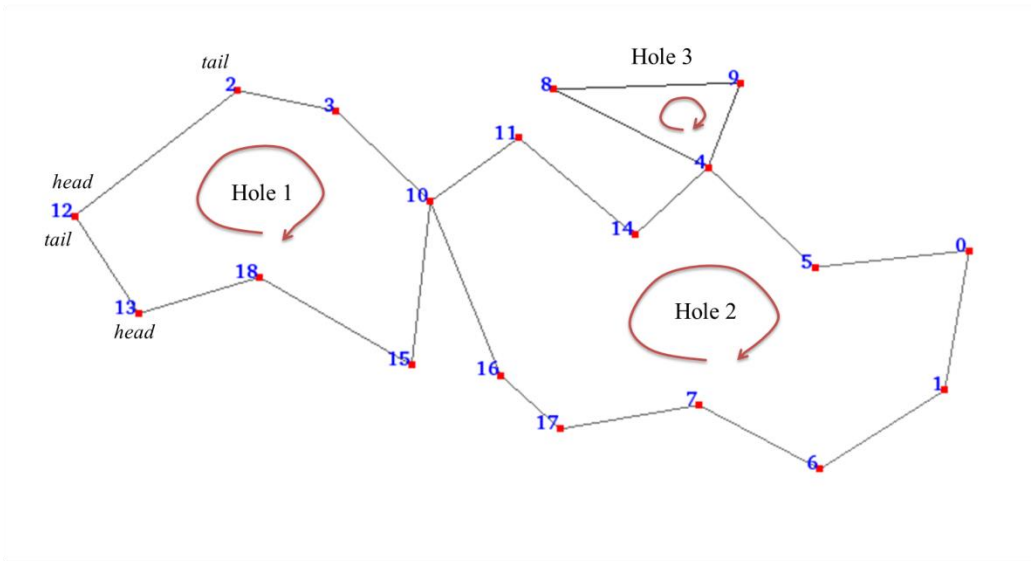

Figure 4.11 : An example of creating a vector list for a given mesh edge set

Each vertex has a unique *id*, position information, and a flag indicating if the vertex has been visited or not. All vertices are marked as unvisited and a loop begins by picking an unvisited, single-degree (a head vertex that has only one tail) vertex. The vertex is added to the output sequence and the loop continues by tracking subsequent tail vertices and adding to the sequence list until we reach back the starting point where we close the loop and print out the sequence. Figure 4.12 shows an example of this traversal procedure. This procedure is repeated until there are no unvisited vertices left in the vertex list. If in the cycle of any loop we encounter a vertex with more than one tail vertex, it means we have reached a point where two or more holes are connected to each other. To pick the correct subsequent vertex in a hole, we need to compute the angle between the current edge and the next candidate edge and pick the one with the biggest angle as shown in the example of figure 4.12. In this way, we can extract all the holes in only one pass through this list very efficiently and output several distinct sets. Each set contains an ordered list of vertices surrounding each hole.

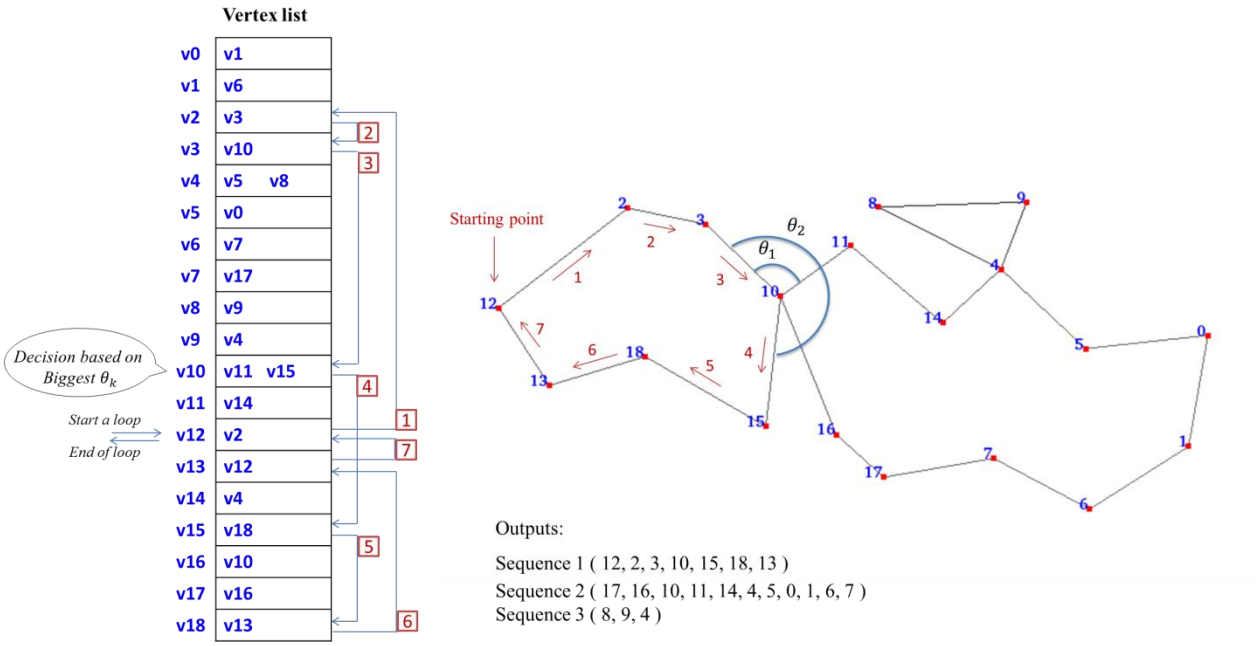

Figure 4.12 : The schematic description of the algorithm for extracting the holes with an example

4.3 Segmentation Process

After identifying admissible holes, the next step is to perform segmentation on the MR images. In this research we have focused on improving parametric deformable models also known as active contour models, but the idea can be extended to other types of edge-based deformable models as well.

For detecting multiple organs using an active contour model, we need multiple initial contours to deform based on external constraint forces and image forces toward boundaries of the organs. The initial contours can be provided by a user or by some other method, perhaps an automated one. In the following we use the extracted holes from the previous stage to automatically initialize multiple active contours and provide an approximation to the organs boundaries in the MR image, and then guide them using vector field convolution to find the actual boundaries.

4.3.1 Active Models Initialization

In general, an active contour is a controlled continuity spline guided by some external forces which tends to fall into the closest local energy minimum. Therefore, to obtain an accurate result, the contours need to be placed near the desired true boundary. As a potential solution, sets of points extracted for holes which are close enough to the true boundaries, are used to construct several splines for initiating the active contours segmentation approach. Each set of points is considered as a set of control points for fitting a B-spline curve. The *k*-order B-spline curve with $n+1$ control points $(P_0, P_1, \dots, P_n)$ and the knot vector $T = \{t_0, t_1, \dots, t_m\}$ is defined in Eq. 4-21 and its basis functions are defined in Eq. 4-22. An example of a B-spline curve fitted to some points and the corresponding basis functions are shown in figure 4.13.

$$C(t) = \sum_{i=0}^{n} N_{i,k}(t)\, P_i \tag{4-21}$$

$$N_{i,0}(t) = \begin{cases} 1 & if \quad t_i \le t < t_{i+1} \\ 0 & otherwise \end{cases} \tag{4-22}$$

$$N_{i,j}(t) = \frac{t - t_i}{t_{i+j} - t_i} N_{i,j-1}(t) + \frac{t_{i+j+1} - t}{t_{i+j+1} - t_{i+1}} N_{i+1,j-1}(t)$$

Where $j = 1,2, \dots, k$ and the degree of the basis functions is $k = m - n - 1$.

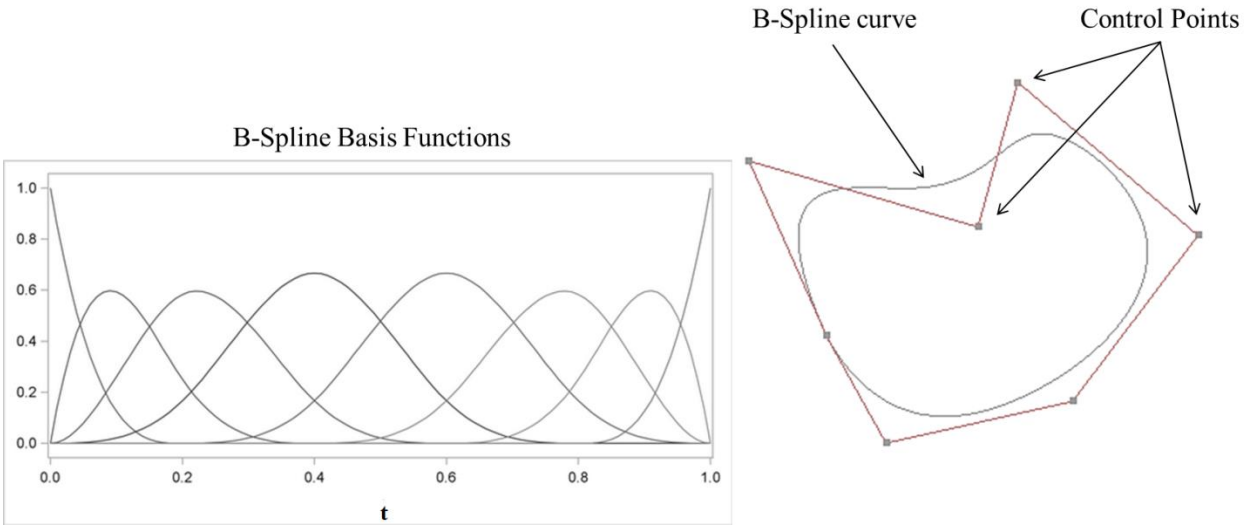

Figure 4.13 : Example of a B-spline curve with control points and corresponding basis functions

By repeating some of the knots and control points, the end points of the generated B-spline curve can coincide with each other and form a closed loop. In this regard, we follow these steps:

- Add a new control point $P_{n+1} = P_0$
- Provide a knot vector of $n + 1$ knots $\{t_0, t_1, \dots, t_n\}$
- Add $k + 2$ knots and wrap around the first $k + 2$ knots : $t_{n+1} = t_0$, $t_{n+2} = t_1$, $, \dots, t_{n+k+1} = t_k$, $t_{n+k+2} = t_{k+1}$

In the same way, we have constructed multiple closed B-spline curves for every set of points extracted for each organ in the MR images and initialize active models for performing segmentation. The result of generating several B-spline curves for sets of points extracted for a MR image is indicated in figure 4.14.

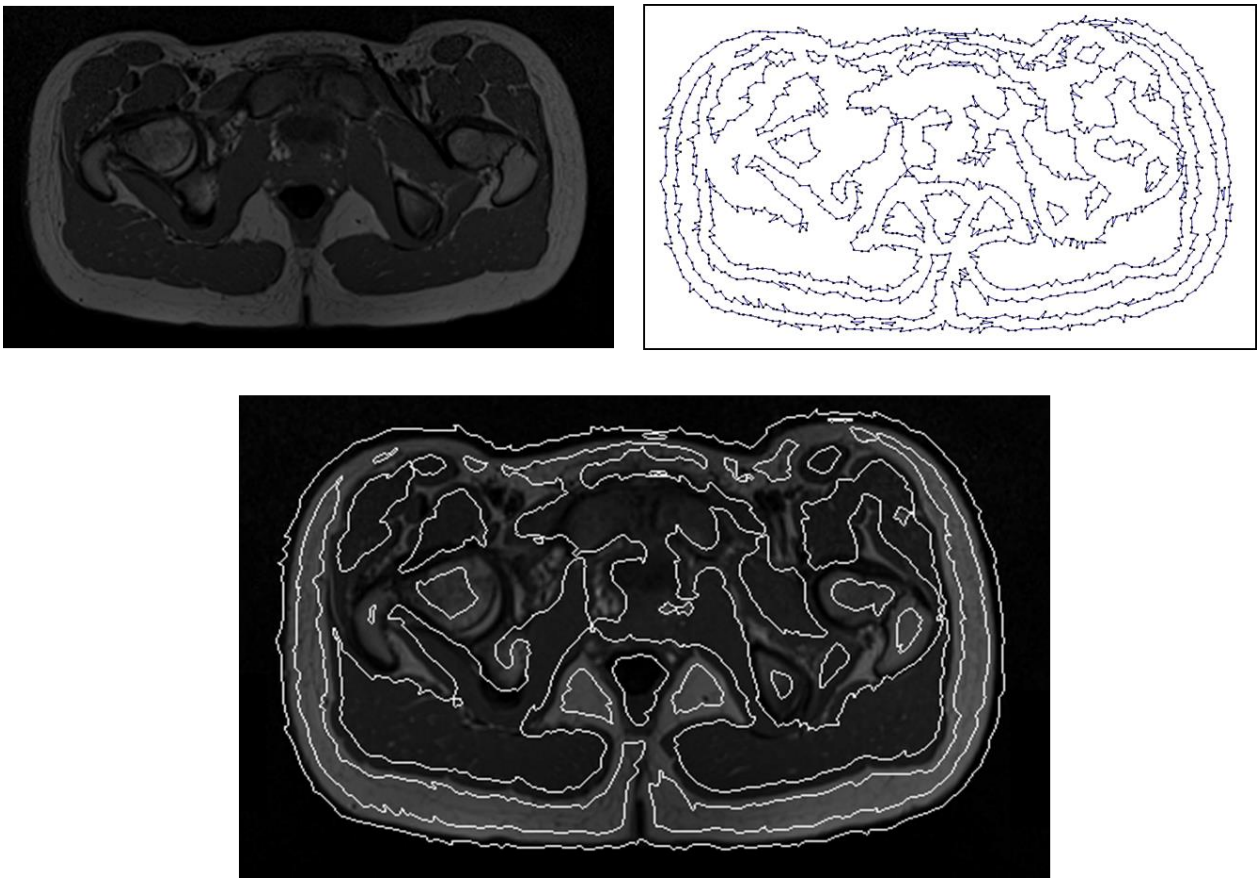

Figure 4.14 : Original MR image and its extracted sets of points (top) and overlay constructed curves onto the original image (bottom)

4.3.2 Evolution Process

So far we have provided several parametric active contours which are placed near the true boundaries of the organs in the MR images. At this stage, each active contour or curve $C(s) = [x(s)\ y(s)]^T$ is deformed to match the true boundary of each organ by minimizing the following energy functional:

$$E = \int_0^1 [\tfrac{1}{2}(\alpha|C'(s)|^2 + \beta|C''(s)|^2) + E_{ext}\big(C(s)\big)]\, ds \tag{4-23}$$

Where $C'(s)$ and $C''(s)$ are the first and second order derivatives of the curve with weighting parameters α and β. These parameters provide control over the internal energy functional responsible for controlling the smoothness constraints. E_{ext} is an external energy function that depends on the image properties for pushing the curve toward the boundary of the organ. The corresponding Euler-Lagrange equation for the minimum of the energy functional is as follow:

$$\alpha C''(s) - \beta C''''(s) + f_{ext}(C) = 0 \tag{4-24}$$

which means that the external force $f_{ext}(C)$ needs to be in balance with internal forces at the minimum. To solve the above equation, we convert it into a time dependent function $C(s,t)$ and use the following gradient descent equation which can be solved by considering the initial contour $C(s,0)$:

$$\frac{\partial C(s,t)}{\partial t} = \alpha C''(s,t) - \beta C''''(s,t) + f_{ext}(C(s,t)) \tag{4-25}$$

In the same way, all active contours evolve independently to minimize their energy functional and capture the true boundaries of the organs beneath them while keeping the smoothness of the resulting contours. The only problem that may arise during the evolution is the overlapping of adjacent contours because of a leakage problem when there is a weak edge separating two regions. In order to prevent such a situation, we chose an appropriate external energy field called Vector Field Convolution (VFC) presented by [123]. They have proposed a new class of static

external forces by convoluting $f_{edge}(x,y)$ as the edge map of the image with a vector field kernel $k(x,y) = [u_k(x,y), u_y(x,y)]$ shown in figure 4.15 as:

$$f_{vfc}(x,y) = f_{edge}(x,y) * k(x,y) \\ = [f_{edge}(x,y) * u_k(x,y)\ ,\ f_{edge}(x,y) * v_k(x,y)] \tag{4-26}$$

where the vector field k contains vectors with magnitude $m(x,y)$ pointing to the kernel origin.

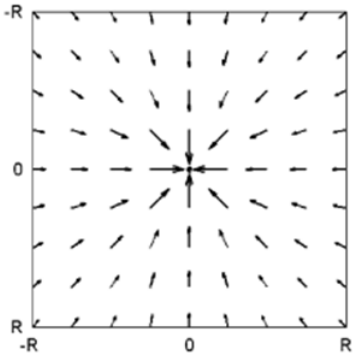

$$k(x,y) = m(x,y)n(x,y)$$
$$n(x,y) = [-x/r\ , -y/r]$$
$$r = \sqrt{x^2 + y^2}$$

$m(x,y)$ *magnitude of vector at* (x,y)
$n(x,y)$ *unit vector pointing to kernel origin*

Figure 4.15 : Example of vector field kernel with radius R and its related terms

They have alleviated the leakage problem by mixing the VFC field and gradient field of the edge map f_{edge} to increase the influence of the strong and weak edges and their capture range while the contribution of noise is reduced.

Hence by using f_{vfc} as the external energy function, we represent the family of evolving closed contours C_i that evolve simultaneously by solving the following gradient descent equation from the initial contours provided for each of them.

$$\frac{\partial C_i(s,t)}{\partial t} = \alpha C_i''(s,t) - \beta C_i''''(s,t) + f_{vfc}(C_i(s,t)) \tag{4-27}$$

Figure 4.16 indicates the final segmentation result of the above process and decomposition of the MR image into several segments representing different organs in the image without overlapping between adjacent regions.

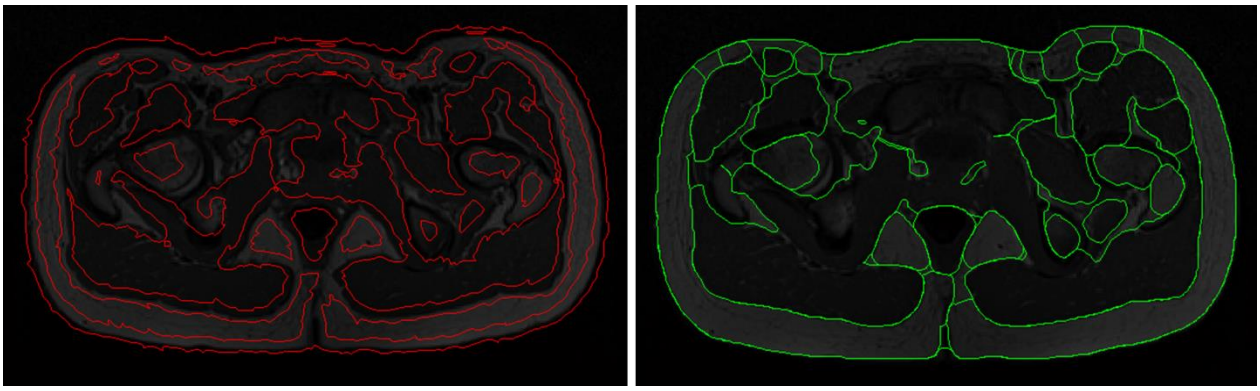

Figure 4.16 : Several closed active contours initialized on a MR image (left) final segmentation result for detecting the true boundary of the organs in the image (right)

4.4 Evaluation

In order to evaluate the performance of the proposed methodology, we have conducted several tests and comparisons for each step in the methodology. First for anisotropic mesh adaptation where we have proposed a new approach for metric computation, we generate adaptive meshes using the proposed metric and two other approaches and compare them qualitatively and quantitatively. Also we use these meshes to reconstruct the input images and measure the difference between these approximation and original images to indicate which approach provides a better representation of the given images.

Then for the active contour initialization step, we also picked two other automatic initialization methods and compared them to our results to demonstrate the effectiveness of our method in detecting multiple organs in MR image data and initializing multiple active contour models. After that, we allow the initial models provided by those three approaches to evolve and produce final segmentation results. The comparison is done in terms of number of models, number of iterations, and convergence time to verify the performance of the proposed method. In order to assess the accuracy of the segmentation results of our approach we also perform a comparison with ground truth data provided by experts for a series of MR images.

CHAPTER 5 RESULTS AND DISCUSSIONS

In this section we provide different experiments to evaluate the performance of the proposed methodology. These experiments include qualitative and quantitative evaluation for anisotropic mesh adaptation, active contour initialization, and the MR image segmentation along with comparison to previous methods and ground truth results.

5.1 Anisotropic Mesh Adaptation

As mentioned before, mesh-based image representation has been used in many applications such as numerical simulation in biomedical fields [94], finite element techniques in image processing [124, 125], image compression [126], etc. to meet the demands of these applications we need to reduce the number of elements and increase the anisotropy of the elements to be oriented in the direction of the image edges. In particular, for numerical simulation, which is our main concern, having fewer elements improves the computational efficiency of the simulations and the numerical solvers are highly sensitive to the element orientations especially when the features of the physical phenomena to capture are anisotropic. In the following, to demonstrate the ability of the proposed metric construction approach, we are going to present several adaptive meshes constructed by our proposed approach for different images and then the results will be compared to other approaches. In this regard, we have selected two different Hessian recovery techniques for images to construct metric tensors and generate anisotropic adaptive meshes for those images. One approach consists in computing a Hessian by spatial convolution filtering as presented by Farid and Simoncelli in [46] and the other to compute a Hessian by geometric approximation called the Quadratic Fitting (QF) method that fits a least-square quadratic polynomial for each pixel by considering two-level neighborhoods that surround the pixel [43]. Figure 5.1 shows three simple images containing single objects (square, diamond, and circle) and their corresponding adaptive meshes constructed using each approach, including our new method.

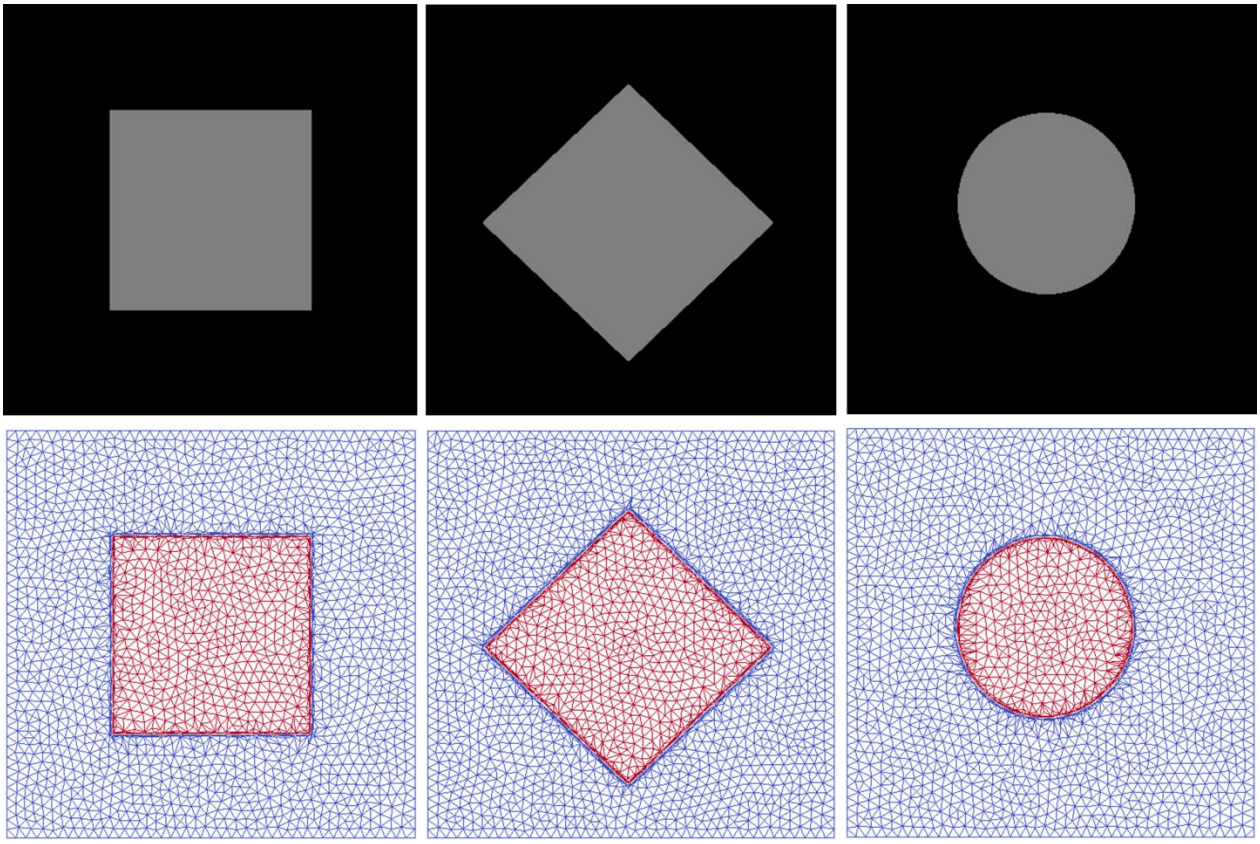

Figure 5.1 : Original images containing single objects for testing Hessian reconstruction algorithms and their corresponding anisotropic adaptive meshes

The comparison results are shown in figure 5.2 where results are illustrated with zoomed in portions on edge parts, to indicate the details of adaptation at the edges. The first column in figure 5.2 shows the results using Farid and Simoncelli's technique for derivative computation, which clearly can provide adequate alignment only in orthogonal directions and fails in all other directions. The second column of figure 5.2 illustrates the resulting meshes using the QF technique that provides better alignment to the edges in all directions but the elements are not stretched enough along the edges in directions other than those aligned with the coordinate axes, where this difference is clearly showed in figure 5.3. The third column in figure 5.2 represents the result of applying our approach, which provides a smooth alignment even all around a circle with continuous change in orientation. Figure 5.4 indicates the skewness of the elements on the adapted mesh obtained by the proposed method along the orthogonal and non-orthogonal edges

in the image which confirms its ability to handle orthogonal and non-orthogonal edge directions in the same manner.

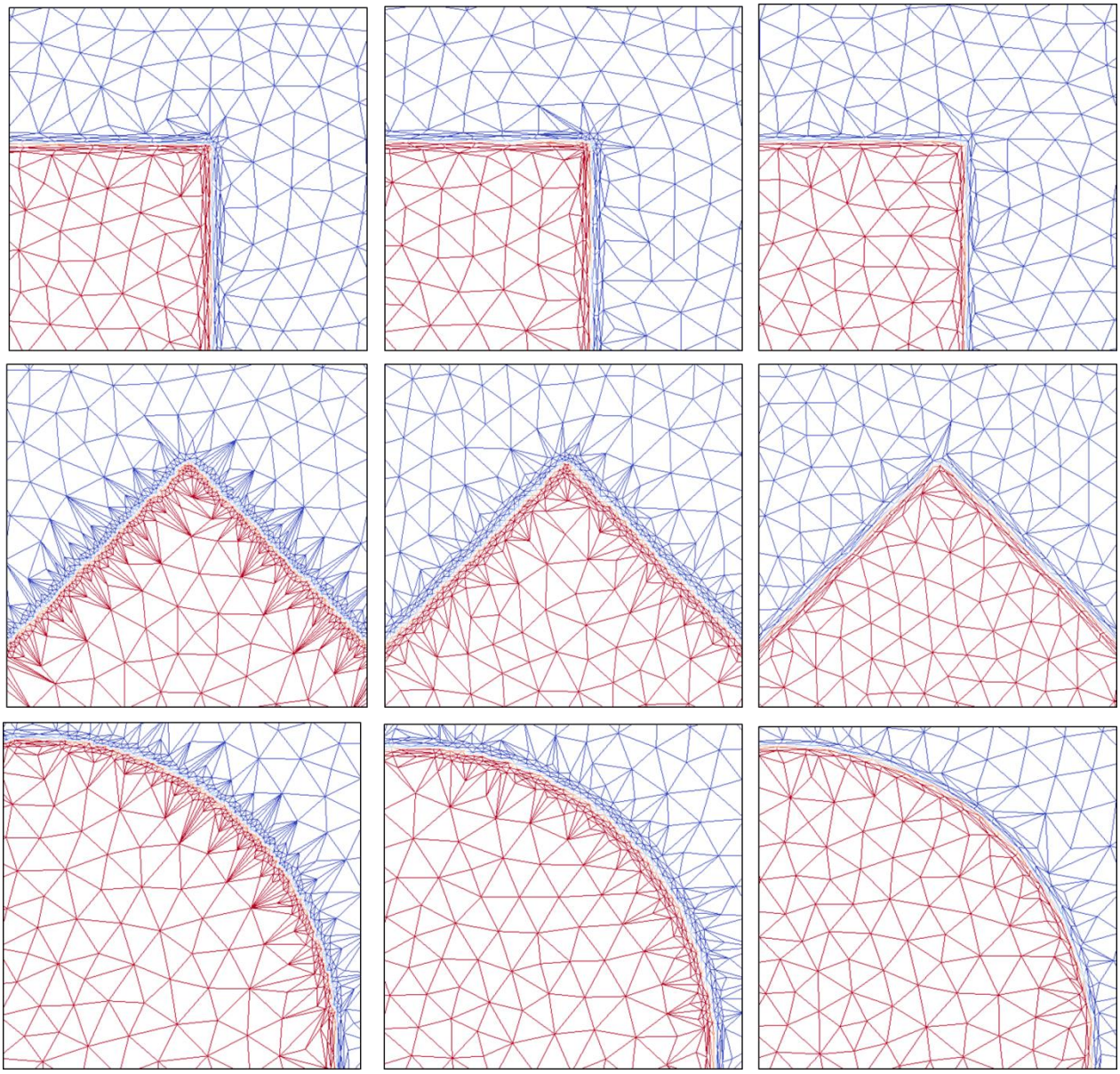

Figure 5.2 : Zoom-in on resulting adapted meshes constructed based on three methods; the approach by Farid & Simoncelli (left), the QF approach (middle), and our proposed approach (right)

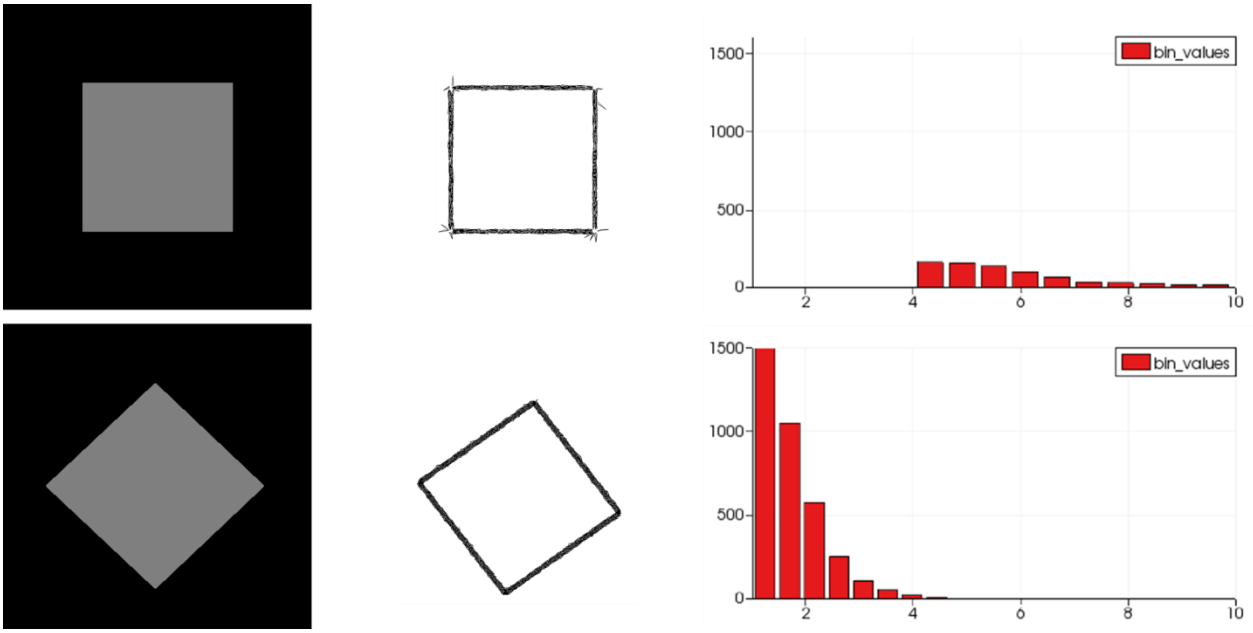

Figure 5.3 : Element skewness on the adapted mesh obtained by the QF approach for axis-aligned and non-axis-aligned edge directions

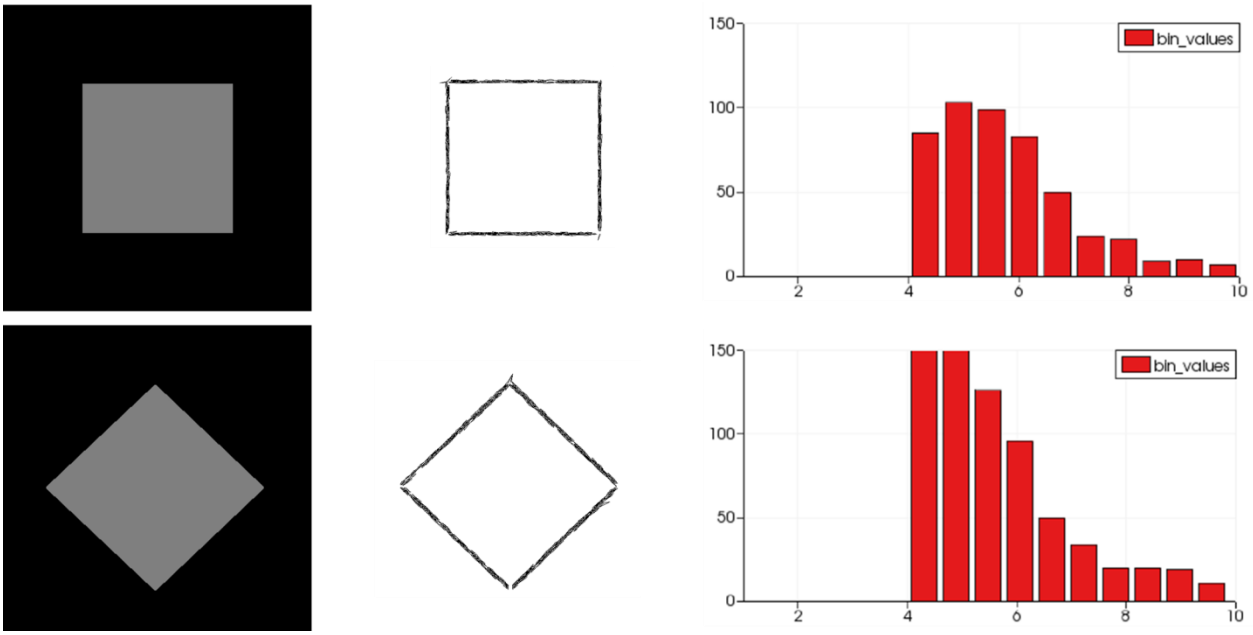

Figure 5.4 : Element skewness on the adapted mesh obtained by our proposed approach for axis-aligned and non-axis-aligned edge directions

In terms of the number of elements, our proposed method also has better performance than the two other approaches and, as can be seen in Table 5.1, produces adaptive meshes with fewer elements, thereby demonstrating the improvement of the adaptation process.

Table 5-1 : Number of elements in adaptive meshes constructed by the three approaches

	Farid & Simoncelli	*Quadratic Fitting*	*Proposed method*
Square	4584	4428	4148
Diamond	8682	7300	4524
Circle	6354	5496	4160

Moreover, in order to show the improvement of the anisotropy and skewness of the elements along the image edges, figure 5.5 presents histograms of element anisotropy for the Circle example provided by the three approaches.

In this regard, we chose the three adaptive meshes generated by the three approaches for the Circle example and extracted the elements with aspect ratio ≥ 2. The corresponding histograms present the number of the elements with an aspect ratio ≥ 2. The results indicate that the anisotropic elements obtained by the two other methods are not located on the image edges and they do not follow the edges orientation. Then again, the result of the proposed method shows the presence of more anisotropic elements along the edge locations and in the corresponding orientations.

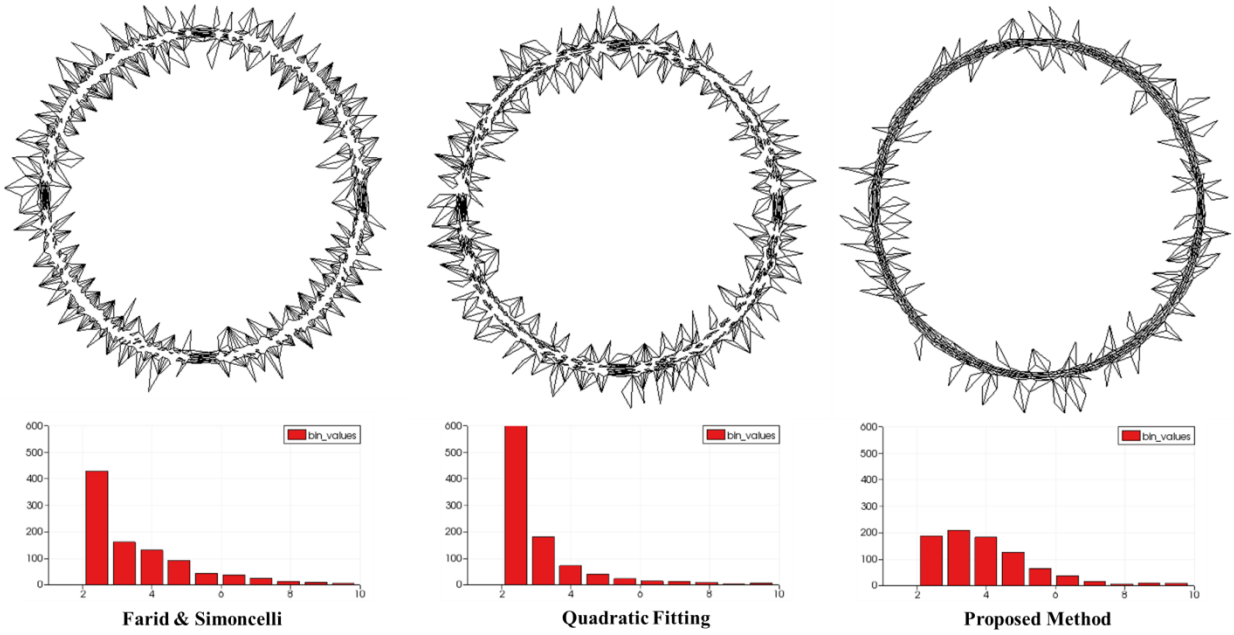

Figure 5.5 : Extracting the anisotropic elements (aspect ratio ≥ 2) from resulting meshes for the three approaches for the Circle example and their corresponding histograms

In order to validate the proposed algorithm for real applications, we have used MRI data of human trunk. So, we have applied the proposed method on a series of MR images of human trunk and generated adaptive meshes. We have performed the same comparison as above, with the two other methods and the results are shown in figure 5.6 and 5.7.

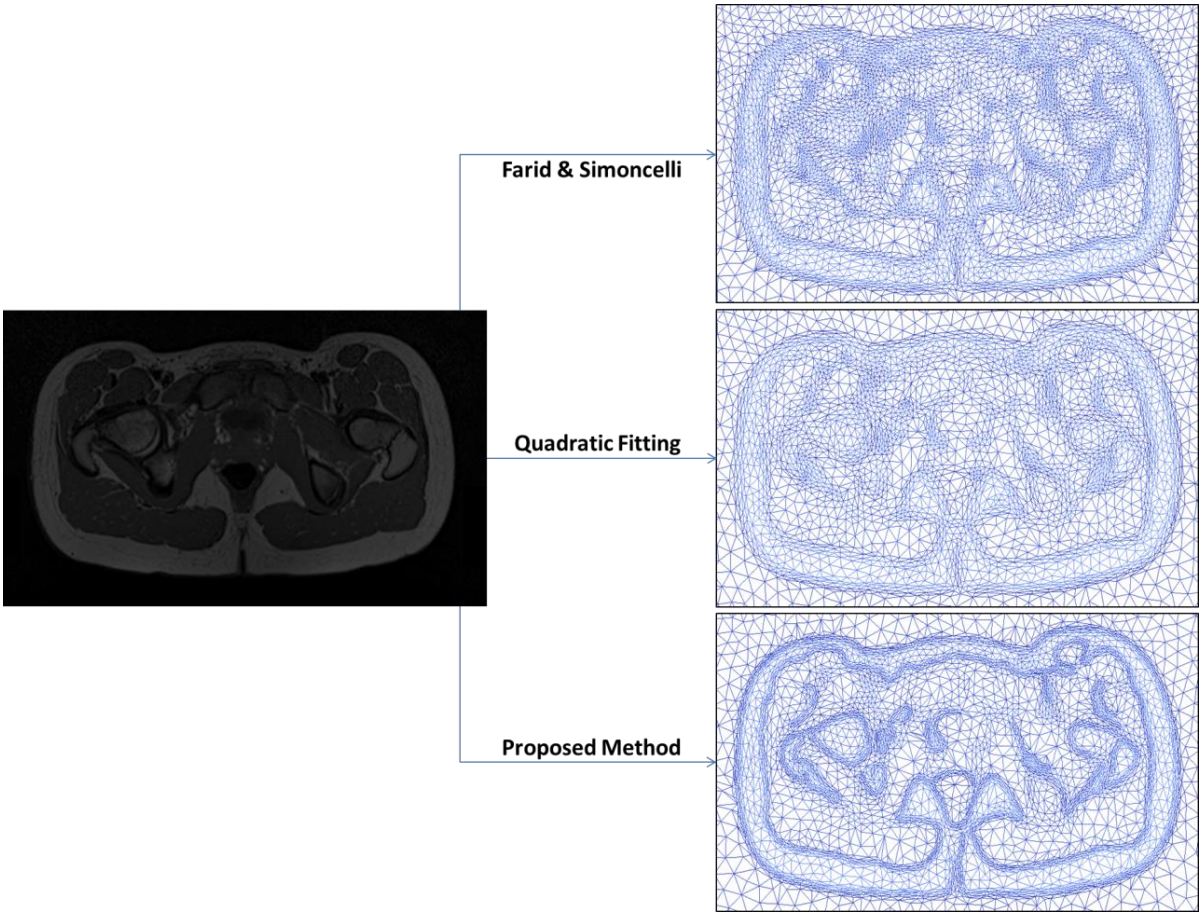

Figure 5.6 : Anisotropic adaptive meshes constructed based on the three mentioned approaches for the given MR image of the human trunk

As clearly observable in figure 5.7, the proposed approach generates elongated elements in all directions and provides a detailed map of anisotropic features of the image in terms of anisotropic mesh elements while the other two methods were able to capture the detailed features mostly in the orthogonal directions.

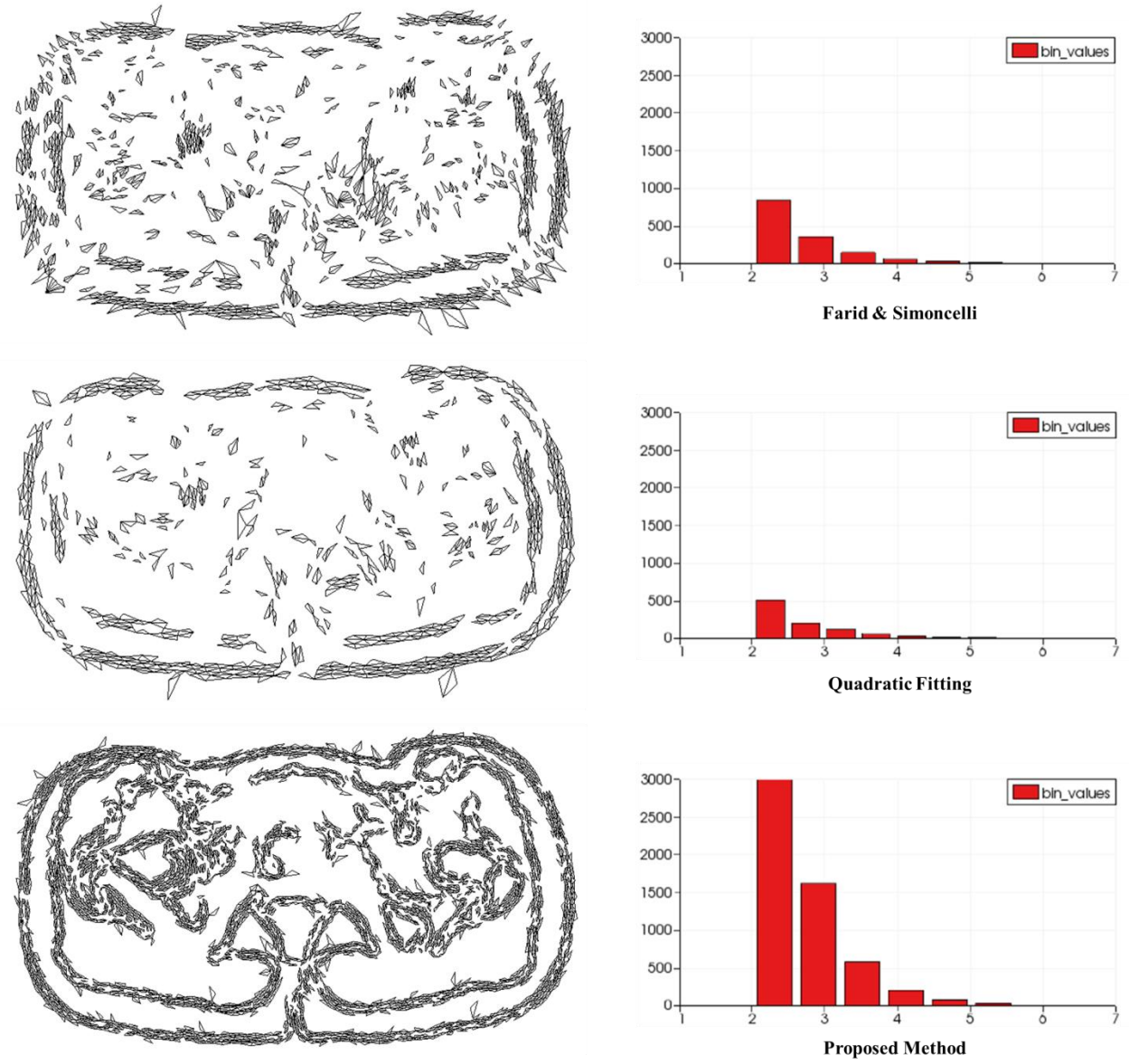

Figure 5.7 : Extracting anisotropic elements (aspect ratio ≥ 2) from resulting meshes for the three approaches for a MR image and their corresponding histograms

Furthermore, to verify the proposed adaptation process, we have considered the verification of the reconstructed solution [21]. In this regard, we have used the gray-level values of the image as a solution and tried to reconstruct the image by interpolating data from the adaptive mesh, and then computed the error of image reconstruction. To demonstrate the relative improvement in mesh-based representation of those images, we have compared image reconstruction results of isotropic and anisotropic adaptation techniques. Figure 5.8 presents three adaptive meshes for an

MR image of a human trunk generated based on isotropic, QF, and the proposed adaptation process. The comparison result for image reconstruction over series of adaptive meshes of different sizes is shown in figure 5.9. The reconstruction error is obtained as a Mean Square Error (MSE) between pixel intensity of the original image and the reconstructed image, and the mesh size is characterized by length *h* of the mesh which is computed as follows:

$$h = (A_\Omega / N)^{1/2} \tag{5-1}$$

where A_Ω denotes the area of the image domain Ω and N is the number of elements.

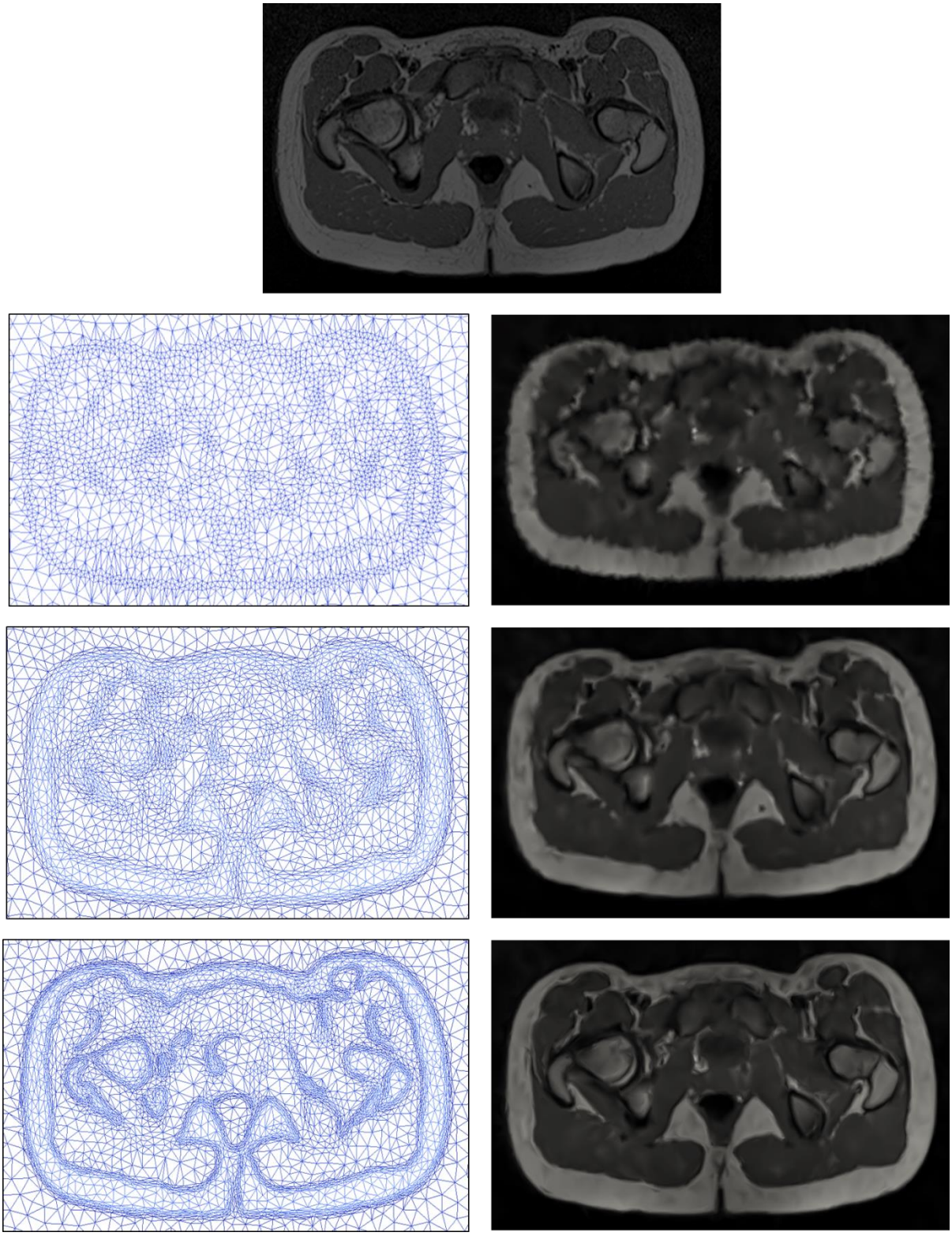

Figure 5.8 : Original MR image at the top and three mesh-based representations (isotropic, QF, proposed method) and their corresponding reconstructed images

Figure 5.9 presents a plot of the log value of the reconstruction error of the image as a function of the log value of h. The top curve corresponds to adapted isotropic meshes, the middle curve to adapted anisotropic meshes based on the QF method and the bottom curve to adapted anisotropic meshes by the proposed method.

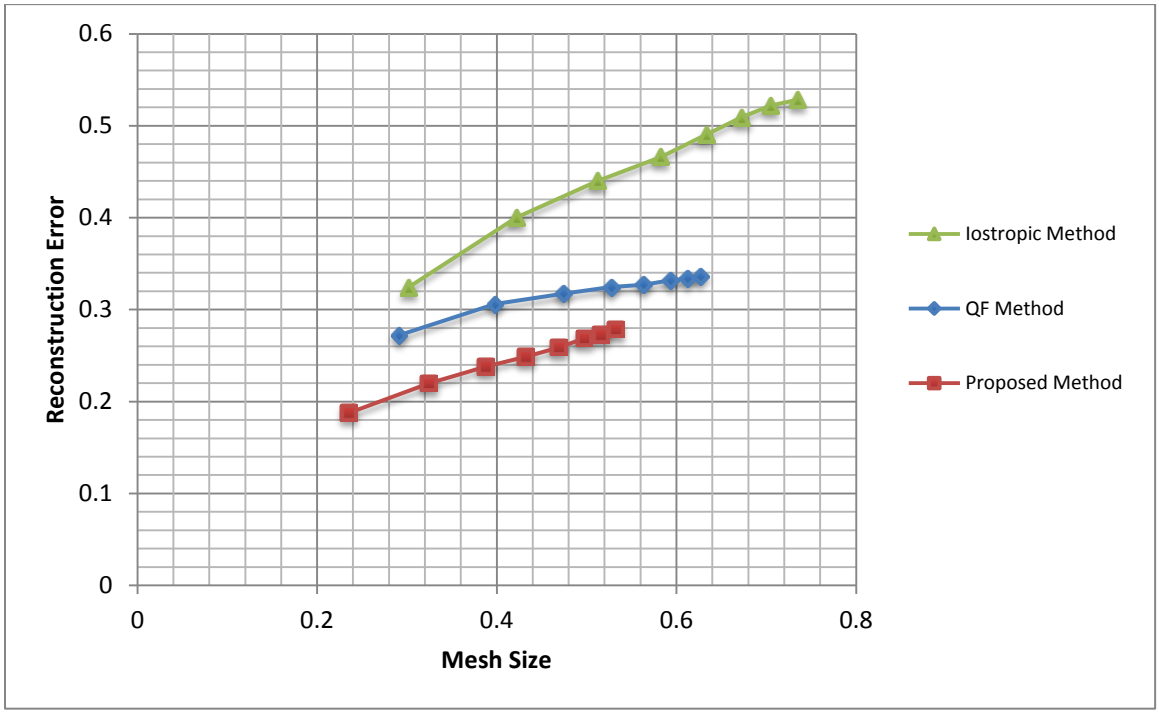

Figure 5.9 : Image reconstruction error over different types of adaptive meshes with different sizes

As expected, the error decreases with refinement for all types of the meshes, but there is an improvement in precision for an equivalent number of elements for the proposed anisotropic adapted meshes. Furthermore, in order to verify the correctness of the results, we have applied the QF method and the proposed method on a series of MR images containing 28 slices of human trunk and summarized the results in figure 5.10. In this bar graph, each bar length represents the average reconstruction error of all images, computed for different mesh sizes and each error bar represents the minimum and maximum error computed among all those images. This shows that the proposed method, which generates more anisotropic meshes by aligning elements with the boundaries of the regions in every direction, not only can provide an adaptive mesh with fewer

elements, but also can improve the interpolation results for image reconstruction. These aspects make the proposed method a better fit for mesh-based image representation for simulation purposes, or any applications that incorporates finite element techniques for image analysis.

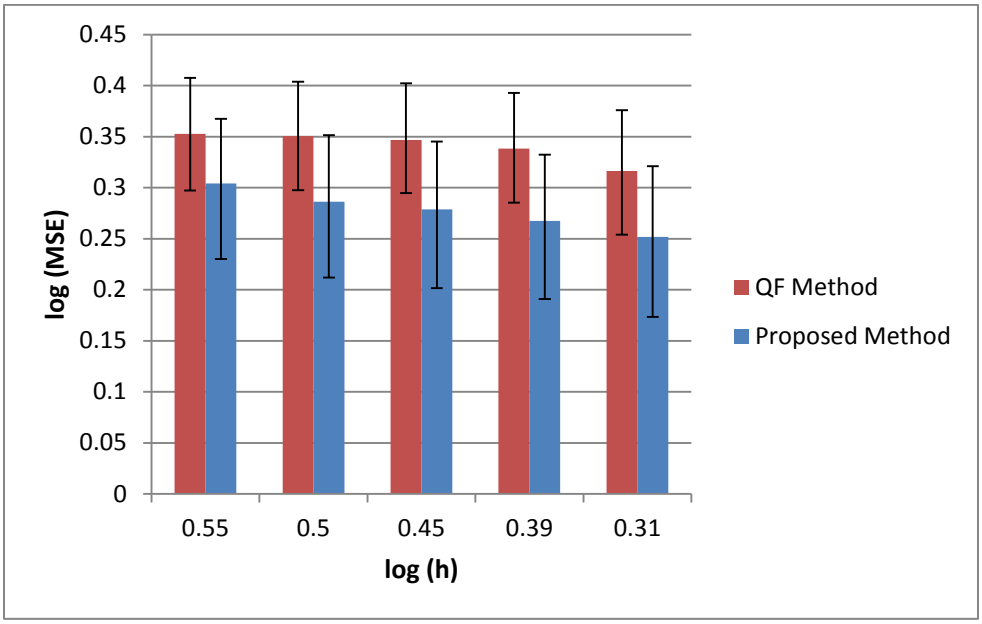

Figure 5.10 : Comparison between QF method and proposed method on a series of MR images

So far, we have demonstrated the capability of the proposed anisotropic mesh adaptation method for image representation. In the next part we discuss exploiting this mesh-based representation for active contour initialization.

5.2 Active Contour Initialization

As described in the methodology part, after partitioning the mesh elements and detecting the holes, several distinct closed curves are constructed using a B-spline parametric representation. These are used as active contour initializations for segmenting different organs in MR images. We have applied this procedure for various series of axial MR images and the results are reported in the following. Since quantitative assessment is generally difficult for medical images and there is no formal criterion to measure initialization results, we have provided qualitative results and

comparison with other studies. Figure 5.11 and 5.12 present several MR images from human arm and trunk sections and their corresponding multiple active contour initializations, constructed using our proposed method.

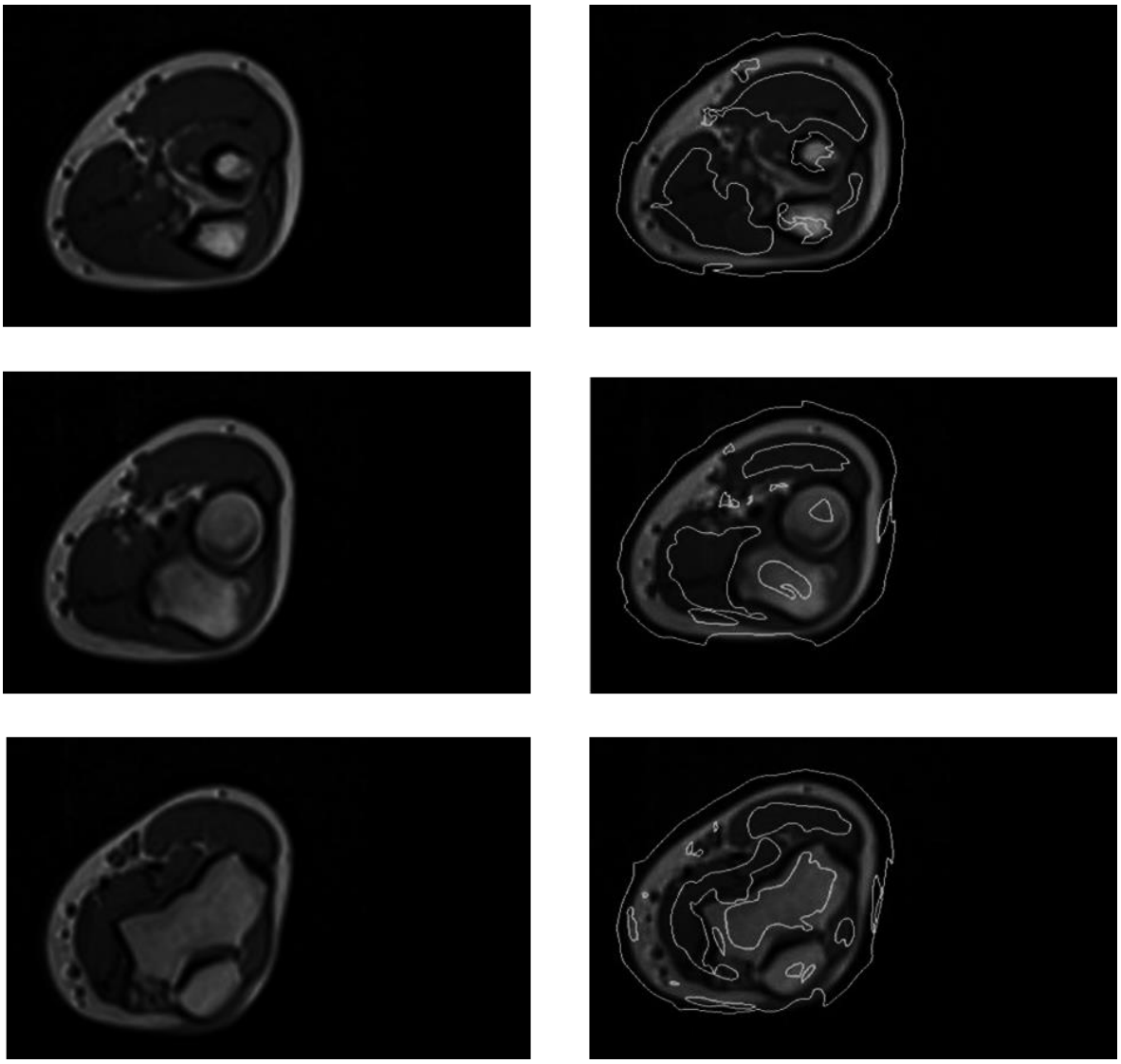

Figure 5.11 : Original MR images of a human arm (left) Multiple active contour initializations (right)

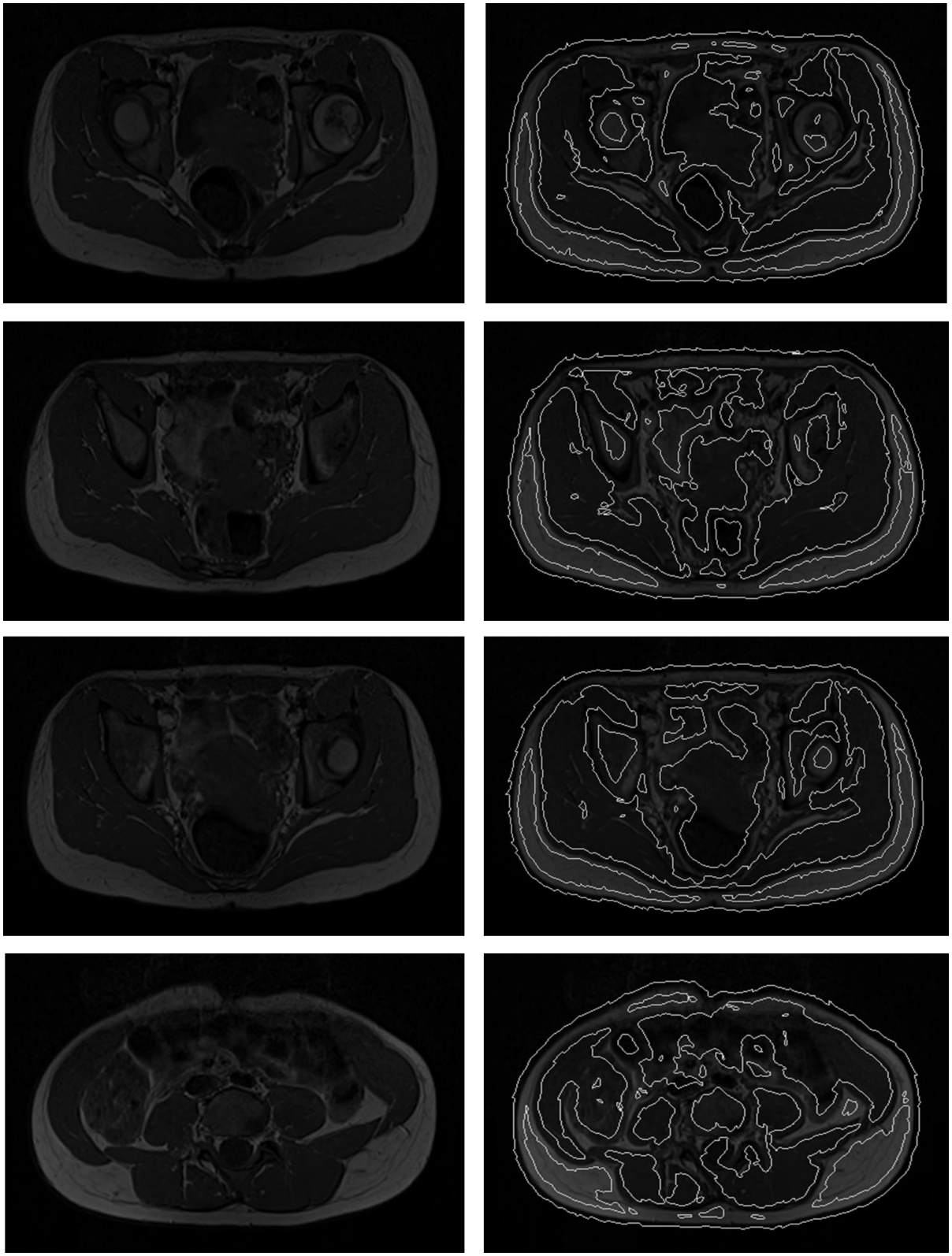

Figure 5.12 : Original MR image of human trunk sections (left) Multiple active contour initializations (right)

As can be observed in these figures, we are dealing with MR images that contain different numbers of anatomical structures and tissues with a great variety in appearance. For example, they contain small bone structures, large and very complex structures for muscle tissues, and long narrow structures for fat tissues. These images also contain some degree of noise and intensity inhomogeneity which are hardly noticeable to a human observer but can be problematic for medical image analysis methods. With all this, however, the proposed initialization method performs fairly well in decomposing the image into its main components and constructs an active contour model for each component. The contours provided for complex muscle structures where intertwined with adjacent structures or those narrow elongated contours for fat parts in the surrounding areas, have been well adapted to the shape of the structures. Moreover, the contours are located very close to the exact boundary of the respective structures. In all our tests, operations were done on the original images without any preprocessing or filtering. It is believed that MR images of human trunk are some of the most challenging images to process, thus, the proposed method should be applicable to other modalities such as CT images.

For the sake of comparison, we have picked out three existing automatic initialization methods; Center of Divergence (CoD), Force Field Segmentation (FFS), and Poisson Inverse Gradient (PIG). In the following, qualitative comparisons of results with these three methods for automatic initialization are presented through figure 5.13 to 5.18. We have used their implementations in MATLAB and in all cases they have been applied on original images without any preprocessing and augmentation procedures. The examples shown here have been selected through series of MR images of human trunk that belong to different axial levels to provide an illustrative diversity in number of objects, their shape and complexity.

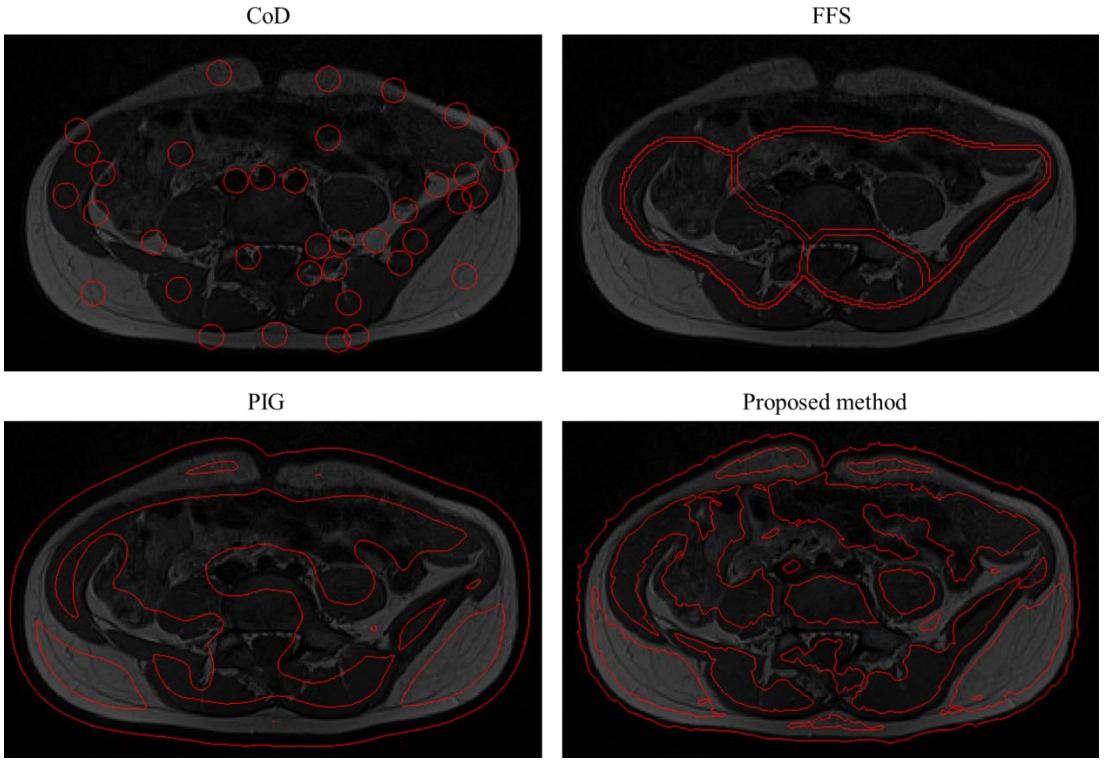

Figure 5.13 : Comparison of automatic initialization on a MR image (example 1)

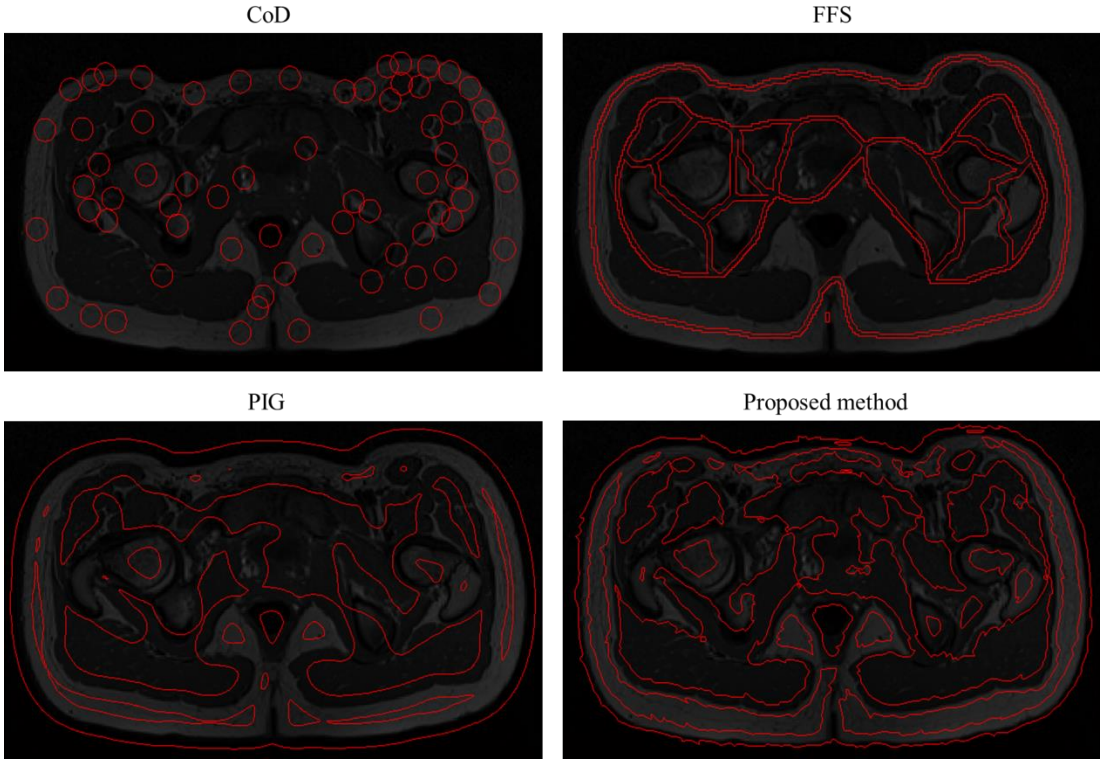

Figure 5.14 : Comparison of automatic initialization on a MR image (example 2)

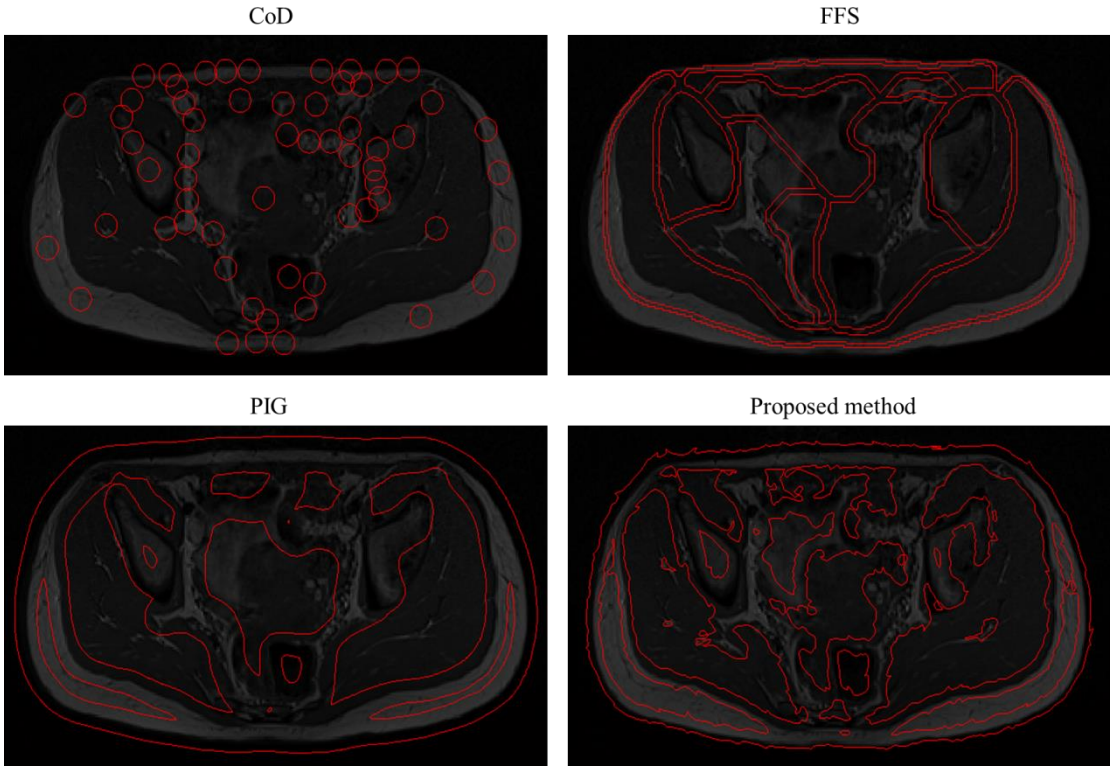

Figure 5.15 : Comparison of automatic initialization on a MR image (example 3)

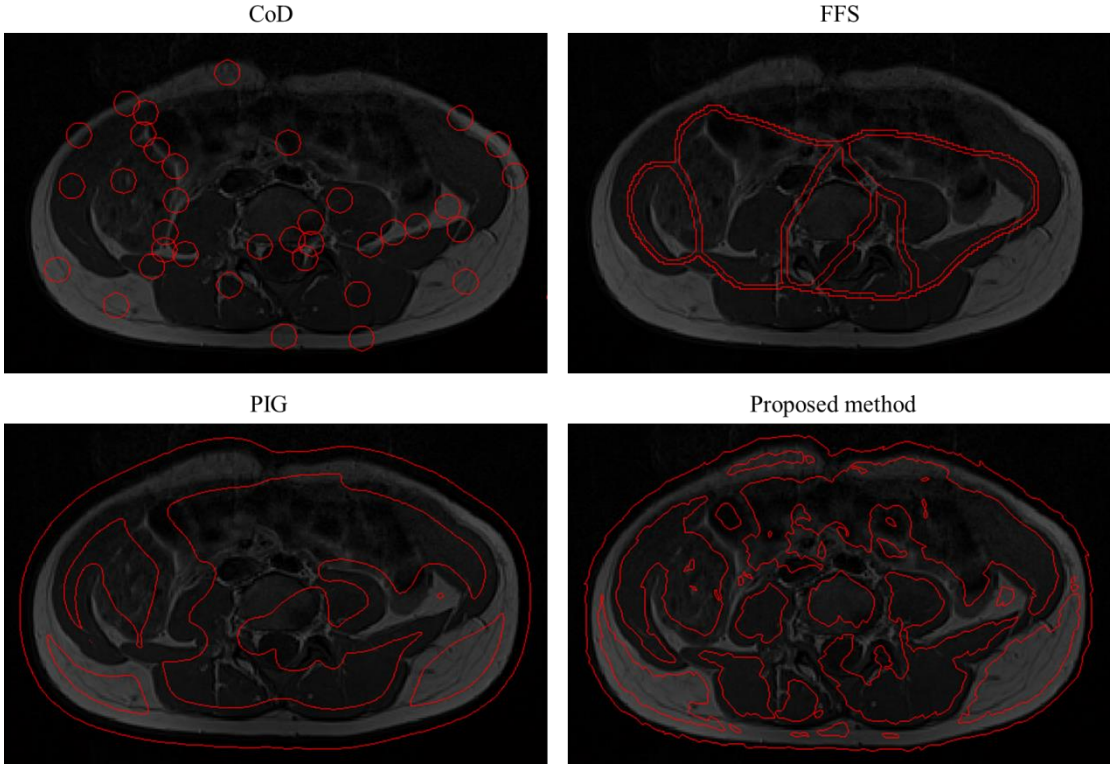

Figure 5.16 : Comparison of automatic initialization on a MR image (example 4)

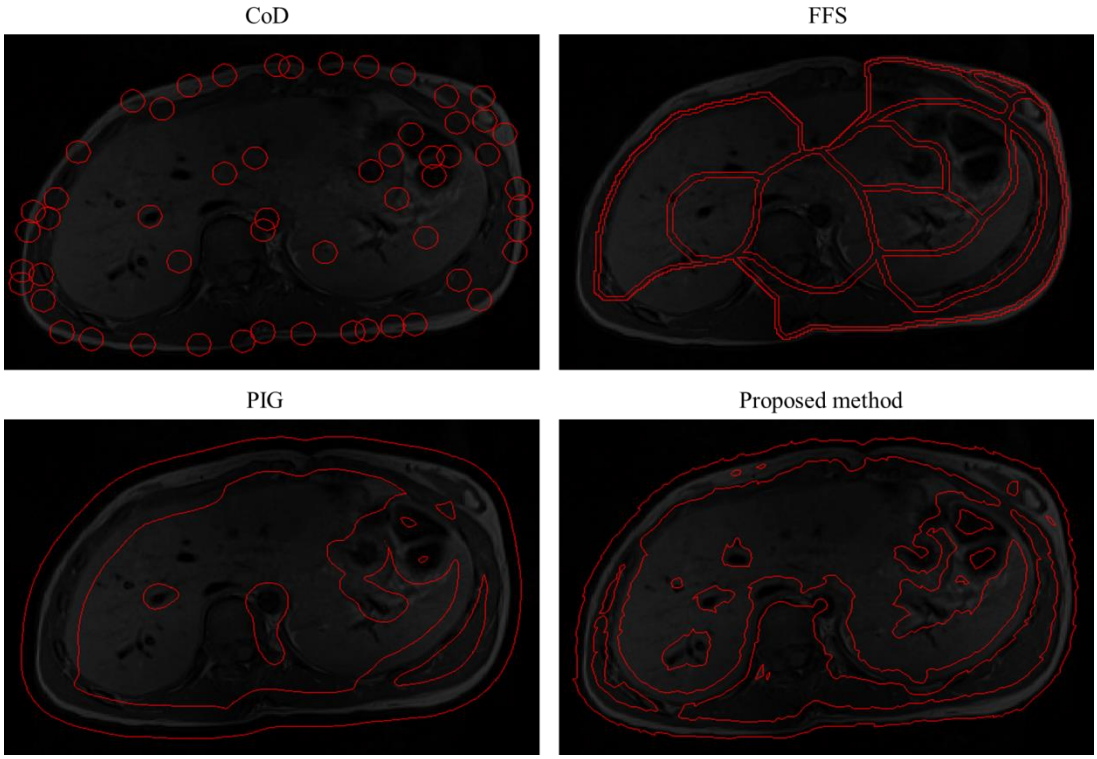

Figure 5.17 : Comparison of automatic initialization on a MR image (example 5)

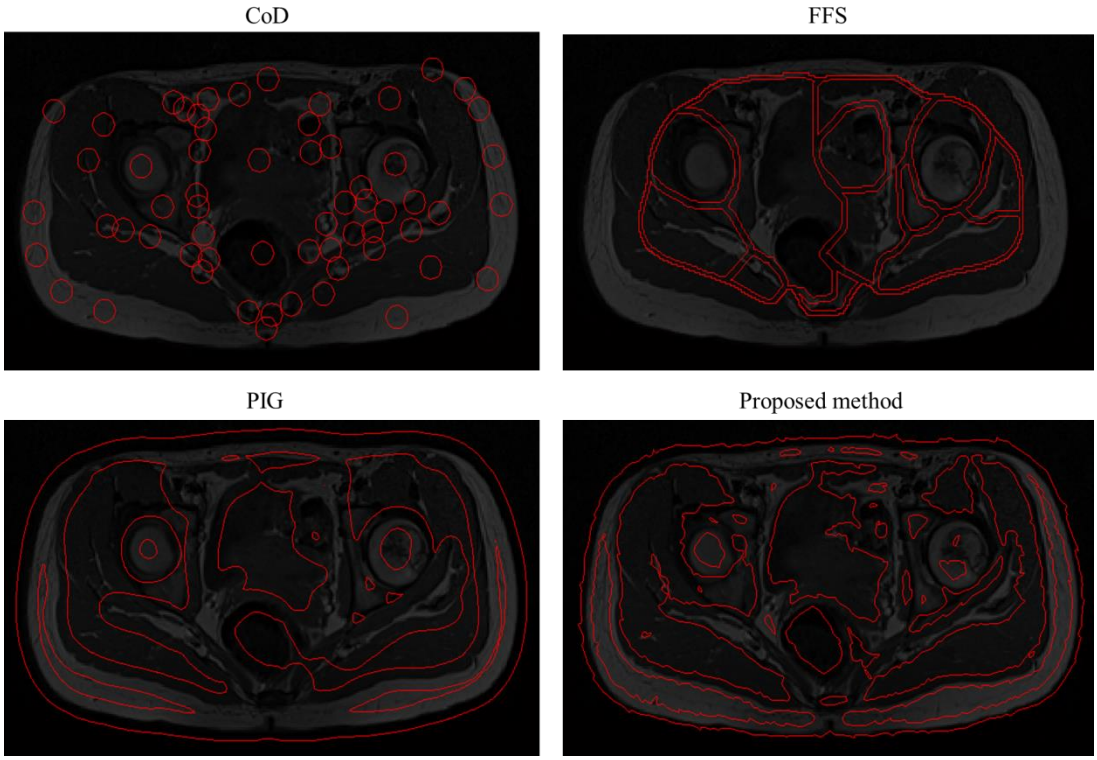

Figure 5.18 : Comparison of automatic initialization on a MR image (example 6)

As can be seen in the figures, very clearly CoD and FFS methods are inefficient for contour estimation on MR images and this indicates that working solely with a force field does not provide a proper solution for multi-object detections from complicated images such as MRI. We therefore need a more abstract level of information, which is provided by the two other methods, PIG and our proposed method. The main difference between PIG and our method is that the PIG approach is based on an energy field computed for the whole image domain without emphasizing boundary information, while the intent of our method is to concentrate on edges and boundary information. Although PIG provides much better results compared to CoD and FFS, it doesn't preserve the boundaries of the organs within the image very well. On the other hand, our proposed approach can respect fairly well the boundaries and provide an adequate contour representation, close to the true boundaries of the organs.

5.3 MR Image Segmentation

In order to demonstrate the effectiveness of the initialization method, we now present final segmentation results and investigate the performance of the segmentation approach qualitatively and quantitatively. Thereby, we have applied the proposed initialization and evolution models for the same image series and some of the results are shown in figure 5.19. In this figure, left images indicate multiple initial contours (red contours) overlaid on the original MR images and right images indicate final segmentation results (green contours) after evolving initial contours. When you compare the initial contours and the final contours after the evolution process, some aspects are noticeable. Each contour has deformed individually and reached the boundary of the respective organ structure without overlapping with adjacent contours and together provide a nice decomposition of the given MR image. Only few parts in the images have remained uncovered which is more apparent in the second example in the figure and the reason is mainly due to the weak edge information in low-contrast areas.

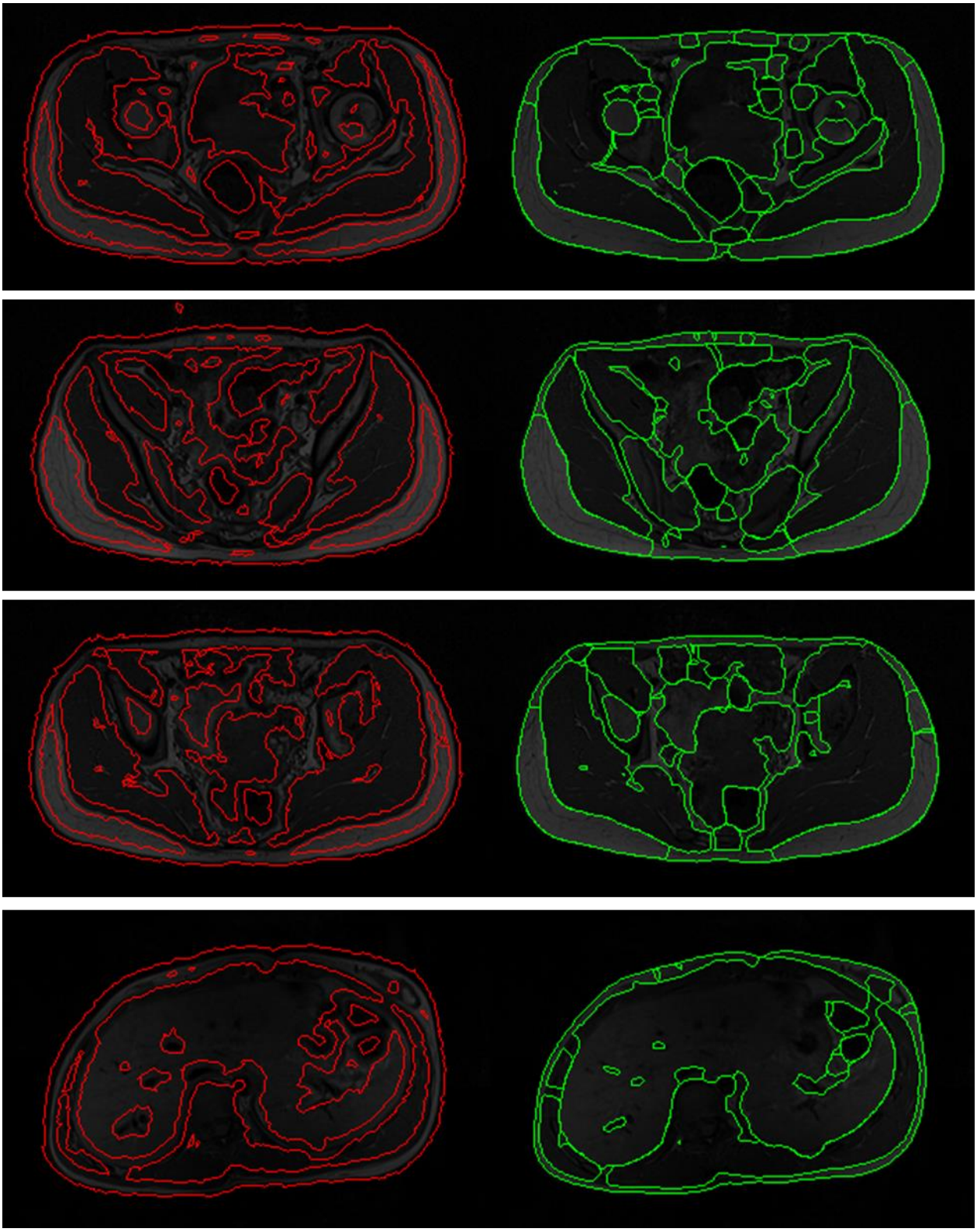

Figure 5.19 : Evolving the initial contours to obtain final segmentation. Initial contours in red (left) Segmentation results in green (right)

In addition, to demonstrate the efficiency in convergence speed of the proposed algorithm we have provided a comparison with three aforesaid automatic initialization methods and analyzed the segmentation performance of all methods in terms of number of active contour models, number of iterations needed for convergence and the convergence time. The result summarized in the following figures and table, confirms that the proposed initialization and evaluation model reduces the computational efforts and improves the correctness of the segmentation results. Figure 5.20 to 5.25 present some examples of qualitative comparison results by performing evolution processes for initialized contour examples presented in figures 5.13 to 5.18. As may be clearly seen, the CoD model results in several small, outspread segments where small portions of different organs are extracted, leaving many parts uncovered. For the FFS model, by having several initial contours without taking individual objects into account make them evolve to the nearest boundaries without aiming for a certain object. Therefore we observe only few contours which have successfully evolved and segmented a single object or a portion of an object in the final segmentation. This approach also generates many noisy contours that were shown before in figure 2.10 and consequently provide very low segmentation performance on these MR images. Thus, it cannot be considered as a reliable model for decomposing MR image into constitutive organs. Indeed, the PIG and the proposed methods outperform these two methods and the main reason is that CoD and FFS initialize the active models far away from features of interest where the evolution models may get trapped in local minima and fail to capture the regions of interest. On the other hand, the PIG and our proposed method provide more meaningful initialization very close to the boundaries of regions, thereby allowing to obtain more relevant segmentation results localizing more objects correctly and providing better decomposition of MR image into constitutive structures and organs. However, the difference between these two is that our proposed method can provide effective segmentation by distinguishing correctly between adjacent regions by successfully analyzing the edge information during the initialization phase.

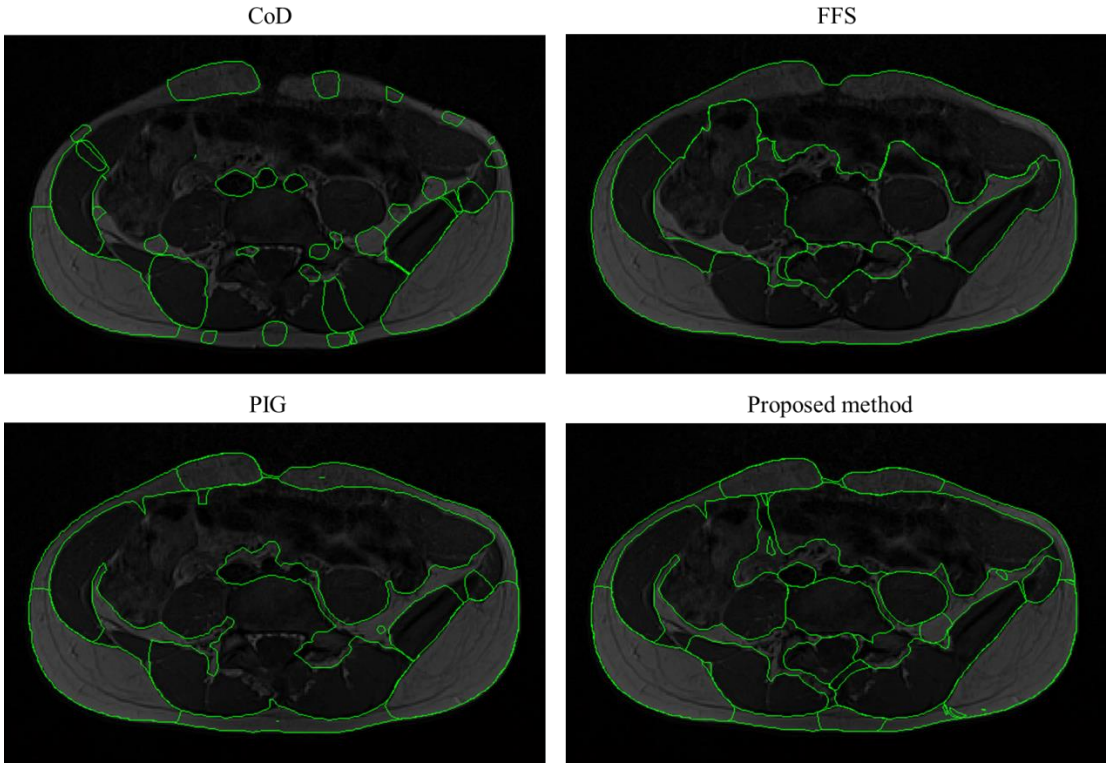

Figure 5.20 : Comparison of segmentation result corresponding to initialization in figure 5.13

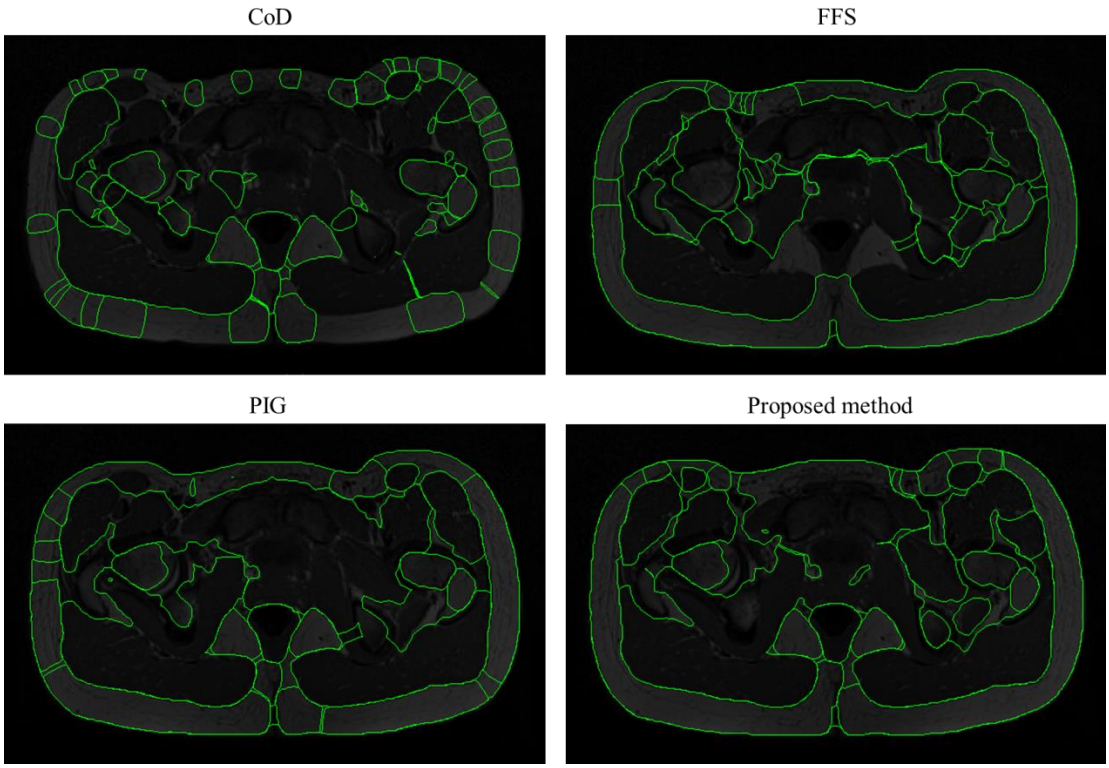

Figure 5.21 : Comparison of segmentation result corresponding to initialization in figure 5.14

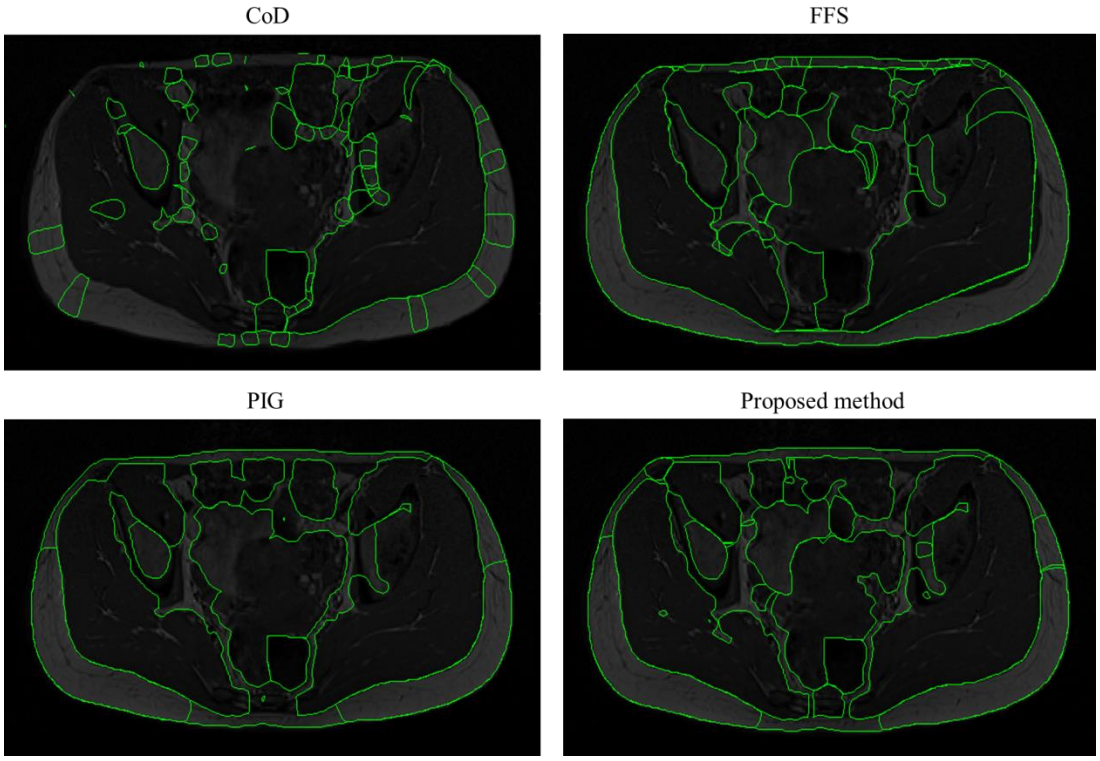

Figure 5.22 : Comparison of segmentation result corresponding to initialization in figure 5.15

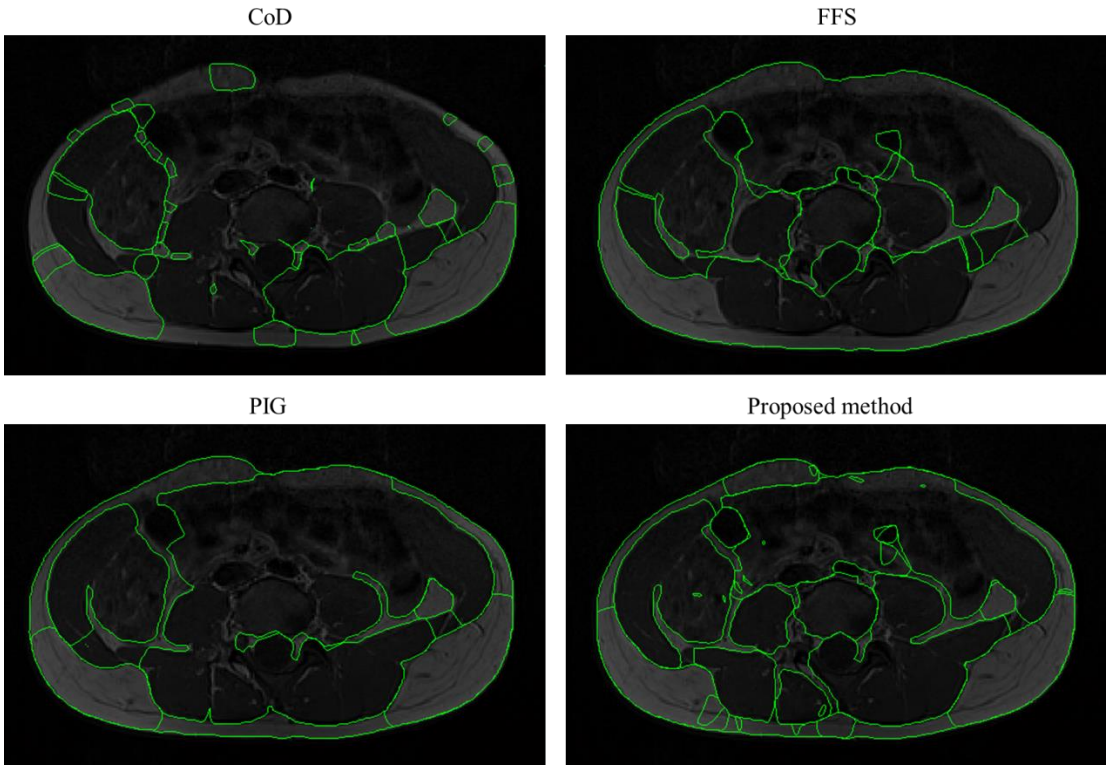

Figure 5.23 : Comparison of segmentation result corresponding to initialization in figure 5.16

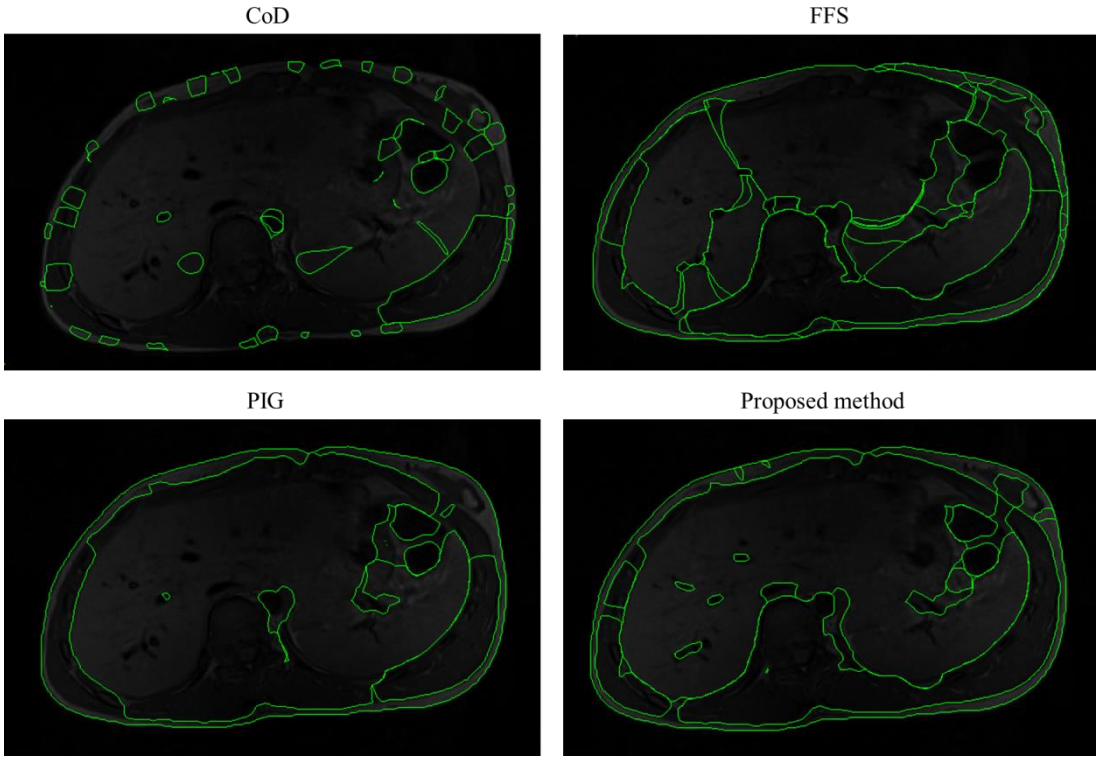

Figure 5.24 : Comparison of segmentation result corresponding to initialization in figure 5.17

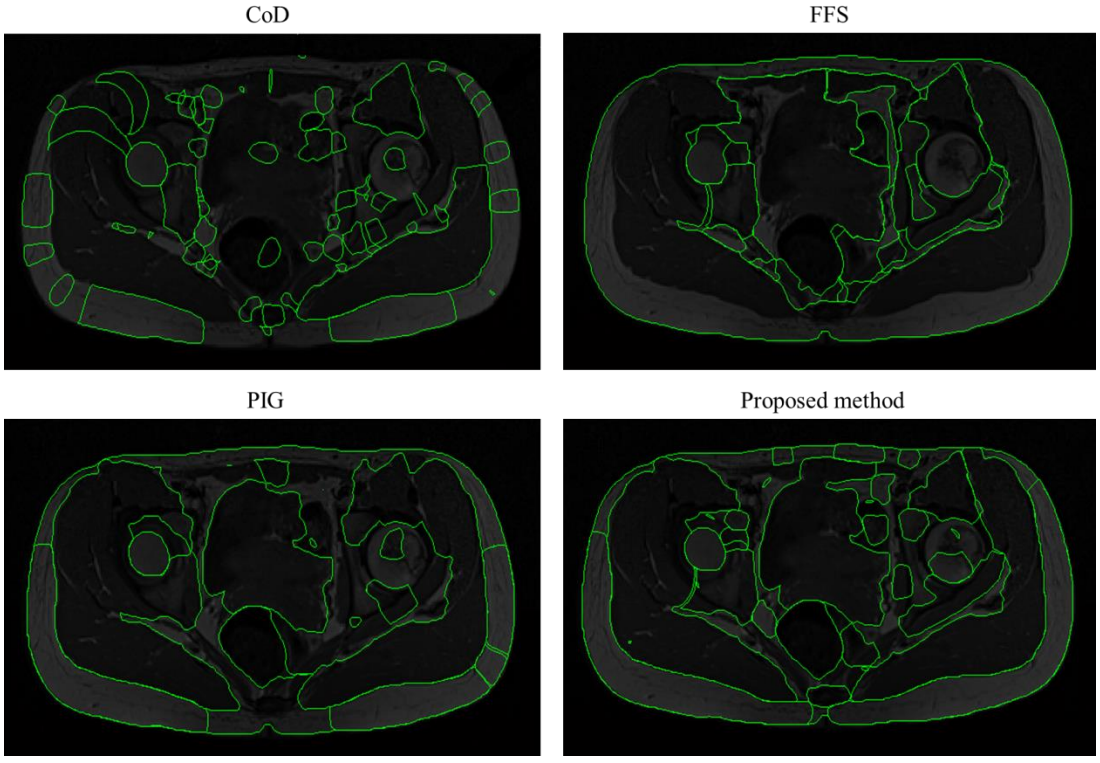

Figure 5.25 : Comparison of segmentation result corresponding to initialization in figure 5.18

Regarding the quantitative analysis of segmentation results, table 5.2 summarizes the comparison results in terms of number of models initialized using the four methods, the number of iteration and convergence time to reach the final segmentation for the aforesaid examples. It is notable that all experiments have been performed using MATLAB 11 and active model parameters including the edge map, the force field, smoothness parameters, and the convergence criteria, are chosen to be identical for all methods. The results in the table reveal that the CoD and FFS methods initialize more active models and many of these models are generated from noisy parts of the image and are therefore useless. Moreover, valid models are generated far from true organ boundaries, which take many iterations before convergence and therefore high convergence times are observed for these methods. On the other hand, the PIG and proposed methods generate reasonable number of models and require fewer iterations. Compare to the PIG method, the proposed method provides more models respecting separate parts that need to be extracted and the number of iterations and convergence time are most of the time lower than for the PIG method because of more appropriate initialization, closer to the true boundaries.

Table 5-2 : Segmentation performance summary for four methods (CoD, FFS, PIG, and Proposed method) on a MR image series

Examples	# of Models Initialized				# of Iterations				Convergence Time (Second)			
	CoD	FFS	PIG	Proposed	CoD	FFS	PIG	Proposed	CoD	FFS	PIG	Proposed
1	87	1472	10	25	273	177	129	81	11.25	14.26	4.30	2.36
2	101	1010	23	30	408	234	153	135	13.20	14.15	6.50	4.71
3	106	1173	12	29	444	243	111	93	12.28	14.34	3.32	2.82
4	70	1496	8	34	273	165	84	309	8.44	13.36	2.52	3.69
5	100	1213	10	18	363	255	162	69	9.57	19.56	3.60	2.00
6	103	1081	19	33	513	642	120	69	13.01	19.81	3.16	3.27

In addition, for quantitative evaluation of the proposed segmentation framework, it is necessary to compare the segmentation results with manual segmentation by physicians. In this regard, we have used a dataset which consists of 50 MR images of human lumbar spine in the sagittal plane where the intervertebral disks have been segmented manually by a clinical expert using the commercially available SliceOmatic software (Tomovision, Montreal). Figure 5.26 indicates an example of these images presented by initialization and segmentation results of the proposed method for detecting intervertebral disks.

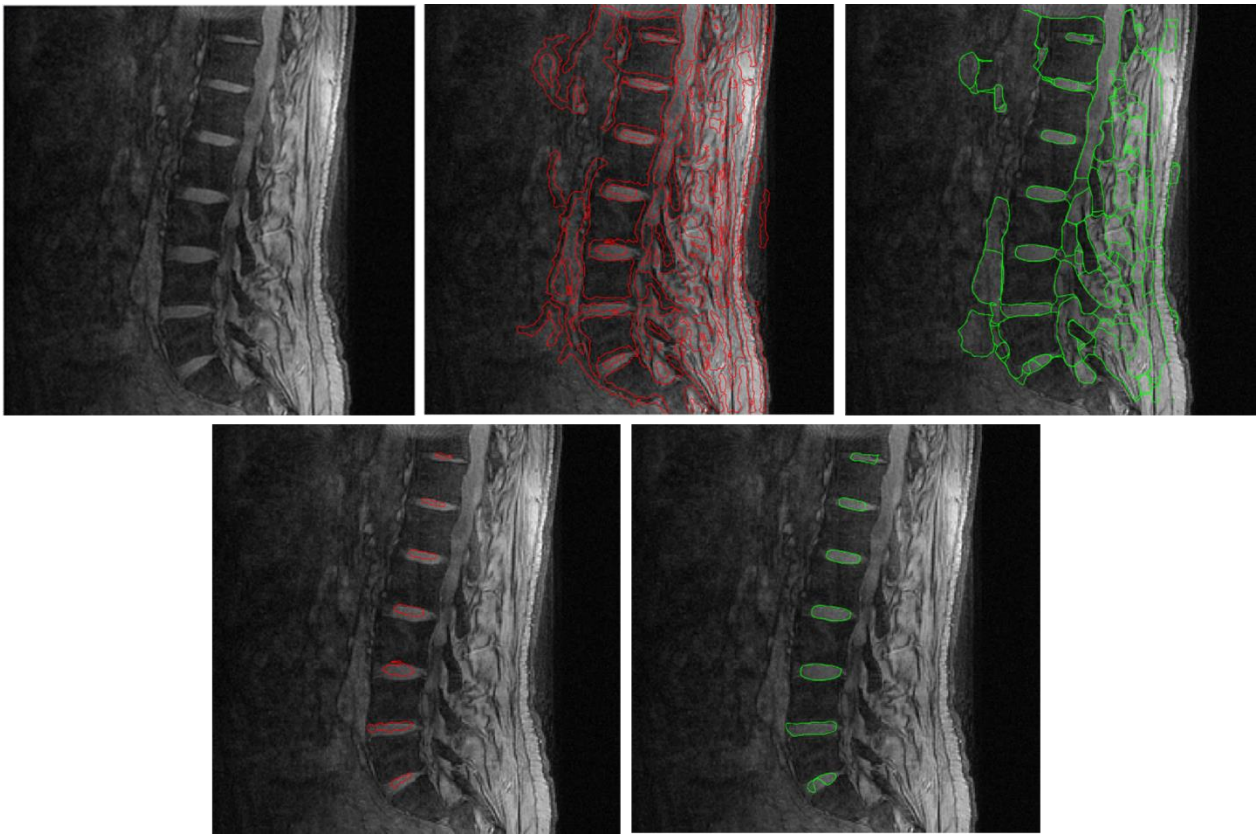

Figure 5.26 : Original image of human lumbar spine, its model initialization, and segmentation (top), selected initialization and segmentation of intervertebral disks (bottom)

At the top row of the figure we have shown the whole process of applying the proposed method on the image. Then we have selected the contours that belong to the intervertebral disks manually from the set of initial contours generated by the proposed initialization method and let them evolve to reach the final segmentation and compared the results with manual segmentation

provided by experts. The Dice Similarity Coefficient (DSC) has been used to evaluate the performance which is defined as:

$$DSC(X,Y) = \frac{2|X \cap Y|}{|X| + |Y|} \quad (5\text{-}2)$$

Where X and Y represent sets of pixels in an intervertebral disk resulting from the proposed method and manual segmentation. The $DSC(X,Y)$ function returns values in the range [0,1] where 0 means no overlap and 1 means complete overlap between two segmentation results. It has been reported that DSC values greater than 0.7 are considered as a good segmentation performance [127, 128]. Figure 5.27 and 5.28 provide the results obtained from similarity measurements between the proposed segmentation and manual segmentation results. The mean and the standard deviation of DSC computed over all 50 cases are 0.8777 and 0.0408 respectively. As can be seen, all DSC values are greater than the threshold for good segmentation performance.

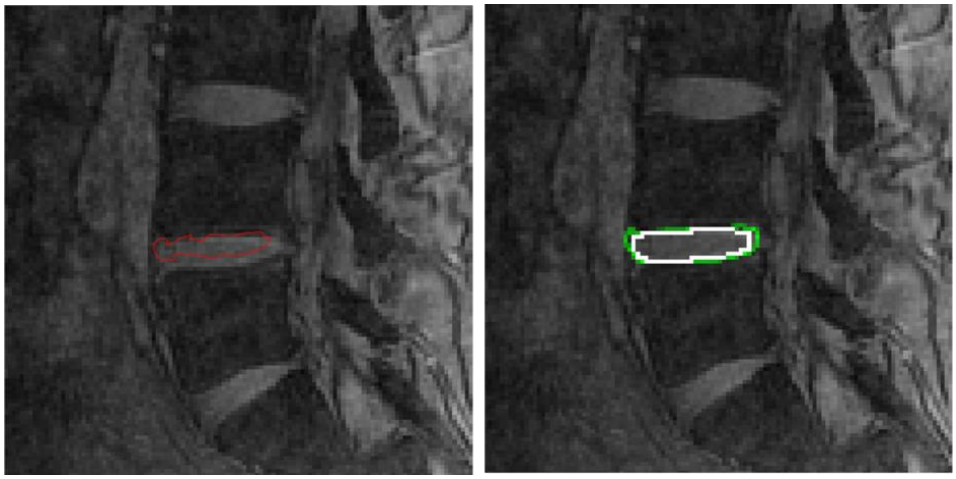

Figure 5.27 : Initial contour for an intervertebral disk (left), comparison between our segmentation in green and manual segmentation in white (right)

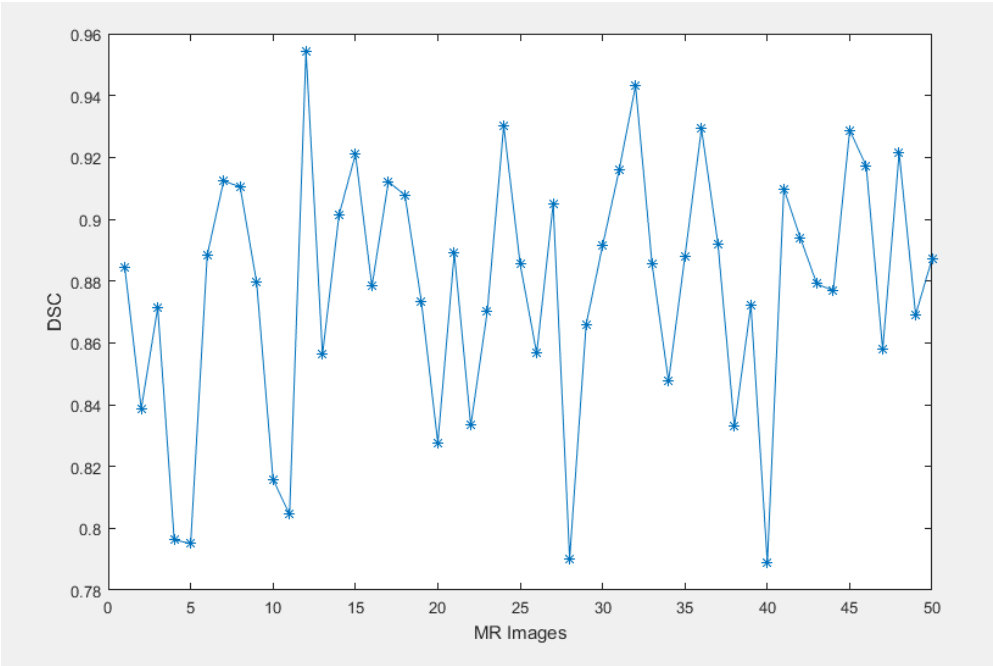

Figure 5.28 : Graph of Dice similarity results for all dataset

From all of our comparison experiments, we can conclude that the proposed segmentation framework can provide an effective initialization for multi-object segmentation in the sense of generating a proper number of active models very close to the true boundaries of different organs which need fewer numbers of iterations to converge. It also can provide good segmentation results where the accuracy of the final segmentations is comparable to expert manual segmentation.

5.4 General Discussion

This chapter aimed to alleviate some limitations of existing methods for multi-object MR image segmentation. We have studied two aspects specifically, *a*) how to improve mesh-based image representation and *b*) how to use this mesh-based image representation to segment several organs and tissues from MR images automatically. The proposed methodology established several specific objectives that led to some original tools for assembling an automatic multi-object MR image segmentation framework. First, we have introduced a new metric computation approach for anisotropic mesh adaptation to bring improvement in mesh-based image representation.

Second, we have employed an anisotropic adaptive mesh for automatic active contour initialization which led to a more efficient approach for multi-object MR segmentation. The general discussion highlights the main improvements done in these steps and also relates them with previous works.

An improvement was made in generating anisotropic adaptive mesh by using directional Hessian computation considering the neighbors along that direction. In comparison to the previous methods, there is a small reduction (less than 5%) in the number of mesh elements for those synthetic images that contain edges only in axis-aligned directions. This small difference is due to the size of the neighborhood (kernel size) used to compute the derivatives in each methods. However, the real potential of the proposed method manifests itself for those images that contain non-axis-aligned edge directions. The proposed directional metric computation leads to a considerable reduction (more than 20%) in mesh elements. Another important observation is the increase of element anisotropy and their alignment to the image content. As can be seen in figure 5.5 and 5.7, we have extracted the elements with aspect ratio greater than 2, there are two improvements using the proposed approach. The first one is that the great numbers of anisotropic elements are located where the image edges are found and they are aligned adequately with the edge directions. The second one which can be seen from the histograms is that the total number of elements with higher aspect ratio is increased compared to other approaches. Thus, the proposed method has presented the anisotropic features of the image with highly elongated elements and adequate alignment which is desired in the anisotropic mesh adaptation. These properties indicate that the proposed mesh-based image can provide a better representation for a given image. The test for regaining the original image from the corresponding mesh confirms that the original image can be recovered from the proposed anisotropic mesh with less error compared to other approaches.

Another aspect of the proposed methodology is automatic active contour initialization by using anisotropic adaptive mesh. We have shown that anisotropic adaptive meshes constructed from MR images contain high-level information about MR image content which can be used to localize different organs and tissues in the image. Based upon this localization we can initialize several active contours for determining the MR image structures automatically. According to the comparison with other automatic active contour initialization methods (table 5-2), the proposed method has presented a reasonable number of active contours for a given MR image. Unlike the

other methods, the proposed initialization approach can handle noise in the image more properly and can localize the objects in the image more accurately as can be seen in the example images. This appropriate initialization leads to better segmentation results in terms of speed and accuracy. Table 5-2 expresses that having such initial contours close to the exact boundaries of the objects has reduced the number of iterations and consequently reduced the convergence time. On the other hand, segmentation validation with ground truth using Dice coefficient and obtaining DSC average 0.8777 with standard deviation 0.0408 across the 50 cases, acknowledge that the proposed method has achieved good segmentation performance.

5.4.1 Limitation

Notwithstanding the advantages of the proposed method for automatic multi-object MR image segmentation; there is a limitation that was not fully investigated.

Low contrast area: In some of the MR images there are some parts which have not been detected due to the very low contrast between these parts and the surrounding tissues. It seems the metric construction based on Hessian information is not very successful to reveal anisotropic features of the low contrast areas or weak edges. For example in the figure 5.29 the two bone structures indicated with white contours are not captured during the localization process and therefore there are no initial contours for these parts. It is clear that further work remains to be done toward a better MR image parsing for these cases.

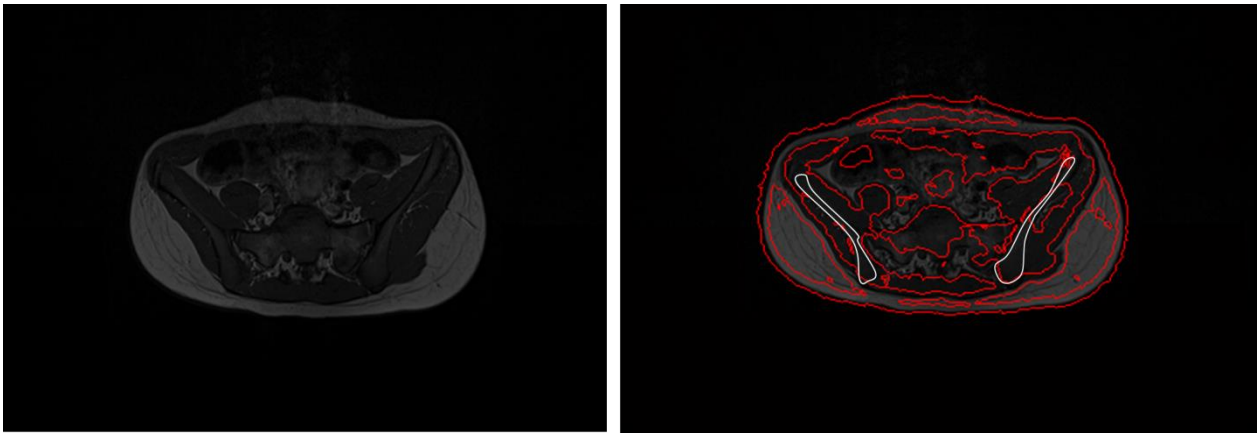

Figure 5.29 : Original image (left) and its proposed initialization with white contours superimposed on it to indicate the missing parts (right)

It is notable that this limitation also exists for the other three mentioned methods for active contour initialization (figure 5.30).

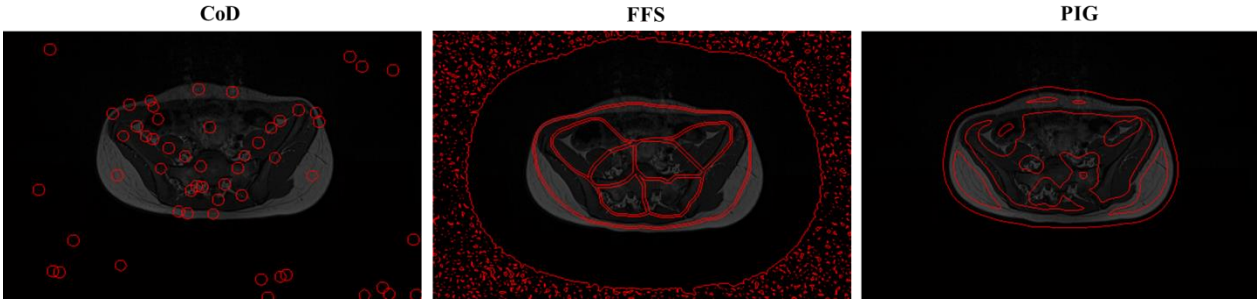

Figure 5.30 : The other three methods also failed to capture the bone structures in the example image in figure 5.29

Limited to 2D: the proposed algorithm is designed for 2D image where we generate 2D meshes construct curves to initialize active contours. Extending the algorithm to 3D and deal with volumetric images directly will need generating 3D meshes and constructing active surfaces which are not trivial and computationally efficient tasks. Therefore the recommended way for building 3D model is to discretize the contours and connects the corresponding nodes from successive slices.

Topology change: Since we have implemented the algorithm using parametric deformable models, there is no automatic handling of topology change. We have not provided any solution to handle topology change and if there are adjacent active models belong to the same part which can be merged together, the method just output them as separate contours.

CHAPTER 6 CONCLUSION

This thesis has addressed the general problem of automatic multi-object MR image segmentation by incorporating anisotropic mesh adaptation. The literature, reviewed in Chapter 2, highlighted the challenges of finding appropriate methods for MR image segmentation and challenges of extracting multiple organs and tissues within the image automatically and also revealed the current limitations of the state-of-the-art. Further, mesh-based image representation methods with their advantages and limitations in image analysis area are described.

According to the literature, deformable models have been proven very successful methods for challenging multi-object MR image segmentation. The main limitation for these methods toward general-purpose automatic segmentation is in their initialization phase. A suitable initialization can prevent failure caused by entrapment in local minima and help capture the boundary of objects. It will also reduce the number of iterations that the method needs to converge. The existing automatic active contour initialization methods are not found so efficient for detecting multiple organs and tissues from MR data. Therefore during the thesis we have proposed a new automatic active contour initialization approach by employing anisotropic adaptive meshes. We have concluded that anisotropic adaptive mesh can be used to reveal more robust and accurate information about edge structure and orientation from eigenvalues and eigenvectors of the defined metric. In other words, anisotropic adaptive mesh constructed from MR image contains higher level, abstract information about anatomical structures of the organs and tissues within the image retained as the elements shape and orientation. Using this information we have localized different anatomical structures in a given MR image and automatically initialized several active contours using B-Spline curves. This initialization step followed by contour evolution based on VFC external force field leads to a final segmentation with better performance and accuracy.

Also we have shown that we can improve the mesh-based image representation by introducing a new metric computation approach. Based on the experiments, the existing anisotropic adaptive meshes which are used for mesh-based image representation are not very efficient. The main limitation of constructing metric tensors using these methods manifests itself in inadequate mesh element alignment to inclined edges of the image. Therefore, a new metric computation based on directional Hessian matrix considering neighbors along the edge direction was proposed which

has improved the mesh anisotropy along non-orthogonal edges for anisotropic mesh adaptation. The results and improvements from the research objectives have been discussed individually in Chapter 5. The main finding and contributions are briefly reminded in the following.

6.1 Contributions

The work described in this thesis, which incorporates anisotropic adaptation technique into a deformable model-based segmentation for detection of multiple organs in MR images, presents the following major contributions:

1. **Improving mesh anisotropy along inclined edges in a mesh-based image representation**. This leads to an adaptation process that can: align adequately element edges with the edges present in an image, regardless of the edge direction, improve the quality of the anisotropic meshing and reduce the number of mesh elements which are considered as important properties in mesh-based image representation and related numerical simulations application in biomedical engineering. The originality of this representation lies in our new metric computation for anisotropic adaptation process.
2. **Introducing mesh-based active contour initialization**. This leads to an automatic initialization of several active models by exploiting an adaptive mesh generation technique. This enables us to extract initial object boundaries close to the exact boundaries of multiple objects simultaneously, which speeds up the evolution process and prevents the model to converge to local minima. The originality of the proposed initialization is in incorporating anisotropic mesh adaptation in active contour initialization.
3. **Introducing a multi-object MR image segmentation framework**. This represents an automatic mesh-based segmentation method that allows evolving several active contours simultaneously using vector field convolution as an external force. Experiments and comparisons show the advantages of the new method in detecting multiple organs in MR images.

Solving the aforesaid problems has many practical and clinical applications in MR image analysis especially when the exact shape of the anatomical structures is of great interest. One of the most demanding examples of such applications is the segmentation of MR images of the human trunk. An important clinical usage of this segmentation is to create a 3D patient-specific model of anatomical structures for simulation purposes. In this regard, a sequence of 2D transversal slices is segmented to extract the contours of different anatomical structures. Then the contours are discretized to a number of nodes, and the corresponding nodes from successive slices are connected to create a tetrahedral mesh as a 3D model.

The next section now establishes the main recommendations, based on the contributions found in the thesis.

6.2 Recommendations and Perspectives

In our approach for anisotropic mesh adaptation, the metric is rather simple: It is constructed from Hessian matrix containing second partial derivatives of image pixels. This metric permits fast implementation and work fairly well in our approach; however it failed to reveal anisotropic features in the areas with low contrast. As future work, we recommend to construct a metric from more advanced techniques such as Shearlet [129] to extract anisotropic features from an image and perform multiresolution analysis to alleviate this limitation.

Also the idea presented for segmenting multiple organs and tissues from MR images can be applied to other medical image modalities such as CT images, etc. where the boundaries of the organs need to be well defined.

In our model, we have used an explicit representation for deformable models and presented active contour models by parametric B-Spline curves. This representation allows direct interaction with the model and provides the advantages of high computational efficiency and simple implementation. However, topology changes such as splitting or merging contours during the deformation can be difficult to cope with. Therefore, it is worth also implementing the models implicitly with geometric deformable models which have the advantage of naturally handling the topology changes.

BIBLIOGRAPHY

[1] P. V. Prasad, *Magnetic Resonance Imaging: Methods and Biologic Applications*: Springer, 2006.

[2] J. L. Prince and J. M. Links, *Medical Imaging Signals and Systems*: Pearson, 2014.

[3] U. Vovk, F. Pernus, and B. Likar, "A Review of Methods for Correction of Intensity Inhomogeneity in MRI," *Medical Imaging, IEEE Transactions on,* vol. 26, pp. 405-421, 2007.

[4] P. J. Frey and P. L. George, *Mesh generation: application to finite elements*: Wiley Online Library, 2000.

[5] F. Alauzet, P. J. Frey, P. L. George, and B. Mohammadi, "3D transient fixed point mesh adaptation for time-dependent problems: Application to CFD simulations," *J. Comput. Phys.,* vol. 222, pp. 592-623, 2007.

[6] D. Ait-Ali-Yahia, G. Baruzzi, W. G. Habashi, M. Fortin, J. Dompierre, and M.-G. Vallet, "Anisotropic mesh adaptation: towards user-independent, mesh-independent and solver-independent CFD. Part II. Structured grids," *International Journal for Numerical Methods in Fluids,* vol. 39, pp. 657-673, 2002.

[7] J. Dompierre, M.-G. Vallet, Y. Bourgault, M. Fortin, and W. G. Habashi, "Anisotropic mesh adaptation: towards user-independent, mesh-independent and solver-independent CFD. Part III. Unstructured meshes," *International Journal for Numerical Methods in Fluids,* vol. 39, pp. 675-702, 2002.

[8] W. G. Habashi, J. Dompierre, Y. Bourgault, D. Ait-Ali-Yahia, M. Fortin, and M.-G. Vallet, "Anisotropic mesh adaptation: towards user-independent, mesh-independent and solver-independent CFD. Part I: general principles," *International Journal for Numerical Methods in Fluids,* vol. 32, pp. 725-744, 2000.

[9] A. Loseille, A. Dervieux, and F. Alauzet, "Fully anisotropic goal-oriented mesh adaptation for 3D steady Euler equations," *J. Comput. Phys.,* vol. 229, pp. 2866-2897, 2010.

[10] P. Labbé, J. Dompierre, M. G. Vallet, F. Guibault, and J. Y. Trépanier, "A universal measure of the conformity of a mesh with respect to an anisotropic metric field," *International Journal for Numerical Methods in Engineering,* vol. 61, pp. 2675-2695, 2004.

[11] K.-F. Tchon, M. Khachan, F. Guibault, and R. Camarero, "Three-dimensional anisotropic geometric metrics based on local domain curvature and thickness," *Computer-Aided Design,* vol. 37, pp. 173-187, 2005.

[12] C. Gruau and T. Coupez, "3D tetrahedral, unstructured and anisotropic mesh generation with adaptation to natural and multidomain metric," *Computer Methods in Applied Mechanics and Engineering,* vol. 194, pp. Pages 4951-4976, 2005-11 2005.

[13] F. Alauzet, "Size gradation control of anisotropic meshes," *Finite Elem. Anal. Des.*, vol. 46, pp. 181-202, 2010.

[14] J. Dompierre, Y. Mokwinski, M.-G. Vallet, and F. Guibault, "On ellipse intersection and union with application to anisotropic mesh adaptation," *Engineering with Computers*, vol. 33, pp. 745–766, 2017.

[15] P. L. George, "Gamanic3d, adaptive anisotropic tetrahedral mesh generator," Technical Note, INRIA, 2003.

[16] C. L. Bottasso, "Anisotropic mesh adaption by metric-driven optimization," *International Journal for Numerical Methods in Engineering*, vol. 60, pp. 597-639, 2004.

[17] X. Li, M. S. Shephard, and M. W. Beall, "3D anisotropic mesh adaptation by mesh modification," *Computer Methods in Applied Mechanics and Engineering*, vol. 194, pp. 4915-4950, 2005.

[18] J. Dompierre, P. Labbé, and F. Guibault. OORT (Object-Oriented Remeshing Toolkit) [Online]. Available: http://www.magnu.polymtl.ca/oort

[19] A. Loseille and R. Löhner, "On 3D Anisotropic Local Remeshing for Surface, Volume and Boundary Layers," in *Proceedings of the 18th International Meshing Roundtable*, B. W. Clark, Ed., ed Berlin, Heidelberg: Springer Berlin Heidelberg, 2009, pp. 611-630.

[20] G. Compère, J.-F. Remacle, J. Jansson, and J. Hoffman, "A mesh adaptation framework for dealing with large deforming meshes," *International Journal for Numerical Methods in Engineering*, vol. 82, pp. 843-867, 2010.

[21] P. Labbé, J. Dompierre, M.-G. Vallet, and F. Guibault, "Verification of three-dimensional anisotropic adaptive processes," *International Journal for Numerical Methods in Engineering*, vol. 88, pp. 350-369, 2011.

[22] O. Courchesne, F. Guibault, J. Dompierre, and F. Cheriet, "Adaptive Mesh Generation of MRI Images for 3D Reconstruction of Human Trunk," in *Image Analysis and Recognition*. vol. 4633, M. Kamel and A. Campilho, Eds., ed: Springer Berlin Heidelberg, 2007, pp. 1040-1051.

[23] R. Löhner, "Automatic unstructured grid generators," *Finite Elements in Analysis and Design*, vol. 25, pp. 111-134, 1997.

[24] S. J. Owen, "A Survey of Unstructured Mesh Generation Technology," in *IMR*, 1998, pp. 239-267.

[25] M. D. Adams, "A Flexible Content-Adaptive Mesh-Generation Strategy for Image Representation," *IEEE Transactions on Image Processing*, vol. 20, pp. 2414-2427, 2011.

[26] M. Sarkis and K. Diepold, "A fast solution to the approximation of 3D scattered point data from stereo images using triangular meshes," in *2007 7th IEEE-RAS International Conference on Humanoid Robots*, 2007, pp. 235-241.

[27] L. Demaret and A. Iske, "Adaptive image approximation by linear splines over locally optimal delaunay triangulations," *IEEE Signal Processing Letters*, vol. 13, pp. 281-284, 2006.

[28] L. Demaret, N. Dyn, and A. Iske, "Image compression by linear splines over adaptive triangulations," *Signal Process.*, vol. 86, pp. 1604-1616, 2006.

[29] D. Su and P. Willis, "Image Interpolation by Pixel-Level Data-Dependent Triangulation," *Computer Graphics Forum*, vol. 23, pp. 189-201, 2004.

[30] J. G. Brankov, Y. Yongyi, and M. N. Wernick, "Tomographic image reconstruction based on a content-adaptive mesh model," *IEEE Transactions on Medical Imaging*, vol. 23, pp. 202-212, 2004.

[31] Y. Yang, M. N. Wernick, and J. G. Brankov, "A fast approach for accurate content-adaptive mesh generation," *Trans. Img. Proc.*, vol. 12, pp. 866-881, 2003.

[32] Y. Xiaohua, B. S. Bryan, and T. W. Sederberg, "Image reconstruction using data-dependent triangulation," *IEEE Computer Graphics and Applications*, vol. 21, pp. 62-68, 2001.

[33] G. Ramponi and S. Carrato, "An adaptive irregular sampling algorithm and its application to image coding," *Image and Vision Computing*, vol. 19, pp. 451-460, 2001.

[34] F. Davoine, M. Antonini, J. M. Chassery, and M. Barlaud, "Fractal image compression based on Delaunay triangulation and vector quantization," *IEEE Transactions on Image Processing*, vol. 5, pp. 338-346, 1996.

[35] H. Edelsbrunner, "Triangulations and meshes in computational geometry," *Acta Numerica*, vol. 9, pp. 133-213, 2000.

[36] M. Sarkis and K. Diepold, "Content Adaptive Mesh Representation of Images Using Binary Space Partitions," *IEEE Transactions on Image Processing*, vol. 18, pp. 1069-1079, 2009.

[37] S. Bougleux, G. Peyré, and L. D. Cohen, "Image compression with anisotropic triangulations," in *2009 IEEE 12th International Conference on Computer Vision*, 2009, pp. 2343-2348.

[38] D. Terzopoulos and M. Vasilescu, "Sampling and reconstruction with adaptive meshes," in *Computer Vision and Pattern Recognition, 1991. Proceedings CVPR '91., IEEE Computer Society Conference on*, 1991, pp. 70-75.

[39] M.-G. Vallet, C. M. Manole, J. Dompierre, S. Dufour, and F. Guibault, "Numerical comparison of some Hessian recovery techniques," *International Journal for Numerical Methods in Engineering*, vol. 72, pp. 987-1007, 2007.

[40] R. C. Almeida, R. A. Feijóo, A. C. Galeao, C. Padra, and R. S. Silva, "Adaptive finite element computational fluid dynamics using an anisotropic error estimator," *Computer Methods in Applied Mechanics and Engineering*, vol. 182, pp. 379-400, 2000.

[41] J. Dompierre, P. Labbé, and F. Guibault, "Controlling approximation error," in *Computational Fluid and Solid Mechanics 2003*, ed Oxford: Elsevier Science Ltd, 2003, pp. 1929-1932.

[42] F. Hecht, "A fews snags in mesh adaptation loops," in *Proceedings of the 14th International Meshing Roundtable*, B. W. Hanks, Ed., ed Berlin, Heidelberg: Springer Berlin Heidelberg, 2005, pp. 301-311.

[43] C. M. Manole, M.-G. Vallet, J. Dompierre, and F. Guibault, "Benchmarking of a second order derivatives recovery method of a piecewise linear scalar field," in *Proceedings of IMACS 2005*, 2005.

[44] W. T. Freeman and E. H. Adelson, "The design and use of steerable filters," *IEEE Transactions on Pattern Analysis and Machine Intelligence*, vol. 13, pp. 891-906, 1991.

[45] J. Luo, K. Ying, P. He, and J. Bai, "Properties of Savitzky-Golay digital differentiators," *Digit. Signal Process.*, vol. 15, pp. 122-136, 2005.

[46] H. Farid and E. P. Simoncelli, "Differentiation of discrete multidimensional signals," *IEEE Transactions on Image Processing*, vol. 13, pp. 496-508, 2004.

[47] H. Farid and E. P. Simoncelli, "Optimally rotation-equivariant directional derivative kernels," in *Computer Analysis of Images and Patterns: 7th International Conference, CAIP '97 Kiel, Germany, September 10–12, 1997 Proceedings*, G. Sommer, K. Daniilidis, and J. Pauli, Eds., ed Berlin, Heidelberg: Springer Berlin Heidelberg, 1997, pp. 207-214.

[48] A. K. Jain, R. P. W. Duin, and M. Jianchang, "Statistical pattern recognition: a review," *Pattern Analysis and Machine Intelligence, IEEE Transactions on*, vol. 22, pp. 4-37, 2000.

[49] J. J. Verbeek, N. Vlassis, and B. Kröse, "Efficient greedy learning of Gaussian mixture models," *Neural computation*, vol. 15, pp. 469-485, 2003.

[50] C. L. Tan and J. C. Rajapakse, "Tissue segmentation of MR images using first order polynomial modeling," in *Neural Information Processing, 2002. ICONIP'02. Proceedings of the 9th International Conference on*, 2002, pp. 1661-1665.

[51] A. P. Zijdenbos and B. M. Dawant, "Brain segmentation and white matter lesion detection in MR images," *Critical reviews in biomedical engineering*, vol. 22, pp. 401-465, 1994.

[52] J. C. Bezdek, L. O. Hall, and L. P. Clarke, "Review of MR image segmentation techniques using pattern recognition," *Medical Physics*, vol. 20, pp. 1033-1048, 1993.

[53] K. Held, E. R. Kops, B. J. Krause, W. M. I. I. I. Wells, R. Kikinis, and H. W. Muller-Gartner, "Markov random field segmentation of brain MR images," *Medical Imaging, IEEE Transactions on*, vol. 16, pp. 878-886, 1997.

[54] M. W. Woolrich and T. E. Behrens, "Variational bayes inference of spatial mixture models for segmentation," *Medical Imaging, IEEE Transactions on*, vol. 25, pp. 1380-1391, 2006.

[55] K. Van Leemput, F. Maes, D. Vandermeulen, and P. Suetens, "Automated model-based bias field correction of MR images of the brain," *Medical Imaging, IEEE Transactions on*, vol. 18, pp. 885-896, 1999.

[56] K. Van Leemput, F. Maes, D. Vandermeulen, and P. Suetens, "Automated model-based tissue classification of MR images of the brain," *Medical Imaging, IEEE Transactions on*, vol. 18, pp. 897-908, 1999.

[57] D. J. Withey and Z. J. Koles, "Medical Image Segmentation: Methods and Software," in *Noninvasive Functional Source Imaging of the Brain and Heart and the International Conference on Functional Biomedical Imaging, 2007. NFSI-ICFBI 2007. Joint Meeting of the 6th International Symposium on*, 2007, pp. 140-143.

[58] A. W. C. Liew and Y. Hong, "An adaptive spatial fuzzy clustering algorithm for 3-D MR image segmentation," *Medical Imaging, IEEE Transactions on,* vol. 22, pp. 1063-1075, 2003.

[59] L. O. Hall, A. M. Bensaid, L. P. Clarke, R. P. Velthuizen, M. S. Silbiger, and J. C. Bezdek, "A comparison of neural network and fuzzy clustering techniques in segmenting magnetic resonance images of the brain," *Neural Networks, IEEE Transactions on,* vol. 3, pp. 672-682, 1992.

[60] M. N. Ahmed, S. M. Yamany, N. Mohamed, A. A. Farag, and T. Moriarty, "A modified fuzzy c-means algorithm for bias field estimation and segmentation of MRI data," *Medical Imaging, IEEE Transactions on,* vol. 21, pp. 193-199, 2002.

[61] A. Criminisi, D. Robertson, E. Konukoglu, J. Shotton, S. Pathak, S. White, and K. Siddiqui, "Regression forests for efficient anatomy detection and localization in computed tomography scans," *Medical Image Analysis,* vol. 17, pp. 1293-1303, 2013.

[62] A. Criminisi, J. Shotton, and S. Bucciarelli, "Decision forests with long-range spatial context for organ localization in CT volumes," in *MICCAI Workshop on Probabilistic Models for Medical Image Analysis*, 2009.

[63] L. Breiman, "Random Forests," *Machine Learning,* vol. 45, pp. 5-32, 2001/10/01 2001.

[64] R. C. Gonzalez and R. E. Woods, *Digital Image Processing*: Pearson/Prentice Hall, 2008.

[65] C. Yian-Leng and L. Xiaobo, "Adaptive image region-growing," *Image Processing, IEEE Transactions on,* vol. 3, pp. 868-872, 1994.

[66] R. Adams and L. Bischof, "Seeded region growing," *Pattern Analysis and Machine Intelligence, IEEE Transactions on,* vol. 16, pp. 641-647, 1994.

[67] T. Heinonen, P. Dastidar, H. Eskola, H. Frey, P. Ryymin, and E. Laasonen, "Applicability of semi-automatic segmentation for volumetric analysis of brain lesions," *Journal of Medical Engineering & Technology,* vol. 22, pp. 173-178, 1998.

[68] J. G. Tamez-Pena, S. Totterman, and K. J. Parker, "Unsupervised statistical segmentation of multispectral volumetric MRI images," 1999, pp. 300-311.

[69] R. Pohle and K. D. Toennies, "Segmentation of medical images using adaptive region growing," 2001, pp. 1337-1346.

[70] I. N. Manousakas, P. E. Undrill, G. G. Cameron, and T. W. Redpath, "Split-and-Merge Segmentation of Magnetic Resonance Medical Images: Performance Evaluation and Extension to Three Dimensions," *Computers and Biomedical Research,* vol. 31, pp. 393-412, 1998.

[71] M. Bomans, K. H. Hohne, U. Tiede, and M. Riemer, "3-D segmentation of MR images of the head for 3-D display," *Medical Imaging, IEEE Transactions on,* vol. 9, pp. 177-183, 1990.

[72] E. M. Haacke and L. Zhi-Pei, "Challenges of imaging structure and function with MRI," *Engineering in Medicine and Biology Magazine, IEEE,* vol. 19, pp. 55-62, 2000.

[73] M. Ashtari, J. L. Zito, B. I. Gold, J. A. Lieberman, M. T. Borenstein, and P. G. Herman, "Computerized volume measurement of brain structure," *Investigative Radiology*, vol. 25, pp. 798-805, 1990.

[74] S. Dellepiane, "Image Segmentation: Errors, sensitivity, and uncertainty," in *Engineering in Medicine and Biology Society, 1991. Vol.13: 1991., Proceedings of the Annual International Conference of the IEEE*, 1991, pp. 253-254.

[75] J. Sijbers, P. Scheunders, M. Verhoye, A. Van der Linden, D. van Dyck, and E. Raman, "Watershed-based segmentation of 3D MR data for volume quantization," *Magnetic Resonance Imaging*, vol. 15, pp. 679-688, 1997.

[76] M. Kass, A. Witkin, and D. Terzopoulos, "Snakes: Active contour models," *International Journal of Computer Vision*, vol. 1, pp. 321-331, 1988/01/01 1988.

[77] M.-O. Berger, "Snake growing," in *Computer Vision — ECCV 90*. vol. 427, O. Faugeras, Ed., ed: Springer Berlin Heidelberg, 1990, pp. 570-572.

[78] C. Xu and J. L. Prince, "Generalized gradient vector flow external forces for active contours," *Signal Processing*, vol. 71, pp. 131-139, 1998.

[79] S. Osher and J. A. Sethian, "Fronts propagating with curvature-dependent speed: Algorithms based on Hamilton-Jacobi formulations," *Journal of Computational Physics*, vol. 79, pp. 12-49, 1988.

[80] T. Liu, H. Zhou, F. Lin, Y. Pang, and J. Wu, "Improving image segmentation by gradient vector flow and mean shift," *Pattern Recognition Letters*, vol. 29, pp. 90-95, 2008.

[81] L. He, Z. Peng, B. Everding, X. Wang, C. Y. Han, K. L. Weiss, and W. G. Wee, "A comparative study of deformable contour methods on medical image segmentation," *Image and Vision Computing*, vol. 26, pp. 141-163, 2008.

[82] R. Malladi, J. A. Sethian, and B. C. Vemuri, "Shape modeling with front propagation: a level set approach," *Pattern Analysis and Machine Intelligence, IEEE Transactions on*, vol. 17, pp. 158-175, 1995.

[83] L. Vese and T. Chan, "A Multiphase Level Set Framework for Image Segmentation Using the Mumford and Shah Model," *International Journal of Computer Vision*, vol. 50, pp. 271-293, 2002/12/01 2002.

[84] H. Li, A. Yezzi, and L. Cohen, "Fast 3D Brain Segmentation Using Dual-Front Active Contours with Optional User-Interaction," in *Computer Vision for Biomedical Image Applications*. vol. 3765, Y. Liu, T. Jiang, and C. Zhang, Eds., ed: Springer Berlin Heidelberg, 2005, pp. 335-345.

[85] C. Li, R. Huang, Z. Ding, C. Gatenby, D. Metaxas, and J. Gore, "A Variational Level Set Approach to Segmentation and Bias Correction of Images with Intensity Inhomogeneity," in *Medical Image Computing and Computer-Assisted Intervention – MICCAI 2008*. vol. 5242, D. Metaxas, L. Axel, G. Fichtinger, and G. Székely, Eds., ed: Springer Berlin Heidelberg, 2008, pp. 1083-1091.

[86] L. Chunming, K. Chiu-Yen, J. C. Gore, and D. Zhaohua, "Minimization of Region-Scalable Fitting Energy for Image Segmentation," *Image Processing, IEEE Transactions on*, vol. 17, pp. 1940-1949, 2008.

[87] Y. Guisheng, L. Ying, and W. Yuhua, "3D level set model for medical image segmentation," in *BioMedical Information Engineering, 2009. FBIE 2009. International Conference on Future*, 2009, pp. 268-271.

[88] M. Lee, W. Cho, S. Kim, S. Park, and J. H. Kim, "Segmentation of interest region in medical volume images using geometric deformable model," *Computers in Biology and Medicine*, vol. 42, pp. 523-537, 2012.

[89] N. Barreira, M. G. Penedo, L. Cohen, and M. Ortega, "Topological active volumes: A topology-adaptive deformable model for volume segmentation," *Pattern Recognition*, vol. 43, pp. 255-266, 2010.

[90] J. Novo, N. Barreira, M. Penedo, and J. Santos, "Topological Active Volume 3D segmentation model optimized with genetic approaches," *Natural Computing*, vol. 11, pp. 161-174, 2012/03/01 2012.

[91] N. Barreira, M. G. Penedo, C. Mariño, and F. M. Ansia, "Topological Active Volumes," in *Computer Analysis of Images and Patterns*. vol. 2756, N. Petkov and M. Westenberg, Eds., ed: Springer Berlin Heidelberg, 2003, pp. 337-344.

[92] P. Lenkiewicz, M. Pereira, M. Freire, and J. Fernandes, "The whole mesh deformation model: a fast image segmentation method suitable for effective parallelization," *EURASIP Journal on Advances in Signal Processing*, vol. 2013, pp. 1-17, 2013/03/19 2013.

[93] P. Lenkiewicz, M. Pereira, M. Freire, and J. Fernandes, "The whole mesh Deformation Model for 2D and 3D image segmentation," in *Image Processing (ICIP), 2009 16th IEEE International Conference on*, 2009, pp. 4045-4048.

[94] O. Courchesne, F. Guibault, S. Parent, and F. Cheriet, "Patient-specific anisotropic model of human trunk based on MR data," *International Journal for Numerical Methods in Biomedical Engineering*, vol. 31, pp. n/a-n/a, 2015.

[95] R. Ardon and L. Cohen, "Fast Constrained Surface Extraction by Minimal Paths," *International Journal of Computer Vision*, vol. 69, pp. 127-136, 2006/08/01 2006.

[96] W. Neuenschwander, P. Fua, G. Szekely, and O. Kubler, "Initializing snakes [object delineation]," in *Computer Vision and Pattern Recognition, 1994. Proceedings CVPR '94., 1994 IEEE Computer Society Conference on*, 1994, pp. 658-663.

[97] X. Ge and J. Tian, "An automatic active contour model for multiple objects," in *Pattern Recognition, 2002. Proceedings. 16th International Conference on*, 2002, pp. 881-884 vol.2.

[98] C. Tauber, H. Batatia, and A. Ayache, "A general quasi-automatic initialization for snakes: application to ultrasound images," in *Image Processing, 2005. ICIP 2005. IEEE International Conference on*, 2005, pp. II-806-9.

[99] C. Tauber, H. Batatia, and A. Ayache, "A robust active contour initialization and gradient vector flow for ultrasound image segmentation," in *MVA*, 2005, pp. 164-167.

[100] C. Li, J. Liu, and M. D. Fox, "Segmentation of external force field for automatic initialization and splitting of snakes," *Pattern Recognition*, vol. 38, pp. 1947-1960, 2005.

[101] L. Bing and S. T. Acton, "Automatic Active Model Initialization via Poisson Inverse Gradient," *Image Processing, IEEE Transactions on*, vol. 17, pp. 1406-1420, 2008.

[102] D. W. Shattuck, M. Mirza, V. Adisetiyo, C. Hojatkashani, G. Salamon, K. L. Narr, R. A. Poldrack, R. M. Bilder, and A. W. Toga, "Construction of a 3D probabilistic atlas of human cortical structures," *NeuroImage,* vol. 39, pp. 1064-1080, 2008.

[103] B. M. Dawant, S. L. Hartmann, J. P. Thirion, F. Maes, D. Vandermeulen, and P. Demaerel, "Automatic 3-D segmentation of internal structures of the head in MR images using a combination of similarity and free-form transformations. I. Methodology and validation on normal subjects," *Medical Imaging, IEEE Transactions on,* vol. 18, pp. 909-916, 1999.

[104] P. L. Bazin and D. L. Pham, "Topology-Preserving Tissue Classification of Magnetic Resonance Brain Images," *Medical Imaging, IEEE Transactions on,* vol. 26, pp. 487-496, 2007.

[105] Z. Yongxin and B. Jing, "Atlas-Based Fuzzy Connectedness Segmentation and Intensity Nonuniformity Correction Applied to Brain MRI," *Biomedical Engineering, IEEE Transactions on,* vol. 54, pp. 122-129, 2007.

[106] M. Färber, J. Ehrhardt, and H. Handels, "Live-wire-based segmentation using similarities between corresponding image structures," *Computerized Medical Imaging and Graphics,* vol. 31, pp. 549-560, 2007.

[107] H. Park, P. H. Bland, and C. R. Meyer, "Construction of an abdominal probabilistic atlas and its application in segmentation," *IEEE Transactions on Medical Imaging,* vol. 22, pp. 483-492, 2003.

[108] Y. Zhou and J. Bai, "Multiple Abdominal Organ Segmentation: An Atlas-Based Fuzzy Connectedness Approach," *IEEE Transactions on Information Technology in Biomedicine,* vol. 11, pp. 348-352, 2007.

[109] T. Okada, K. Yokota, M. Hori, M. Nakamoto, H. Nakamura, and Y. Sato, "Construction of Hierarchical Multi-Organ Statistical Atlases and Their Application to Multi-Organ Segmentation from CT Images," Berlin, Heidelberg, 2008, pp. 502-509.

[110] R. Wolz, C. Chu, K. Misawa, K. Mori, and D. Rueckert, "Multi-organ Abdominal CT Segmentation Using Hierarchically Weighted Subject-Specific Atlases," Berlin, Heidelberg, 2012, pp. 10-17.

[111] T. Kohlberger, M. Sofka, J. Zhang, N. Birkbeck, J. Wetzl, J. Kaftan, J. Declerck, and S. K. Zhou, "Automatic Multi-organ Segmentation Using Learning-Based Segmentation and Level Set Optimization," Berlin, Heidelberg, 2011, pp. 338-345.

[112] C. Lu, Y. Zheng, N. Birkbeck, J. Zhang, T. Kohlberger, C. Tietjen, T. Boettger, J. S. Duncan, and S. K. Zhou, "Precise Segmentation of Multiple Organs in CT Volumes Using Learning-Based Approach and Information Theory," Berlin, Heidelberg, 2012, pp. 462-469.

[113] A. Tsai, W. Wells, C. Tempany, E. Grimson, and A. Willsky, "Mutual information in coupled multi-shape model for medical image segmentation," *Medical Image Analysis,* vol. 8, pp. 429-445, 2004.

[114] J. Yang, L. H. Staib, and J. S. Duncan, "Neighbor-Constrained Segmentation With Level Set Based 3-D Deformable Models," *IEEE Transactions on Medical Imaging*, vol. 23, pp. 940-948, 2004.

[115] P. Yan, W. Shen, A. A. Kassim, and M. Shah, "Segmentation of Neighboring Organs in Medical Image with Model Competition," Berlin, Heidelberg, 2005, pp. 270-277.

[116] K. Li, S. Millington, X. Wu, D. Chen, and M. Sonka, "Simultaneous Segmentation of Multiple Closed Surfaces Using Optimal Graph Searching," in *Information Processing in Medical Imaging*. vol. 3565, G. Christensen and M. Sonka, Eds., ed: Springer Berlin Heidelberg, 2005, pp. 406-417.

[117] X. Liu, D. Z. Chen, X. Wu, and M. Sonka, "Optimal graph search based image segmentation for objects with complex topologies," 2009, pp. 725915-725915-10.

[118] M. J. Costa, H. Delingette, S. Novellas, and N. Ayache, "Automatic Segmentation of Bladder and Prostate Using Coupled 3D Deformable Models," Berlin, Heidelberg, 2007, pp. 252-260.

[119] A. Shimizu, R. Ohno, T. Ikegami, H. Kobatake, S. Nawano, and D. Smutek, "Segmentation of multiple organs in non-contrast 3D abdominal CT images," *International journal of computer assisted radiology and surgery*, vol. 2, pp. 135-142, 2007.

[120] Y. Yin, R. Williams, D. D. Anderson, and M. Sonka, "Hierarchical Decision Framework with a Priori Shape Models for Knee Joint Cartilage Segmentation—MICCAI Grand Challenge," in *MICCAI 2010 Grand Challenges in Medical Image Analysis Workshop, Beijing, China*, 2010.

[121] Y. Gao, A. Tannenbaum, and R. Kikinis, "Simultaneous Multi-object Segmentation Using Local Robust Statistics and Contour Interaction," in *Medical Computer Vision. Recognition Techniques and Applications in Medical Imaging*. vol. 6533, ed: Springer Berlin Heidelberg, 2011, pp. 195-203.

[122] J.-M. Geusebroek, A. W. M. Smeulders, and H. Geerts, "A Minimum Cost Approach for Segmenting Networks of Lines," *International Journal of Computer Vision*, vol. 43, pp. 99-111, 2001.

[123] B. Li and S. T. Acton, "Active Contour External Force Using Vector Field Convolution for Image Segmentation," *Trans. Img. Proc.*, vol. 16, pp. 2096-2106, 2007.

[124] T. Preußer and M. Rumpf, "An Adaptive Finite Element Method for Large Scale Image Processing," *Journal of Visual Communication and Image Representation*, vol. 11, pp. 183-195, 2000/06/01/ 2000.

[125] C. Ebmeyer and J. Vogelgesang, "Finite element approximation of a forward and backward anisotropic diffusion model in image denoising and form generalization," *Numerical Methods for Partial Differential Equations*, vol. 24, pp. 646-662, 2008.

[126] S. Bougleux, G. Peyré, and L. D. Cohen, "Image compression with anisotropic triangulations," in *Computer Vision, 2009 IEEE 12th International Conference on*, 2009, pp. 2343-2348.

[127] K. H. Zou, S. K. Warfield, A. Bharatha, C. M. C. Tempany, M. R. Kaus, S. J. Haker, W. M. Wells, F. A. Jolesz, and R. Kikinis, "Statistical Validation of Image Segmentation Quality Based on a Spatial Overlap Index: Scientific Reports," *Academic Radiology*, vol. 11, pp. 178-189, 2004.

[128] L. Daw-Tung, L. Chung-Chih, and H. Siu-Wan, "Computer-aided kidney segmentation on abdominal CT images," *IEEE Transactions on Information Technology in Biomedicine*, vol. 10, pp. 59-65, 2006.

[129] K. Guo and D. Labate, "Characterization and Analysis of Edges Using the Continuous Shearlet Transform," *SIAM Journal on Imaging Sciences*, vol. 2, pp. 959-986, 2009.